Diffraction Analysis of Residual Stress;

Modelling Elastic Grain Interaction

Udo Welzel

Dissertation
an der
Universität Stuttgart

Diffraction Analysis of Residual Stress;
Modelling Elastic Grain Interaction

Von der Fakultät für Chemie der Universität Stuttgart
zur Erlangung der Würde eines Doktors der
Naturwissenschaften (Dr. rer. nat.) genehmigte Abhandlung

Vorgelegt von

Udo Siegfried Welzel

aus Selb in Bayern

Hauptberichter: Prof. Dr. Ir. E. J. Mittemeijer

Mitberichter: Prof. Dr. P. Scardi

Tag der Einreichung: 14. März 2002

Tag der mündlichen Prüfung: 3. Juni 2002

Max-Planck-Institut für Metallforschung Stuttgart,

Institut für Metallkunde der Universität Stuttgart,

Stuttgart, 2002

Abstract

X-ray (and neutron) diffraction can be used for the non-destructive analysis of residual and load stresses. Suitable parameters as (X-ray) elastic constants are required for relating the measured lattice strains to the components of the mechanical stress tensor.

For the first time a unifying, rigorous treatment for the diffraction stress analysis of both macroscopically elastically isotropic and anisotropic polycrystals has been given. The notion 'surface anisotropy' of bulk specimens has been revisited as a special case of direction-dependent grain interaction.

Evidence for direction-dependent grain interaction, i.e. the direction dependence of the elastic coupling of grains in a polycrystal, was obtained only very recently for the first time in the diffraction stress analysis of an untextured, polycrystalline nickel thin film by van Leeuwen *et al.* (1999). A stress analysis of the measured diffraction strains was only possible by adopting grain interaction assumptions given by Vook & Witt (1965). In this work, the Vook-Witt based grain interaction model is elaborated for the textured case.

The concept of direction-dependent grain interaction for diffraction analysis of stress is generalised, overcoming some unrealistic (extreme) grain interaction assumptions involved in the Vook-Witt based grain interaction model. Experimental verification has been achieved by X-ray diffraction strain measurements performed on a vapour deposited copper film.

To this end, a quantitative analysis of the texture of the specimen in terms of an orientation distribution function was required. This analysis was performed employing a Polycapillary X-ray lens. The corrections for instrumental aberrations in texture measurements with this optical component have been, for the first time, rigorously investigated and suitable correction procedures have been developed.

Table of Contents

5

1. Introduction

Thin surface layers, deposited by means of chemical or physical vapour deposition or formed, for example, by a process like plasma-nitriding are often utilised for improving the (surface) properties of bulks. For example: cutting tools may be covered with a thin ceramic surface layer of titanium nitride to enhance wear resistance. Moreover, layered structures are of key importance in the microelectronics industry.

Among the manifold of factors determining the properties of a layered structure, like adhesion of the layer(s), residual stress may be one of the least understood entities of a part entering its service live even though residual stress is of crucial importance for its performance and reliability (see, for example, Vande Walle, 1985, Machlin, 1995).

For obtaining fundamental insight into the origin of residual stress and its correlation to microstructure and properties, first of all methods of reliably measuring residual stress are required. Among a number of techniques, X-ray diffraction plays a key role being accurate, non-destructive and capable of providing additional information (see, for example, Noyan & Cohen, 1987, Hauk, 1997). Simultaneously with the X-ray diffraction stress measurement, as an example, the crystallographic texture can be analysed quantitatively.

This work is dedicated to residual stress analysis of polycrystalline specimens with a focus on modelling of elastic grain interaction in thin films and surfaces.
The analysis of residual stress by X-ray diffraction involves the measurement of elastic lattice strains as functions of two angles ψ and φ, where ψ is the inclination angle of the sample surface normal with respect to the diffraction vector and φ denotes the rotation of the sample around the sample surface normal. From a number of measured lattice strains for various measurement directions (i.e. various ψ and/or φ) for single or multiple reflections, the components of the mechanical stress tensor can be calculated by means of suitable, so-called diffraction elastic constants (see, for example, Noyan & Cohen, 1987, Hauk, 1997).

However, for polycrystalline specimens composed of (intrinsically) elastically anisotropic crystallites, the interpretation of the measured lattice strains in terms of mechanical stress is not straightforward. For (intrinsically) elastically anisotropic crystallites, the elastic properties depend on the crystallographic direction. As a consequence, stresses and strains vary over the crystallographically differently oriented crystallites in a polycrystalline specimen subjected to a mechanical stress-strain state. Therefore neither the mechanical elastic constants (relating mechanical (macroscopic) strains to mechanical (macroscopic) stresses) nor the diffraction elastic constants (diffraction stress factors for elastically

anisotropic samples), relating diffraction strains to mechanical stresses, can be derived without more ado from single-crystal data of the crystallites composing the specimen.

X-ray diffraction is highly susceptible to the elastic anisotropy, because lattice strains are measured for particular *hkl* reflections pertaining to particular crystallographic planes. Thus, lattice strains are not a direct measure for mechanical strains, being averages of the strains of all crystallites (see, for example, Möller & Martin, 1939, Hauk, 1997).

A possible solution of this problem is the adoption of a so-called grain-interaction model describing the distribution of stresses and strains over the crystallographically differently oriented crystallites in the specimen.

Common grain-interaction models, in particular the models of Voigt (1910), Reuss (1929), Neerfeld-Hill (Neerfeld, 1942, Hill, 1952) and Eshelby-Kröner (Eshelby, 1957, Kröner, 1958, see also Kneer, 1965), were devised for the calculation of mechanical elastic constants of polycrystals from single-crystal elastic data but these models can also be used for the calculation of diffraction elastic constants from single-crystal elastic data.

Even though the above models have been devised for bulk polycrystals, these models are also frequently applied to thin film stress analysis. Owing to their microstructure and reduced dimensionality, the elastic behaviour of thin films can be different from the elastic behaviour of corresponding bulk polycrystals. In a bulk specimen, each crystallite is surrounded by neighbouring crystallites in three dimensions, whereas this is not necessarily the case for a thin film (or surface adjacent material). See figure 1.1 for an example.

Thin films cannot generally be considered as macroscopically elastically isotropic; rather they can exhibit macroscopically transversely isotropic elastic properties (even in the absence of texture; van Leeuwen *et al.*, 1999). The traditional models for grain interaction (Voigt, Reuss, Eshelby-Kröner, Neerfeld-Hill) are compatible only with macroscopic elastic isotropy (in the absence of texture) and hence these models are inappropriate for the analysis of stress in such thin films.

Only recently van Leeuwen *et al.* (1999) observed experimentally the occurrence of transverse elastic isotropy for an untextured Ni film. Experimental observations (curved $\sin^2\psi$-plots; see further) being incompatible with the traditional models for grain interaction were interpreted on the basis of a grain interaction model adapted to the microstructure of a columnar thin film. To this end, grain-interaction assumptions proposed by Vook and Witt (Vook & Witt, 1965, Witt & Vook, 1968) were, for the first time, employed for the analysis of diffraction stress measurements. It was shown by van Leeuwen *et al.* (1999) that the Vook-Witt grain interaction assumptions give rise to elastic anisotropy on the macroscopic scale.
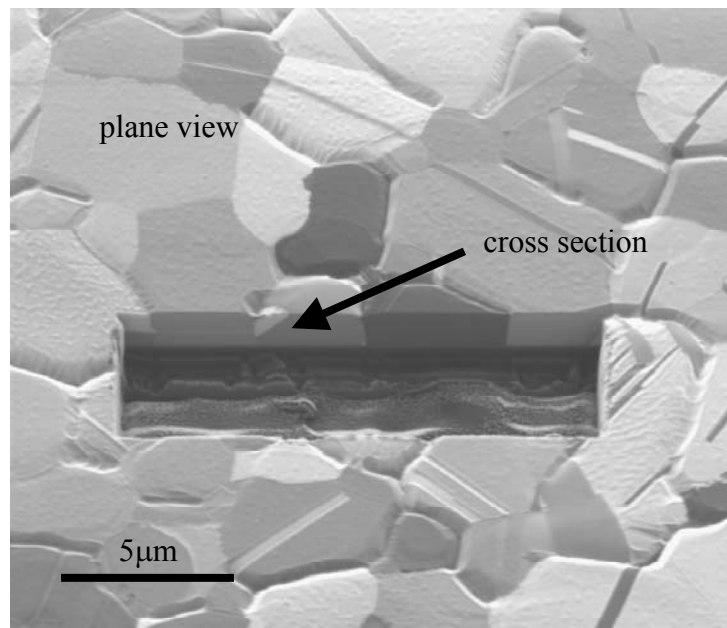
Figure 1.1: Micrograph of a sputtered (and annealed) copper layer (500nm thickness) taken with a focused ion beam workstation at a viewing angle of 45º. Prior to imaging, a rectangular section of the layer was removed by sputtering (employing the Ga-ion beam at high beam current). The cross section is visible simultaneously with the plane view.

In the Vook-Witt model it is assumed that the strain parallel to the specimen surface is equal in all crystallites and that the stress perpendicular to the specimen surface is zero in all crystallites. Thus, the grain interaction depends on the direction in the specimen and for that reason such a grain interaction model will be called a direction dependent grain interaction model.

The use of direction dependent grain interaction models for diffraction stress analysis (see also below) requires the implementation of these models in the theoretical framework. In *Chapter 2* of this work it is shown for the first time that the use of the so-called diffraction (X-ray) stress factors (Dölle & Hauk, 1978, Dölle & Hauk, 1979) is the most general formulation of the relation of the lattice strain to the components of the mechanical stress tensor, being valid for macroscopically elastically isotropic and anisotropic polycrystals (e.g. polycrystals with direction dependent grain interaction). However, for macroscopically elastically isotropic specimens, the use of the diffraction (X-ray) elastic constants is much simpler.

The concept of direction dependent grain interaction is introduced straightforwardly in the theoretical framework of diffraction stress analysis by the definition of the so-called grain

interaction tensor representing the linear transformation of the macroscopic mechanical stress tensor into the local stress tensor of a crystallite in a polycrystalline specimen.

In *Chapter 3* of this work, the Vook-Witt model is extended to textured specimens. On the basis of simulations of lattice strains for the case of fibre-texture it is demonstrated that erroneous results (errors as large as 50%) for the stress can occur when this type of grain interaction holds and, yet, traditional models are employed in stress analysis.

In *Chapter 4* of this work, a more general approach for the modelling of direction dependent grain interaction is proposed. Even though the Vook-Witt grain-interaction model has to be considered as some 'intermediate' model of grain interaction (with reference to the Voigt and Reuss models), it still imposes extreme constraints (e.g. identical in-plain strain for all crystallites). It is well known from literature (see, for example, Neerfeld, 1942, Hill, 1952, Hauk, 1997) that extreme grain-interaction assumptions are in general not compatible with the elastic behaviour of real specimens. Therefore, in this work a so-called effective grain interaction model, based on a linear combination of basic, extreme models with volume fractions as weighing factors is presented. To this end, the so-called inverse Vook-Witt model for grain interaction has been proposed. The proposed effective grain interaction model (combing the Reuss, Voigt, Vook-Witt and inverse Vook-Witt models) is applied to the diffraction analysis of stress in a fibre-textured copper layer. The measured lattice strains, represented as $\sin^2\psi$-plots (i.e. plots of the lattice strain versus the squared sin of the specimen tilt angle), are incompatible with the traditional grain interaction models. A consistent, simultaneous analysis of six $\sin^2\psi$-plots was possible only on the basis of the effective grain interaction model proposed in this work.

In *Chapter 5* the corrections for instrumental aberrations of pole figure measurements employing an X-ray lens (see, for example, Kumachov & Komarov, 1990, Kogan & Bethke, 1998, Scardi *et al.*, 2000) are discussed. Crystallographic texture is commonly met in thin films as a result of the layer growth. The occurrence of texture influences the mechanical and diffraction elastic constants considerably and thus it is necessary to consider texture in terms of an orientation distribution function in diffraction stress analysis.

In this work, an X-ray lens has been employed for diffraction stress and (simultaneous, see Chapter 4) texture analysis. The use of X-ray lenses, which have now been commercially available for a few years, is not yet frequent in texture analysis. The present work presents, on the basis of measurements performed with texture-free reference samples, an analysis of the corrections for instrumental aberrations of texture measurements (pole figures) if an X-ray

lens is employed. It is demonstrated that the use of an X-ray lens considerably simplifies the corrections necessary for the quantitative interpretation of the measured intensity in terms of orientation dependent volume fractions as compared to traditional (focusing, e.g. Bragg-Brentano) measurement geometries. Two correction procedures for the instrumental aberrations, an experimental one and a numerical one, have been described and tested.

The method was also successfully applied to the texture analysis of a fibre textured copper layer (see Chapter 4).

2. Diffraction Stress Analysis of Macroscopically Elastically Anisotropic Specimens; On the Concepts of Diffraction Elastic Constants and Stress Factors

Udo Welzel & Eric J. Mittemeijer

Abstract

For the first time a unifying, rigorous treatment has been given for the diffraction stress analysis of both macroscopically elastically isotropic specimens and macroscopically elastically anisotropic specimens. The applicability ranges of so-called diffraction elastic constants and diffraction stress factors have been discussed. It has been shown that the diffraction stress factors, originally introduced for the diffraction stress analysis of textured specimens, can also be used in the diffraction stress analysis of specimens exhibiting direction dependent grain interaction. The grain interaction tensor has been introduced and investigated for various grain interaction models. The notion surface anisotropy of bulk specimens has been revisited as a special case of direction dependent grain interaction.

2.1. Introduction

X-ray (and neutron) diffraction is a well-established tool for the non-destructive analysis of (macro-) stress states in polycrystalline solids. Usually, diffraction lines of one or more *hkl* reflections are measured at various specimen tilt (and, dependent on the complexity of the stress state, rotation) angles. From the angular positions of the diffraction lines, lattice spacings and thus (elastic) lattice strains can be calculated (see, for example, Noyan & Cohen, 1987, Hauk, 1997). The components of the mechanical stress tensor can be calculated from these lattice strains employing suitable parameters as elastic constants.

Experimental results indicated that the mechanical elastic constants relating the mechanical stress of the specimen to the mechanical elastic strain (e.g. *E*, Young's modulus, and *v*, Poisson's ratio, for macroscopically elastically isotropic specimens) are, in general, not suitable for the calculation of the components of the mechanical stress tensor from diffraction lattice strains (see, for example, Glocker, 1938, Möller & Martin, 1939). The strain probed by X-ray diffraction ('diffraction strain', named 'lattice strain' in the following) can be different from the mechanical strain because a diffraction line contains information on the elastic strain of only a subset of crystallites which have the lattice planes under study oriented perpendicular to the diffraction vector. Individual crystallites are, in general, intrinsically elastically anisotropic. Hence, the elastic properties of subsets of grains (as can be described by so-called diffraction elastic constants) can be different from the mechanical elastic properties of the whole specimen. Against this background the so-called diffraction (X-ray) elastic constants for macroscopically elastically isotropic (quasi-isotropic[1]) specimens (see, for example, Hauk, 1997; see also Chapter 2.3) and the so-called diffraction (X-ray) stress factors for textured (macroscopically elastically anisotropic) samples were introduced (Dölle & Hauk, 1978, Dölle & Hauk, 1979, Hauk, 1997; see also Chapter 2.2 and 2.3).

For the analysis of an homogeneous stress state in a macroscopically elastically *isotropic* specimen, the so-called $\sin^2\psi$-method can be used. This method relies on the linear (or elliptic, in the presence of shear stresses) dependence of the measured diffraction strain on $\sin^2\psi$, where ψ is the specimen tilt angle (i.e. the inclination of the lattice-strain measurement direction with respect to the surface normal of the specimen). The components of the mechanical stress tensor follow from slopes of straight lines (or parameters of ellipses, in the

---

[1] A specimen is termed quasi-isotropic if the (whole) specimen is elastically isotropic but the individual crystallites are elastically anisotropic.

case of the presence of shear stresses), fitted to the lattice-strain data in $\sin^2\psi$ -plots, and the values of the *hkl*-dependent X-ray elastic constants S_1^{hkl} and $\frac{1}{2}S_2^{hkl}$. These elastic constants were introduced on an empirical basis by Möller and Martin (1939) . The general proof of the validity of the concept of X-ray elastic constants for any macroscopically elastically isotropic polycrystal with a rigorous discussion of the underlying assumptions was not given before some tens of years later by Stickforth (1966).

For the analysis of an homogeneous stress state in macroscopically elastically *anisotropic* specimens, a diffraction analysis of stress is also possible. However, a rigorous derivation of the underlying equations lacks. Until recently, only (crystallographic) texture was considered as a possible source of macroscopic elastic anisotropy.

It was observed experimentally (for a comprehensive review, see for example Hauk, 1997) that non-linear $\sin^2\psi$-plots occur for textured materials. To account for these non-linearities, incompatible with the traditional $\sin^2\psi$ -behaviour, the so-called X-ray stress factors were introduced (on the basis of the Reuss grain interaction model; Dölle & Hauk, 1978, Dölle & Hauk, 1979).

X-ray diffraction stress analysis is also frequently applied for the determination of load or residual stress in thin films. Owing to their microstructure and reduced dimensionality, the elastic behaviour of thin films can be different from the elastic behaviour of bulk polycrystals. Thin films cannot generally be considered as macroscopically elastically isotropic, rather they can exhibit macroscopically transversely isotropic properties *even in the absence of texture*. Only recently, it has been demonstrated theoretically and experimentally by van Leeuwen *et al.* (1999) that the application of a new type of grain-interaction model, a so-called direction-dependent grain interaction model, is compatible with macroscopic anisotropic elastic behaviour even in the absence of texture. However, basic equations, analogous to the traditional $\sin^2\psi$-law for elastically isotropic specimens, lack.

In this work, the concept of diffraction elastic constants will be revisited rigorously. It will be demonstrated that the concept of X-ray stress factors holds for macroscopically elastically anisotropic specimens independent of the source of the anisotropy. Thus, X-ray stress factors can be employed for diffraction stress analysis of specimens exhibiting texture, direction dependent grain interaction, or both. Finally, the relation of the surface anisotropy as discussed by Stickforth (1966) with the recent direction dependent grain interaction models (van Leeuwen *et al.*, 1999, see also Chapter 3 and 4 of this work) is discussed.

17

2.2. Theoretical basis - frames of reference and calculation of mechanical and diffraction averages of elastic stress and strain tensors

It is convenient to introduce three Cartesian frames of reference:

- The *crystal frame of reference* (*C*): The conventional definition of an orthonormal crystal system, such as the one given by Nye (1957) (for a detailed treatment, see also Giacovazzo, 1998) is adopted. For cubic crystal symmetry the axes chosen coincide with the *a*, *b* and *c* axis of the crystal lattice.

- The *specimen frame of reference* (*S*): The S_3 axis is oriented perpendicular to the specimen surface and the S_1 and S_2 axes are in the surface plane.

- The *laboratory frame of reference* (*L*): This frame is chosen in such a way that the L_3-axis coincides with the diffraction vector in the (X-ray) diffraction experiment.

In the following a superscript (*C*, *S* or *L*) is used for indicating the reference frame adopted for the representation of a tensor. The absence of any superscript implies the validity of an equation independent of the reference frame used for tensor representation (but the same frame of reference has to be adopted for all tensors in the equation).

Transformations of tensors can be accomplished by suitable rotation matrices (for a general introduction on the use of transformation matrices in the context of diffraction stress analysis, see for example, Hauk, 1997; for details on matrices within the context of this Chapter, see also Chapter 3.).

The orientation of each crystallite in the *S* system can be identified by three Euler angles. The convention of Roe and Krigbaum (1964) in the definition of these angles will be adopted and these angles will be called α, β and γ. It is usual to associate a set of Euler angles with a vector $\vec{g} = (\alpha, \beta, \gamma)$ in the three-dimensional orientation (Euler) space *G* (for example, see Bunge, 1982a). In this way, each point in the orientation space *G* represents a possible orientation of the *C* frame of reference with respect to the *S* frame of reference. Only in the absence of texture it holds, that the volume fraction of crystallites having an orientation in the infinitesimal orientation range $d^3g = \sin(\beta)d\alpha d\beta d\gamma$ around $\vec{g}$ is independent of $\vec{g}$. Texture can be quantified by introducing the so-called orientation distribution function (ODF), $f(\alpha, \beta, \gamma)$, which is a function of the Euler angles, specifying the volume fraction of crystallites having an orientation in the infinitesimal orientation range $d^3g = \sin(\beta)d\alpha d\beta d\gamma$ around $\vec{g}$:

$$\frac{dV\left(\vec{g}\right)}{V} = \frac{f\left(\vec{g}\right)}{8\pi^2} dg = \frac{f(\alpha,\beta,\gamma)}{8\pi^2} \sin(\beta)d\alpha d\beta d\gamma .$$ (2.1)

The ODF is normalised:

$$\iiint_G \frac{f\left(\vec{g}\right)}{8\pi^2} d^3g = 1 .$$ (2.2)

On the basis of the Euler angles it is possible to calculate mechanical and diffraction averages of elastic-, stress- and strain tensors. In the following, angular brackets $\langle\,\rangle$ denote volume-weighted averages for all crystallites in the aggregate considered (i.e. mechanical averages) whereas braces $\{\,\}$ denote volume-weighted averages for diffracting crystallites only (i.e. diffraction averages). The group of diffracting crystallites is selected by specifying the *hkl* of the reflection considered and the orientation of the diffraction vector with respect to the specimen reference frame, which can be identified by the angles (φ,ψ), where φ denotes the rotation of the sample around the sample surface normal .

Mechanical averages of a tensor Ω can be calculated by integration over all Euler angles, using the ODF as a weighing factor:

$$\langle\Omega\rangle = \frac{1}{8\pi^2} \iiint_G \Omega \, f\left(\vec{g}\right) d^3g =$$

$$= \frac{1}{8\pi^2} \int_{\gamma=0}^{2\pi} \int_{\beta=0}^{\pi} \int_{\alpha=0}^{2\pi} \Omega(\alpha,\beta,\gamma) \, f(\alpha,\beta,\gamma) \, \sin(\beta)d\alpha d\beta d\gamma$$ (2.3)

A diffraction line contains data on only a subset of the crystallites for which the diffracting planes are perpendicular to the chosen measurement direction. Because only the measurement direction (i.e. the direction of the diffraction vector) is defined, a degree of freedom occurs for the diffracting crystallites: the rotation around the diffraction vector (denoted by the angle λ in the following). For a *hkl* diffraction line, the subset of diffracting crystallites is selected by the orientation of the diffraction vector with respect to the specimen frame of reference *S*. This is indicated by attaching sub- (φ,ψ) and superscripts (*hkl*) to the corresponding average:

$$\{\Omega\}_{\varphi,\psi}^{hkl} = \frac{\displaystyle\int_0^{2\pi} \Omega(hkl,\lambda,\varphi,\psi) \, f^*(hkl,\lambda,\varphi,\psi) \, d\lambda}{\displaystyle\int_0^{2\pi} f^*(hkl,\lambda,\varphi,\psi) \, d\lambda} .$$ (2.4)

$f^*(hkl,\lambda,\varphi,\psi)$ is the representation of the ODF in terms of the measurement parameters and the rotation angle λ. The ODF as defined in equation (2.1) cannot be directly used in equation (2.4), in analogy to equation (2.3), since the angles λ,φ,ψ are *not* Euler angles representing a

rotation of the C system with respect to the S system (they provide the rotation of the system L with respect to the system S). However, the values of α, β, γ and thus $f(\alpha,\beta,\gamma)$ at every λ can be calculated from hkl, λ, φ and ψ, to be finally substituted for $f^*(hkl,\lambda,\varphi,\psi)$ in equation (2.4) (for a more detailed treatment of the necessary transformations, see also Chapter 3 and the corresponding Appendix).

Using the above approach, the lattice strain $\varepsilon_{\varphi\psi}^{hkl}$ can be calculated as the average strain $\left\{\varepsilon_{33}^{L}\right\}_{\varphi\psi}^{hkl}$, i.e. the average strain parallel to the L_3-axis:

$$\varepsilon_{\varphi\psi}^{hkl} = \left\{\varepsilon_{33}^{L}\right\}_{\varphi\psi}^{hkl} = \frac{\displaystyle\int_{0}^{2\pi}\varepsilon_{33}^{L}(hkl,\lambda,\varphi,\psi)f^*(hkl,\lambda,\varphi,\psi)\ d\lambda}{\displaystyle\int_{0}^{2\pi}f^*(hkl,\lambda,\varphi,\psi)\ d\lambda}. \tag{2.5}$$

2.3. The fundamental equations of diffraction stress analysis

In this section first a short synopsis of the of the present stage of knowledge on the diffraction stress analysis of homogeneous stress states is given. The basic equations for macroscopically elastically isotropic, untextured and for macroscopically elastically anisotropic, textured polycrystalline specimens are presented. Then, recent developments in the field of grain-interaction models are discussed (Chapter 2.3.1). The shortcomings of the current understanding of the basics of diffraction stress analysis are: A rigorous discussion of the assumptions underlying (the role of grain interaction in) diffraction stress analysis lacks and the general applicability of the so-called X-ray stress factors has not been realised and demonstrated.

In this paper, the assumptions underlying diffraction stress analysis are introduced rigorously (Chapter 2.3.2), followed by a derivation of the $\sin^2\psi$-law for macroscopically elastically isotropic specimens (in association with the case of X-ray elastic constants; Chapter 2.3.3) and a derivation of the $\sin^2\psi$-law for macroscopically elastically anisotropic specimens (in association with the case of X-ray stress factors; Chapter 2.3.3). Special attention is paid to the sources of macroscopic elastic anisotropy as texture and direction dependent grain interaction. This section concludes with an illustration of the consequences of various grain interaction models as those due to Reuss, Voigt and Vook-Witt, for diffraction stress analysis.

2.3.1 Hierarchy of elastic anisotropy in diffraction stress analysis

2.3.1.1. Intrinsic elastic isotropy

For a polycrystalline material composed of elastically isotropic crystallites, Hooke's law relating the stress and the strain tensor in the specimen frame of reference reads:

$$\left\langle \varepsilon_{ij}^{S} \right\rangle = S_{ijkl}^{S} \left\langle \sigma_{kl}^{S} \right\rangle = \left(\delta_{ij}\delta_{kl}S_1 + \tfrac{1}{2}\left(\delta_{ik}\delta_{jl}+\delta_{il}\delta_{jk}\right)\tfrac{1}{2}S_2 \right)\left\langle \sigma_{kl}^{S} \right\rangle \qquad (2.6)$$

with

$$S_1 = -\frac{\nu}{E} \ \text{ and } \ \tfrac{1}{2}S_2 = \frac{1+\nu}{E}, \qquad (2.7),(2.8)$$

where ν is Poisson's ratio and E is Young's modulus. S^S is the compliance tensor of the body. Equation (2.6) contains mechanical quantities. However, in the case of elastically isotropic crystallites equation (2.6) holds as well for every crystallite in the aggregate (and thus also for the lattice strain probed by X-ray diffraction) as the elastic constants of the individual crystallites are independent of their orientation with respect to the specimen frame of reference. Thus the elastic properties of the body are identical to the elastic properties of the individual crystallites and S^S is the compliance tensor of the body as well as of the individual crystallites. Note that also the superscript indicating the reference frame could be skipped for S^S, as the compliance tensor has, in this case of intrinsic elastic isotropy for each crystallite, an identical notation with respect to every (orthogonal) reference frame.

The elastic lattice strain $\varepsilon_{\varphi\psi}$ measured by X-ray diffraction can be obtained as the strain along the direction of the diffraction vector $\overrightarrow{m^S}$. No averaging is necessary here as the strain tensor is *identical* for all elastically isotropic crystallites; angular/curly brackets and the indication of the particular reflection considered can be skipped in this case, i.e. $\left\langle \sigma_{ij}^{S} \right\rangle \equiv \sigma_{ij}^{S}$ and $\left\{ \varepsilon_{33}^{L} \right\}_{\varphi\psi}^{\mathbf{h}} \equiv \varepsilon_{\varphi\psi}$, and thus:

$$\begin{aligned}
\varepsilon_{\varphi\psi} = m_i^S \varepsilon_{ij}^S m_j^S = {} & \varepsilon_{11}^S \cos^2\varphi \sin^2\psi + \varepsilon_{22}^S \sin^2\varphi \sin^2\psi + \varepsilon_{33}^S \cos^2\psi + \\
& + \varepsilon_{12}^S \sin 2\varphi \sin^2\psi + \varepsilon_{13}^S \cos\varphi \sin 2\psi + \varepsilon_{23}^S \sin\varphi \sin 2\psi
\end{aligned} \qquad (2.9)$$

where

$$\overrightarrow{m^S} = \begin{pmatrix} \sin\psi\cos\varphi \\ \sin\psi\sin\varphi \\ \cos\psi \end{pmatrix}. \qquad (2.10)$$

The angles φ and ψ define the orientation of the (normalised) diffraction vector $\vec{m}$ (i.e. the direction of the strain measurement, the z-direction of the laboratory frame of reference) with respect to the sample reference frame (see Chapter 2.2.).

By insertion of equation (2.6) into equation (2.9), it follows straightforwardly:

$$\varepsilon_{\varphi\psi} = \tfrac{1}{2}S_2 \sin^2\psi\left(\sigma_{11}^S\cos^2\varphi + \sigma_{12}^S\sin(2\varphi) + \sigma_{22}^S\sin^2\varphi\right) +$$
$$+ \tfrac{1}{2}S_2\left(\sigma_{13}^S\cos\varphi\sin(2\psi) + \sigma_{23}^S\sin\varphi\sin(2\psi) + \sigma_{33}^S\cos^2\psi\right) \qquad (2.11)$$
$$+ S_1\left(\sigma_{11}^S + \sigma_{22}^S + \sigma_{33}^S\right)$$

S_1 and $\tfrac{1}{2}S_2$ are the elastic constants relating the measured lattice strain (i.e. $\varepsilon_{33}^L = \varepsilon_{\varphi\psi}$) to the components of the mechanical stress tensor σ_{ij}^S. Note that, formally, the elastic constants S_1 and $\dfrac{1}{2}S_2$ used in equations (2.6) and (2.11) are defined in the specimen frame of reference (however, they would, due to the isotropy of the polycrystal, be the same in any other orthogonal reference frame). Note that, for a polycrystalline aggregate consisting of elastically isotropic crystallites, equation (2.11) holds independently of the presence of crystallographic texture or the occurrence of direction dependent grain interaction.

2.3.1.2. Macroscopic elastic isotropic ('quasi-isotropy')

For a polycrystalline aggregate composed of elastically anisotropic crystallites, mechanical elastic isotropy requires *at least* the absence of texture (and the absence of direction dependence of the grain interaction; see corresponding discussion in Chapter 2.3.3). When a polycrystal composed of elastically anisotropic crystallites exhibits macroscopic elastic isotropy, which is also called 'quasi-isotropy', a diffraction analysis of a homogeneous stress state is still possible on the basis of equation (2.11). To this end, the elastic constants S_1 and $\tfrac{1}{2}S_2$ have to be replaced by the so-called *hkl*-dependent X-ray elastic constants S_1^{hkl} and $\tfrac{1}{2}S_2^{hkl}$. Then, the lattice strains depend on the reflection *hkl* (in this case, the stresses / strains of individual crystallites are not equal to the corresponding mechanical averages, thus averaging braces and brackets, cf. Chapter 2.2, have to be used):

$$\left\{\varepsilon_{33}^L\right\}_{\varphi\psi}^{hkl} = \tfrac{1}{2}S_2^{hkl}\sin^2\psi\left(\left\langle\sigma_{11}^S\right\rangle\cos^2\varphi + \left\langle\sigma_{12}^S\right\rangle\sin(2\varphi) + \left\langle\sigma_{22}^S\right\rangle\sin^2\varphi\right) +$$
$$+ \tfrac{1}{2}S_2^{hkl}\left(\left\langle\sigma_{13}^S\right\rangle\cos\varphi\sin(2\psi) + \left\langle\sigma_{23}^S\right\rangle\sin\varphi\sin(2\psi) + \left\langle\sigma_{33}^S\right\rangle\cos^2\psi\right) \quad (2.12)$$
$$+ S_1^{hkl}\left(\left\langle\sigma_{11}^S\right\rangle + \left\langle\sigma_{22}^S\right\rangle + \left\langle\sigma_{33}^S\right\rangle\right)$$

The X-ray elastic constants S_1^{hkl} and $\frac{1}{2}S_2^{hkl}$ can be measured by applying a known load stress to a specimen under simultaneous lattice strain measurement in a diffractometer or they can be calculated from single crystal elastic compliances by adopting a grain-interaction model. The modifications of equation (2.11) necessary to obtain equation (2.12) were introduced on an empirical basis: about ten years after the first strain measurements by means of X-ray diffraction (Joffe & Kirpitcheva, 1922), Möller & Barbers (1935) obtained experimental results indicating that equation (2.11) cannot be used for the stress analysis of polycrystals composed of elastically anisotropic crystallites, i.e. lattice strains differ from mechanical strains (as an effect of single crystal elastic anisotropy). The following introduction of the X-ray elastic constants on an empirical basis by Möller and Martin (1939) was supported by an elaboration of the Voigt grain-interaction model (Voigt, 1910, and Reuss, 1929) and an elaboration of the Reuss grain-interaction model (Möller and Martin, 1939) for the application to the stress analysis by diffraction for a principal stress state.

However, a rigorous proof of the validity of equation (2.12) for any quasi-isotropic polycrystal for any state of stress (irrespective of the type of grain interaction) was given decades later by Stickforth (1966). Evenschor and Hauk (1975) were the first to discuss explicitly the analysis of the shear components of the stress tensor.

The analogous structures of equation (2.12) and (2.11) suggest that also the X-ray elastic constants S_1^{hkl} and $\frac{1}{2}S_2^{hkl}$ are defined in the sample reference frame. However, this is *not* the case; the X-ray elastic constants are defined in laboratory reference frame (for further discussion on the validity of equation (2.12), see Chapter 2.3.3).

2.3.1.3. Macroscopic elastic anisotropy; case of a textured polycrystal

For a polycrystalline aggregate consisting of elastically anisotropic crystallites, the occurrence of texture leads to a macroscopically elastically anisotropic behaviour. Thus, the use of equation (2.12) for stress analysis is not possible, as equation (2.12) is incompatible with macroscopic elastic anisotropy. Experimentally it was found (for an comprehensive review, see for example Hauk, 1997) that non-linear $\sin^2\psi$-plots are generally observed for textured specimens (also for a plane state of stress). The equation proposed for diffraction stress analysis in this case resulted from adopting a particular model of grain interaction, the Reuss model, and in this context the stress factors $F_{kl}(\psi,\varphi,hkl)$ were introduced (Dölle & Hauk, 1978, Dölle & Hauk, 1979):

$$\left\{\varepsilon_{33}^L\right\}_{\varphi\psi}^{\mathbf{h}} = F_{kl}(\psi,\varphi,hkl)\left\langle\sigma_{kl}^S\right\rangle \tag{2.13}$$

24

The stress factors $F_{kl}(\psi, \varphi, hkl)$ can be measured by applying a known load stress to a specimen under simultaneous lattice strain measurement in a diffractometer or calculated from single crystal elastic compliances (by adopting a grain interaction model).

A general proof of the validity of equation (2.13) for macroscopically elastically anisotropic specimens exhibiting texture, independently of the adoption of a particular grain-interaction model lacks. This proof is provided in Chapter 2.3.2.

2.3.1.4. Macroscopic elastic anisotropy; case of direction dependent grain interaction

Recently, the occurrence of non-linear $\sin^2\psi$-plots for an untextured nickel film in a plane state of stress was reported by van Leeuwen *et al.* (1999). Similar observations were reported earlier in a diffraction stress analysis of a TiN specimen by Rafaja *et al.* (1996). These results can not be analysed on the basis of the traditional $\sin^2\psi$-law, equation (2.12), as then only a linear dependence of the lattice strain on $\sin^2\psi$ is possible (for a plane state of stress). A consistent stress analysis was possible by developing a so-called direction dependent grain-interaction model (van Leeuwen *et al.*, 1999, see Chapter 3). In a direction dependent grain-interaction model, the elastic coupling of crystallites is direction dependent (for a precise definition of direction dependent grain interaction, see also Chapter 2.3.3). The simultaneous occurrence of texture and direction dependent grain interaction has been dealt with in Chapter 3.

The occurrence of direction dependent grain interaction implies that, even in the absence of texture, a polycrystal exhibits macroscopic elastic isotropy, as was pointed out by van Leeuwen *et al.* (1999), hereby excluding applicability of equation (2.12).

The equations analogous to the traditional $\sin^2\psi$-law, underlying a diffraction stress analysis of a polycrystal with direction dependent grain interaction, lack (only numerical calculations of the lattice strains for a given mechanical stress/strain state of the polycrystal have been presented). In this paper it will be shown that, under certain basic assumptions, equation (2.13) is generally valid for any macroscopically elastically anisotropic polycrystal, independent of the origin of the anisotropy which can be texture, direction dependent grain interaction or both.

2.3.2. The assumptions underlying diffraction stress analysis

The basic assumption for diffraction stress analysis is the validity of the following equation:

$$\left\{\varepsilon_{ij}^{L}\right\}_{\varphi\psi}^{hkl} = A_{ijkl}^{L}\left(hkl,\varphi,\psi,s^{C},\Upsilon,f^{*}\right)\left\langle\sigma_{kl}^{L}\right\rangle. \tag{2.14}$$

$A^{L}\left(hkl,\varphi,\psi,s^{C},\Upsilon,f^{*}\right)$ is a suitable rank-four tensor (Stickforth, 1966), which generally depends on hkl, φ, ψ, s^{C} (the single-crystal elastic compliance tensor), Υ (the so-called grain interaction tensor, see below) and f^{*} (the crystallographic orientation distribution function).

For diffraction stress analysis, only $\left\{\varepsilon_{33}^{L}\right\}_{\varphi\psi}^{hkl}$ is relevant (i.e. the strain in the direction of the diffraction vector) and the mechanical stress in the laboratory frame of reference $\left\langle\sigma_{ij}^{L}\right\rangle$ can be expressed in terms of the mechanical stress $\left\langle\sigma_{mn}^{S}\right\rangle$ in the specimen frame of reference by an orthogonal transformation relating specimen and laboratory frames of reference, represented by the matrix Ω (for the definition of Ω, see Appendix 2.1):

$$\left\langle\sigma_{ij}^{L}\right\rangle = \Omega_{im}\Omega_{jn}\left\langle\sigma_{mn}^{S}\right\rangle \tag{2.15}$$

Using equation (2.15), equation (2.14) can be rearranged

$$\left\{\varepsilon_{33}^{L}\right\}_{\varphi\psi}^{hkl} = A_{33ij}^{L}\left(hkl,\varphi,\psi,s^{C},\Upsilon,f^{*}\right)\left\langle\sigma_{ij}^{L}\right\rangle =$$
$$A_{33ij}^{L}\left(hkl,\varphi,\psi,s^{C},\Upsilon,f^{*}\right)\Omega_{im}\Omega_{jn}\left\langle\sigma_{mn}^{S}\right\rangle = F_{mn}\left(hkl,\varphi,\psi,s^{C},\Upsilon,f^{*}\right)\left\langle\sigma_{mn}^{S}\right\rangle \tag{2.16}$$

with:

$$F_{mn}\left(hkl,\varphi,\psi,s^{C},\Upsilon,f^{*}\right) = A_{33ij}^{L}\left(hkl,\varphi,\psi,s^{C},\Upsilon,f^{*}\right)\Omega_{im}\Omega_{jn}. \tag{2.17}$$

$F_{mn}\left(hkl,\varphi,\psi,s^{C},\Upsilon,f^{*}\right)$ are the so-called X-ray stress factors, which have been introduced in Chapter 2.3.1.3 (in the context of texture, cf. equation (2.13)). Note that the X-ray stress factors are due to their definition, equation (2.17), *not* the components of a rank-two tensor.

Equations (2.14) and (2.15) imply that the concept of effective elastic constants, i.e. the A_{ijkl}^{L}, are valid for ensembles of grains selected in diffraction measurements. The general validity of equations (2.14) and (2.15) is not trivial. A general proof has not been presented so far (a similar problem, the validity of the concept of effective elastic constants for relating the mechanical strain tensor to the mechanical stress tensor, was investigated on the basis of statistical continuum mechanics by Kröner (1971)). Throughout this paper, the validity of equation (2.14) will be presupposed.

Note that, as the stress and the strain tensors are symmetric, it holds that:

$$A_{ijkl} = A_{jikl} = A_{ijlk} \,. \tag{2.18}$$

The condition under which equation (2.14) is valid can be reformulated as follows.

Consider Hooke's law for an individual crystallite in a polycrystalline sample:

$$\varepsilon_{ij}^L = s_{ijkl}^L \sigma_{kl}^L \tag{2.19}$$

where ε^L is the elastic strain tensor of the crystallite, σ^L is the corresponding stress tensor and s^L is the single crystal compliance tensor transformed to the laboratory frame of reference. The stress tensor for every crystallite is a function of the mechanical stress tensor of the polycrystal and the orientation of the crystallite represented by $hkl, \lambda, \varphi, \psi$:

$$\sigma_{kl}^L = \sigma_{kl}^L \left(\left\langle \sigma^L \right\rangle, hkl, \lambda, \varphi, \psi \right) \tag{2.20}$$

Inserting equation (2.20) in equation (2.19) and calculating the average for the diffracting crystallites yields (cf. equation (2.4)):

$$\left\{ \varepsilon_{ij}^L \right\}_{\varphi\psi}^{hkl} = \frac{\int_0^{2\pi} s_{ijkl}^L \left(hkl, \lambda \right) \sigma_{kl}^L \left(\left\langle \sigma^L \right\rangle, hkl, \lambda, \varphi, \psi \right) f^* \left(hkl, \lambda, \varphi, \psi \right) d\lambda}{\int_0^{2\pi} f^* \left(hkl, \lambda, \varphi, \psi \right) d\lambda} \tag{2.21}$$

Now, the right-hand side of equation (2.21) equals the right-hand side of equation (2.14) if:

$$\sigma_{kl}^L = \Upsilon_{klmn}^L \left(hkl, \lambda, \varphi, \psi \right) \left\langle \sigma_{mn}^L \right\rangle \tag{2.22}$$

with

$$A_{ijkl}^L \left(hkl, \varphi, \psi, s^C, \Upsilon, f^* \right) =$$
$$\frac{\int_0^{2\pi} s_{ijmn}^L \left(hkl, \lambda \right) \Upsilon_{mnkl}^L \left(hkl, \lambda, \varphi, \psi \right) f^* \left(hkl, \lambda, \varphi, \psi \right) d\lambda}{\int_0^{2\pi} f^* \left(hkl, \lambda, \varphi, \psi \right) d\lambda} \,. \tag{2.23}$$

The (arbitrarily) introduced function Υ is obviously a fourth-rank tensor and represents the outcome of the elastic interaction of the grains in the specimen, i.e. it tells how from the macroscopic stress the stress of a single crystallite can be calculated. Hence, Υ will be called the grain-interaction tensor.

2.3.3. Macroscopic elastic isotropy and anisotropy: diffraction (X-ray) elastic constants and diffraction (X-ray) stress factors

In the following, the consequences of macroscopic elastic isotropy of the polycrystal on the tensor $A^L\left(hkl,\varphi,\psi,s^C,\Upsilon,f^*\right)$ defined in equation (2.23) will be investigated. *By definition* a polycrystal is (said to be) macroscopically elastically isotropic if the average stress/strain state in the laboratory frame of reference of *any* ensemble of diffracting crystallites (i.e. $\left\{\varepsilon_{ij}^L\right\}_{\varphi\psi}^{hkl}$ and $\left\{\sigma_{ij}^L\right\}_{\varphi\psi}^{hkl}$) is independent of the orientation of the polycrystal with respect to the laboratory frame of reference when the polycrystal is subjected to a certain macroscopic, mechanical stress/strain state in the laboratory frame of reference (see Burbach, 1974). Under this assumption, the $A_{ijkl}^L\left(hkl,\varphi,\psi,s^C,\Upsilon,f^*\right)$ are independent of φ and ψ:

$$\frac{\partial}{\partial\varphi}A_{ijkl}^L\left(hkl,\varphi,\psi,s^C,\Upsilon,f^*\right)=0 \tag{2.24}$$

$$\frac{\partial}{\partial\psi}A_{ijkl}^L\left(hkl,\varphi,\psi,s^C,\Upsilon,f^*\right)=0, \tag{2.25}$$

i.e. the 'orientation-dependence' of the $A_{ijkl}^L\left(hkl,\varphi,\psi,s^C,\Upsilon,f^*\right)$ is only due to the reflection *hkl*. Further simplification of the $A_{ijkl}^L\left(hkl,s^C,\Upsilon,f^*\right)$ is possible considering that every ensemble of diffracting crystallites is invariant with respect to a rotation around the diffraction vector. Thus, only the following components can be non-zero (see, for example, Hauk, 1997):

$$\begin{aligned}
&A_{1111}^L=A_{2222}^L,\quad A_{3333}^L,\quad A_{1122}^L,\quad A_{2211}^L,\quad A_{1133}^L=A_{2233}^L,\quad A_{3311}^L=A_{3322}^L,\\
&A_{1313}^L=A_{2323}^L,\quad A_{3131}^L=A_{3232}^L,\quad A_{1212}^L,\quad A_{2121}^L
\end{aligned} \tag{2.26}$$

By using equations (2.26) in simplifying equation (2.14), the diffraction strain $\left\{\varepsilon_{33}^L\right\}_{\varphi\psi}^{hkl}$ reads:

$$\begin{aligned}
\left\{\varepsilon_{33}^L\right\}_{\varphi\psi}^{hkl}&=A_{33kl}^L\left(hkl,s^C,\Upsilon,f^*\right)\cdot\left\langle\sigma_{kl}^L\right\rangle=\\
&=A_{3311}^L\left(hkl,s^C,\Upsilon,f^*\right)\cdot\left(\left\langle\sigma_{11}^L\right\rangle+\left\langle\sigma_{22}^L\right\rangle\right)+A_{3333}^L\left(hkl,s^C,\Upsilon,f^*\right)\cdot\left\langle\sigma_{33}^L\right\rangle
\end{aligned} \tag{2.27}$$

By defining

$$\begin{aligned}
S_1^{hkl}&\equiv A_{3311}^L\left(hkl,s^C,\Upsilon,f^*\right),\\
\frac{1}{2}S_2^{hkl}&\equiv A_{3333}^L\left(hkl,s^C,\Upsilon,f^*\right)-A_{3311}^L\left(hkl,s^C,\Upsilon,f^*\right)
\end{aligned} \tag{2.28}$$

and replacing the mechanical stress tensor components in the laboratory reference frame $\left\langle\sigma_{ij}^L\right\rangle$ by the mechanical stress tensor components in the specimen frame of reference $\left\langle\sigma_{ij}^S\right\rangle$

(for the necessary transformation matrices, see Appendix 2.1) equation (2.27) is directly transformed into equation (2.12): the traditional $\sin^2\psi$-law. Thus, the assumption of macroscopic elastic isotropy together with the adoption of equation (2.14) is sufficient for the derivation of the traditional $\sin^2\psi$-law. Note that the X-ray elastic constants S_1^{hkl} and $\frac{1}{2}S_2^{hkl}$ derived in the above way are defined in the laboratory frame of reference L (cf. equation (2.28)).

The assumption of macroscopic elastic isotropy imposes certain restrictions for the $A^L\left(hkl,\varphi,\psi,s^C,\Upsilon,f^*\right)$, which are expressed by equations (2.24), (2.25) and (2.26). The consequences of macroscopic elastic isotropy for the grain interaction tensor and the orientation distribution function will be discussed next.

If macroscopic elastic isotropy occurs, it follows from equations (2.24) and (2.25) that

$$\frac{\partial}{\partial\varphi}\frac{\int_0^{2\pi} s_{ijkl}^L\left(hkl,\lambda\right)\Upsilon_{klmn}^L\left(hkl,\lambda,\varphi,\psi\right)f^*\left(hkl,\lambda,\varphi,\psi\right)d\lambda}{\int_0^{2\pi} f^*\left(hkl,\lambda,\varphi,\psi\right)d\lambda}=0 \tag{2.29}$$

$$\frac{\partial}{\partial\psi}\frac{\int_0^{2\pi} s_{ijkl}^L\left(hkl,\lambda\right)\Upsilon_{klmn}^L\left(hkl,\lambda,\varphi,\psi\right)f^*\left(hkl,\lambda,\varphi,\psi\right)d\lambda}{\int_0^{2\pi} f^*\left(hkl,\lambda,\varphi,\psi\right)d\lambda}=0\,. \tag{2.30}$$

By reversing the order of the partial differentiation and the integration, it follows:

$$\frac{\partial}{\partial\varphi}\Upsilon_{klmn}^L\left(hkl,\lambda,\varphi,\psi\right)f^*\left(hkl,\lambda,\varphi,\psi\right)=$$
$$=\frac{\partial}{\partial\psi}\Upsilon_{klmn}^L\left(hkl,\lambda,\varphi,\psi\right)f^*\left(hkl,\lambda,\varphi,\psi\right)=0 \tag{2.31}$$

As the grain interaction tensor is defined independent of the orientation distribution function (cf. equation (2.22)), we can conclude that:

$$\frac{\partial}{\partial\varphi}\Upsilon_{klmn}^L\left(hkl,\lambda,\varphi,\psi\right)=\frac{\partial}{\partial\psi}\Upsilon_{klmn}^L\left(hkl,\lambda,\varphi,\psi\right)=0 \tag{2.32}$$

$$\frac{\partial}{\partial\varphi}f^*\left(hkl,\lambda,\varphi,\psi\right)=\frac{\partial}{\partial\psi}f^*\left(hkl,\lambda,\varphi,\psi\right)=0\,. \tag{2.33}$$

Equations (2.33) imply that the specimen is untextured as from equation (2.33) it follows that

$$\frac{\partial}{\partial\varphi}\int_0^{2\pi} f^*\left(hkl,\lambda,\varphi,\psi\right)d\lambda=\frac{\partial}{\partial\psi}\int_0^{2\pi} f^*\left(hkl,\lambda,\varphi,\psi\right)d\lambda=0 \tag{2.34}$$

which is equivalent to the statement that the corresponding pole figure for the reflection *hkl* is φ- and ψ-independent.

Equation (2.32) expresses the requirement of macroscopic isotropy for the grain interaction tensor (cf. equation (2.22)). Also, equations (2.26) impose restrictions on the actual grain interaction. If *L'* is a Cartesian frame of reference which is rotated by an angle δ around the L_3 axis with respect to the laboratory frame of reference, equations (2.26) require that (texture is not considered as the occurrence of texture is not compatible with macroscopic elastic isotropy):

$$A_{ijkl}^{L'}\left(hkl,s^{C},\Upsilon\right)=A_{ijkl}^{L}\left(hkl,s^{C},\Upsilon\right) \tag{2.35}$$

In Appendix 2.2 it is demonstrated that for macroscopic elastic isotropy, equation (2.35) is equivalent to:

$$\Delta_{im}^{\delta}\Delta_{jn}^{\delta}\Delta_{ko}^{\delta}\Delta_{lp}^{\delta}\Upsilon_{mnop}^{L}\left(hkl,\lambda+\delta\right)=\Upsilon_{ijkl}^{L}\left(hkl,\lambda\right) \tag{2.36}$$

where Δ^{δ} is a matrix representing the othonormal transformation from the *L* frame of reference to the *L'* frame of reference. Hence, if at least one of equations (2.32) and (2.36) does not hold, the grain interaction is no longer direction independent but direction dependent. Then, the polycrystal is macroscopically elastically anisotropic.

Note that equations (2.32), (2.33) and (2.36) together are equivalent to the definition of macroscopic elastic isotropy as given at the beginning of this subsection.

It should be noted that although the grain interaction can be isotropic (i.e. equations (2.32) and (2.36) hold), the specimen can exhibit macroscopic elastic anisotropic behaviour yet, if preferred orientation (texture) occurs (i.e. equation (2.33) does not hold). Such cases are discussed in Chapter 2.3.4.1 and 2.3.4.2.

Thus, in case of macroscopic elastic isotropy, diffraction stress analysis can be performed by using equation (2.12) by employing the concept of diffraction (X-ray) elastic constants. In all cases of macroscopic elastic anisotropy, i.e. due to direction dependent grain interaction and/or the occurrence of preferred orientation, in association with intrinsic single crystal elastic anisotropy, diffraction stress analysis can be performed using equation (2.16) employing the concept of diffraction (X-ray) stress factors.

Until now, the (implicit) assumption inherent to all diffraction stress analyses, as expressed by equation (2.14) has not been generally recognised. Furthermore, the general validity of the stress factors, applicable in all cases of macroscopic anisotropy, has not been shown before.

2.3.4. Examples

In the following, the theoretical considerations of Chapters 2.3.1 to 2.3.3 will be illustrated on the basis of the Reuss, the Voigt and the Vook-Witt based grain interaction model.

2.3.4.1. Reuss grain interaction model

Adopting the Reuss model, the components of the stress tensor in the specimen frame of reference for every individual crystallite are set equal to the corresponding components of the mechanical stress tensor:

$$\sigma_{ij}^{S} = \left\langle \sigma_{ij}^{S} \right\rangle . \tag{2.37}$$

By introducing the rank-four identity I, equation (2.37) can be rewritten:

$$\sigma_{kl}^{S} = I_{klmn} \left\langle \sigma_{mn}^{S} \right\rangle , \tag{2.38}$$

The rank-four identity is defined as (δ is Kronecker-Delta):

$$I_{ijkl} = \frac{1}{2} \left(\delta_{ik} \delta_{jl} + \delta_{il} \delta_{jk} \right) \tag{2.39}$$

Obviously, equations (2.37) and (2.38) also hold in the laboratory frame of reference. Then, by comparison of equation (2.38), with the superscript '*S*' substituted by the superscript '*L*', with equation (2.22), it can be concluded that

$$\Upsilon_{klmn}^{L} \left(hkl, \lambda, \varphi, \psi \right) = \Upsilon_{klmn}^{L} = I_{klmn} . \tag{2.40}$$

Thus, the grain interaction tensor adopting the Reuss grain interaction model is the rank-4 identity. Υ_{klmn}^{L} fulfils equations (2.32) and (2.36), thus the Reuss model is an isotropic grain interaction model. Note that a textured specimen obeying the Reuss grain interaction model is macroscopically elastically anisotropic, as in this case, equation (2.33) does not hold (see discussion in Chapter 2.3.3).

2.3.4.2. Voigt grain interaction model

Adopting the Voigt model, the components of the strain tensor in the specimen frame of reference for every individual crystallite are set equal to the corresponding components of the mechanical strain tensor:

$$\varepsilon_{ij}^{S} = \left\langle \varepsilon_{ij}^{S} \right\rangle . \tag{2.41}$$

The mechanical stress can be calculated from:

$$\left\langle \sigma_{ij}^S \right\rangle = \left\langle c_{ijkl}^S \varepsilon_{kl}^S \right\rangle = \left\langle c_{ijkl}^S \right\rangle \left\langle \varepsilon_{kl}^S \right\rangle, \tag{2.42}$$

thus

$$\varepsilon_{ij}^S = \left\langle \varepsilon_{ij}^S \right\rangle = \left\langle c_{ijkl}^S \right\rangle^{-1} \left\langle \sigma_{kl}^S \right\rangle \tag{2.43}$$

The components of the local stress tensor of an individual crystallite follow from:

$$\sigma_{ij}^S = c_{ijkl}^S \varepsilon_{kl}^S = c_{ijkl}^S \left\langle c_{klmn}^S \right\rangle^{-1} \left\langle \sigma_{mn}^S \right\rangle. \tag{2.44}$$

Obviously, equation (2.44) also holds in the laboratory frame of reference. By comparison of equation (2.44), with the superscript 'S' substituted by the superscript 'L', with equation (2.22), it can be concluded that

$$\Upsilon_{klmn}^L \left(hkl, \lambda, \varphi, \psi \right) = c_{klop}^L \left\langle c_{opmn}^L \right\rangle^{-1}. \tag{2.45}$$

Thus, the grain interaction tensor adopting the Voigt grain interaction model is given by equation (2.45).

Equation (2.45) can be rewritten recognising all dependencies:

$$\Upsilon_{klmn}^L \left(hkl, \lambda, \varphi, \psi \right) = c_{klop}^L \left(hkl, \lambda \right) \left(\left\langle c_{opmn}^L \right\rangle^{-1} \left(\varphi, \psi \right) \right) \tag{2.46}$$

where $\left\langle c_{opmn}^L \right\rangle^{-1} \left(\varphi, \psi \right)$ symbolises that $\left\langle c_{opmn}^L \right\rangle^{-1}$ in principle depends on $\left(\varphi, \psi \right)$. For an untextured specimen, $\left\langle c_{opmn}^L \right\rangle^{-1}$ is an isotropic tensor. In this case, equations (2.32) and (2.36) hold and then the Voigt model is an isotropic grain interaction model. In the case of a textured polycrystal, $\left\langle c_{opmn}^L \right\rangle^{-1}$ depends on φ and ψ and equations (2.32) and (2.33) do not hold. Consequently, a textured polycrystal obeying the Voigt grain interaction model is macroscopically elastically anisotropic.

2.3.4.3. Vook-Witt based grain interaction model

The equations for the components of the stress and strain tensor of individual crystallites cannot be given in an analytical form for the Vook-Witt based grain interaction model. Thus a formulation of an analytical solution for the grain interaction tensor $\Upsilon_{klmn}^L \left(hkl, \lambda, \varphi, \psi \right)$ is not possible. However, it is demonstrated that in this case $\Upsilon_{klmn}^L \left(hkl, \lambda, \varphi, \psi \right)$ depends on φ and ψ, even in the absence of texture. For a more detailed discussion of the Vook-Witt model, see also Chapter 3 and 4.

The analysis will be focused on a transversely isotropic thin film subject to a plane state of stress. Both the symmetry axis of the elastic properties and the one of the stress field are chosen parallel to the sample normal. The stress tensor reads:

$$\langle \sigma^S \rangle = \begin{pmatrix} \sigma_\parallel^S & 0 & 0 \\ 0 & \sigma_\parallel^S & 0 \\ 0 & 0 & 0 \end{pmatrix}, \tag{2.47}$$

with $\sigma_\parallel^S$ as the mechanical stress parallel to the surface. Only two mechanical elastic constants are necessary to characterise the mechanical elastic behaviour as only one (independent) component of the mechanical stress tensor and two (independent) components of the mechanical strain tensor, $\varepsilon_\parallel^S$ and $\varepsilon_\perp^S$, the mechanical strains parallel and perpendicular to the surface, respectively, are non-zero:

$$\langle \varepsilon^S \rangle = \begin{pmatrix} \varepsilon_\parallel^S & 0 & 0 \\ 0 & \varepsilon_\parallel^S & 0 \\ 0 & 0 & \varepsilon_\perp^S \end{pmatrix} \tag{2.48}$$

These elastic constants will be called A and B (cf. van Leeuwen *et al.*,1999, Chapter 3 and 4):

$$\varepsilon_\parallel^S = A\sigma_\parallel^S \tag{2.49}$$

$$\varepsilon_\perp^S = B\sigma_\parallel^S \tag{2.50}$$

The following grain interaction assumptions are adopted:

(i)   the strain is rotationally symmetric parallel to the surface and

(ii)   equal for all crystallites parallel to the surface and

(iii)   the stresses perpendicular to the surface are zero for all crystallites, i.e. the crystallites can deform freely in this direction.

This type of grain interaction model can be of special relevance for thin films (with a columnar microstructure) and for surface adjacent material (with grain boundaries oriented more or less perpendicular to the surface; cf. also discussion in Chapter 3 and 4).

The grain interaction assumptions ((i) – (iii)) fix parts of the stress and strain tensors (in the specimen frame of reference) for all crystallites:

$$\varepsilon^S = \begin{pmatrix} \varepsilon_\parallel^S & 0 & \Diamond \\ 0 & \varepsilon_\parallel^S & \Diamond \\ \Diamond & \Diamond & \Diamond \end{pmatrix}, \sigma^S = \begin{pmatrix} \Diamond & \Diamond & 0 \\ \Diamond & \Diamond & 0 \\ 0 & 0 & 0 \end{pmatrix}. \tag{2.51},(2.52)$$

The tensor components marked by $\Diamond$ are not explicitly specified for every crystallite, but these components can be calculated employing Hooke's law for every crystallite. To this end, it is convenient first to solve the following set of equations

$$\begin{pmatrix} s_{1112}^{S} & s_{1222}^{S} & 2s_{1212}^{S} \\ s_{1111}^{S} & s_{1122}^{S} & 2s_{1112}^{S} \\ s_{1122}^{S} & s_{2222}^{S} & 2s_{1222}^{S} \end{pmatrix} \begin{pmatrix} \sigma_{11}^{S} \\ \sigma_{22}^{S} \\ \sigma_{12}^{S} \end{pmatrix} = \begin{pmatrix} \varepsilon_{12}^{S} \\ \varepsilon_{11}^{S} \\ \varepsilon_{22}^{S} \end{pmatrix} \overset{def}{=} \begin{pmatrix} 0 \\ \varepsilon_{/\!/}^{S} \\ \varepsilon_{/\!/}^{S} \end{pmatrix} \tag{2.53}$$

for the missing stress tensor components:

$$\sigma_{11}^{S} = \varepsilon_{\|}^{S} \frac{s_{1222}^{S}\left(s_{1222}^{S} - s_{1211}^{S}\right) + s_{1212}^{S}\left(s_{1122}^{S} - s_{2222}^{S}\right)}{\Delta} \tag{2.54}$$

$$\sigma_{22}^{S} = \varepsilon_{\|}^{S} \frac{s_{1212}^{S}\left(s_{1211}^{S} - s_{1111}^{S}\right) + s_{1211}^{S}\left(s_{1211}^{S} - s_{1222}^{S}\right)}{\Delta} \tag{2.55}$$

$$\sigma_{12}^{S} = \frac{1}{2}\varepsilon_{\|}^{S} \frac{s_{1211}^{S}\left(s_{1111}^{S} - s_{1211}^{S}\right) + s_{1211}^{S}\left(s_{2222}^{S} - s_{1122}^{S}\right)}{\Delta} \tag{2.56}$$

where

$$\Delta \overset{def}{=} s_{1122}^{S}s_{1112}^{S}\left(s_{1212}^{S} - s_{1222}^{S}\right) - \left(s_{1112}^{S}\right)^{2}\left(s_{1222}^{S} + s_{2222}^{S}\right) + \\ s_{1111}^{S}\left(\left(s_{1222}^{S}\right)^{2} - s_{1212}^{S}s_{2222}^{S}\right) \tag{2.57}$$

is the determinant of the matrix in equation (2.53) (the symmetry of the compliance tensor has been used). Hereafter, the three missing strain tensor components of the specific crystallite can be calculated from the now complete stress tensor by applying Hooke's law. Equations (2.49) and (2.50) can be reformulated as

$$A = \frac{\varepsilon_{\|}^{S}}{\sigma_{\|}^{S}} = \frac{\left\langle \varepsilon_{11}^{S}\right\rangle}{\left\langle \sigma_{11}^{S}\right\rangle} = \frac{\iiint\limits_{G} \varepsilon_{11}^{S} f(g)dg}{\iiint\limits_{G} \sigma_{11}^{S} f(g)dg} \tag{2.58}$$

$$B = \frac{\varepsilon_{\perp}^{S}}{\sigma_{\|}^{S}} = \frac{\left\langle \varepsilon_{33}^{S}\right\rangle}{\left\langle \sigma_{11}^{S}\right\rangle} = \frac{\iiint\limits_{G} \varepsilon_{33}^{S} f(g)dg}{\iiint\limits_{G} \sigma_{11}^{S} f(g)dg} \tag{2.59}$$

indicating how the two mechanical elastic constants A and B can be calculated.

The effect of the direction dependent grain interaction assumptions on the linear transformation represented by the rank-4 tensor $\Upsilon_{klmn}^{L}\left(hkl, \lambda, \varphi, \psi\right)$ can be understood as follows: The linear transformation $\Upsilon_{klmn}^{L}\left(hkl, \lambda, \varphi, \psi\right)$ relating the stress tensor of an individual crystallite to the mechanical stress tensor (equation (2.22)), which cannot be written explicitly, can be replaced by a sequence of linear transformations (see figure 2.1): First, an orthogonal transformation ('1' in figure 2.1) rotates the mechanical stress tensor from the laboratory frame of reference to the specimen frame of reference. In the specimen frame of reference, where the grain interaction conditions have been formulated, the missing stress

tensor components for each crystallite ($\sigma_{11}^S, \sigma_{22}^S, \sigma_{12}^S = \sigma_{21}^S$) can be calculated by solving the system of equations (2.54), (2.55) and (2.56) after substituting $\varepsilon_{\parallel}^S$ by $A\sigma_{\parallel}^S$. Clearly, the solution of the system of equations (2.54), (2.55) and (2.56) depends on the orientation of the crystallite with respect to the specimen frame of reference, which is specified by $(hkl, \lambda, \varphi, \psi)$ (transformation '2' in figure 2.1). Finally, applying the inverse transformation ('3' in the figure) with respect to the above transformation yields the stress tensor of the crystallite in the laboratory frame of reference. Consequently, this σ^L depends on $(hkl, \lambda, \varphi, \psi)$ and $\langle \sigma^L \rangle$ (see also figure 2.1).

Thus, it holds:

$$\sigma^S(\mathbf{h}, \lambda, \varphi, \psi) \longleftarrow \langle \sigma^S \rangle = \begin{pmatrix} \sigma_{\parallel} & 0 & 0 \\ 0 & \sigma_{\parallel} & 0 \\ 0 & 0 & 0 \end{pmatrix}$$

2

3   **1**

$$\Upsilon$$

$$\sigma^L \qquad\qquad \longleftrightarrow \qquad\qquad \langle \sigma^L \rangle$$
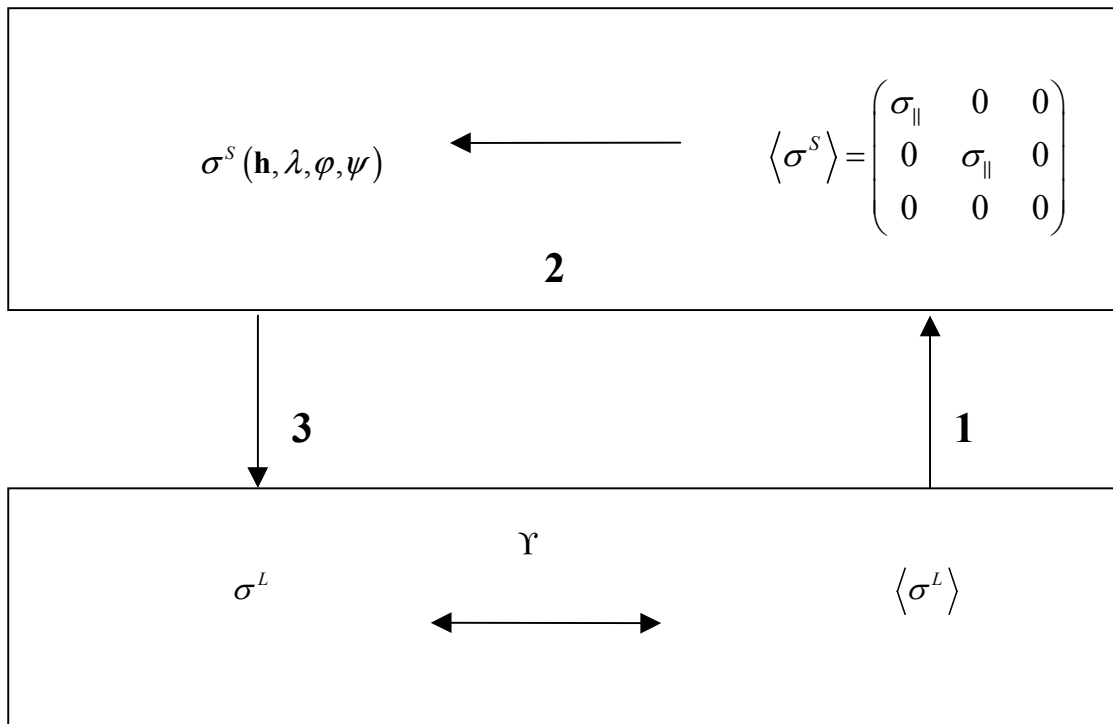
Figure 2.1: Schematic diagram of the transformations relating the stress in the sample system (upper box) to the stress in the laboratory system (lower box). Arrow 2 marks the linear transformation relating the mechanical stress in the sample system to the stress of individual crystallite. (i.e. solving a system of equations for the missing stress tensor components in the sample system). Note that the orientation of an individual crystallite is identified by specifying $(hkl, \lambda, \varphi, \psi)$, i.e. the transformation 2 depends on $(hkl, \lambda, \varphi, \psi)$.

$$\frac{\partial}{\partial \varphi} \Upsilon_{klmn}^L \left(hkl, \lambda, \varphi, \psi \right) \neq 0 \tag{2.60}$$

$$\frac{\partial}{\partial \psi} \Upsilon_{klmn}^L \left(hkl, \lambda, \varphi, \psi \right) \neq 0 \tag{2.61}$$

Therefore, the Vook-Witt based model is indeed a direction dependent grain interaction model. Then, even in the absence of texture, a polycrystal obeying the Vook-Witt grain interaction model is macroscopically elastically anisotropic.

2.4. Surface anisotropy as a special case of direction dependent grain interaction

Equation (2.14) is the basic equation adopted for diffraction stress analysis and holds for macroscopically elastically isotropic and anisotropic specimens. In the following for simplicity, a plane, principal state of stress in the specimen frame of reference an is imposed. Equation (2.14) can be straightforwardly reformulated as (cf. Stickforth, 1966):

$$\left\{\varepsilon_{33}^L\right\}_{\varphi\psi}^{hkl} = t_1 \left(hkl, \varphi, \psi, s^C, \Upsilon, f^*\right)\left(\left\langle \sigma_{11}^S \right\rangle + \left\langle \sigma_{22}^S \right\rangle\right) +$$
$$\tfrac{1}{2} t_2 \left(hkl, \varphi, \psi, s^C, \Upsilon, f^*\right)\sin^2 \psi \left(\left\langle \sigma_{11}^S \right\rangle \cos^2 \varphi + \left\langle \sigma_{22}^S \right\rangle \sin^2 \varphi\right) + \tag{2.62}$$
$$t_3 \left(hkl, \varphi, \psi, s^C, \Upsilon, f^*\right)\sin 2\varphi \left(\left\langle \sigma_{11}^S \right\rangle - \left\langle \sigma_{22}^S \right\rangle\right)$$

where:

$$t_1 \left(hkl, \varphi, \psi, s^C, \Upsilon, f^*\right) = A_{3322}^L \tag{2.63}$$

$$\tfrac{1}{2} t_2 \left(hkl, \varphi, \psi, s^C, \Upsilon, f^*\right)\sin^2 \psi =$$
$$\left(A_{3333}^L - A_{3311}^L\right)\sin^2 \psi + A_{3311}^L - A_{3322}^L + A_{3313}^L \sin 2\psi \tag{2.64}$$

$$t_3 \left(hkl, \varphi, \psi, s^C, \Upsilon, f^*\right) = -A_{3312}^L \cos \psi - A_{3323}^L \sin \psi \tag{2.65}$$

Here it should be noted that Stickforth (1966) was the first to propose an equation like equation (2.62). It should also be noted that equation (2.62) is a fully equivalent, alternative reformulation of equation (2.16) (for the case of a plane, principle state of stress).

The A's in equations (2.63), (2.64) and (2.65) depend on $hkl, \varphi, \psi, s^C, \Upsilon$ and f^*. The factors t_1, $\tfrac{1}{2} t_2$ and t_3 might be named 'diffraction (X-ray) elastic constants' with reference to the traditional $\sin^2 \psi$-law (cf. equation (2.12)): t_1 takes the place of S_1^{hkl} and $\tfrac{1}{2} t_2$ takes the place of $\tfrac{1}{2} S_2^{hkl}$; for t_3 there is no equivalent in the traditional $\sin^2 \psi$-law. For the case of macroscopic elastic isotropy t_3 equals zero and t_1 and $\tfrac{1}{2} t_2$ are then equal to the X-ray elastic

constants S_1^{hkl} and $\frac{1}{2}S_2^{hkl}$. However, it should be recognised that, in contrast with S_1^{hkl} and $\frac{1}{2}S_2^{hkl}$, in general t_1, $\frac{1}{2}t_2$ and t_3 depend on φ and ψ: i.e. curvature occurs in the $\sin^2\psi$-plots.

Surface anisotropy was first considered by Stickforth (1966) as a source of macroscopic elastic anisotropy: the elastic behaviour of crystallites located adjacent to the surface of a polycrystal can be different from the elastic behaviour of crystals located at some distance from the surface. In the bulk of a polycrystal, each crystallite is surrounded by other crystallites in three dimensions, whereas crystallites located at the surface of a polycrystal have no neighbouring crystallites in the direction perpendicular to the surface. Thus, for the crystallites adjacent to the surface not all directions may be equivalent for the interaction of the grains.

Experimental investigations on the possible occurrence of surface anisotropy were performed by, for example, Nikolin (1983) and Hauk, Nikolin & Weisshaupt (1985). Hauk (1997) summarised various publications and concluded (see also Hartmann, 1973, Nikolin, 1983) that, if surface anisotropy is a genuine physical phenomenon, the surface region of a polycrystal affected by surface anisotropy must have a thickness of less than 400nm.

The first evidence of direction dependent grain interaction was obtained only very recently in the diffraction stress analysis of an untextured, polycrystalline thin film in a plane state of stress (van Leeuwen *et al.*, 1999). The apparent lack of convincing proof of distinct surface anisotropy in the diffraction analysis of the surface region of bulk specimens may be understood as follows: Straightforward diffraction evidence of direction dependent grain interaction is obtained if deviations of straight line behaviour occurs in $\sin^2\psi$-plots for untextured specimens in a plane state of stress (see equation (2.62)). Indeed this is the line of reasoning followed by van Leeuwen *et al.* (1999) in their work on a stressed thin film.

However, non-linear behaviour in $\sin^2\psi$-plots can also be explained on the basis of more complicated states of stress, the occurrence of texture and/or the occurrence of stress depth gradients. It is not unlikely that the unavailability of an appropriate direction dependent grain-interaction model (as, for example, the Vook-Witt based model proposed for diffraction stress analysis by van Leeuwen *et al.* (1999) ; see also this work, Chapter 3. and Chapter 4.), and the tendency to either ignore non-linearities in measured $\sin^2\psi$-plots or to focus on interpretation invoking shear components, texture effects and/or stress depth gradients, has obstructed the recognition of the significance of surface anisotropy for (also) bulk specimens. This work may breathe new life into that research.

2.5. Summary

- Diffraction analysis of stress is based on an (assumed) linear transformation of the macroscopic mechanical stress tensor into the local stress tensor of a crystallite in a polycrystalline specimen. This linear transformation is achieved by the grain interaction tensor.

- In case of macroscopic elastic isotropy diffraction stress analysis can be performed employing the concept of diffraction (X-ray) elastic constants.

- In case of macroscopic elastic anisotropy, i.e. in the presence of preferred orientation and/or direction dependent grain interaction, diffraction stress analysis can be performed employing the concept of diffraction (X-ray) stress factors.

- A specimen can exhibit isotropic grain interaction and macroscopically elastically anisotropic behaviour at the same time due to the occurrence of texture.

- The Vook-Witt based grain interaction model, recently proposed as the first, explicit direction dependent grain interaction model for diffraction stress analysis of thin films, has relevance for the phenomenon of surface anisotropy of bulk specimens. Observations of non-linearities in $\sin^2\psi$-plots may need reinterpretation recognising the role of the surface anisotropy.

Appendix 2.1. Calculation of the components of the stress tensor in the laboratory frame of reference from the stress components in the specimen frame of reference

The laboratory frame of reference is related to the specimen frame of reference by the three Euler angles φ, and ψ and η (η is not needed in the following). The order of rotations is: (i) rotation around S_3 axis by φ; the new frame of reference will be referred to as the S' frame of reference. (ii) rotation around S'_2 axis by ψ.

The individual rotations can be realised by rotation matrices:

$$a_\varphi = \begin{pmatrix} \cos\varphi & \sin\varphi & 0 \\ -\sin\varphi & \cos\varphi & 0 \\ 0 & 0 & 1 \end{pmatrix} \tag{2A1}$$

$$a_\varphi = \begin{pmatrix} \cos\psi & 0 & -\sin\psi \\ 0 & 1 & 0 \\ \sin\psi & 0 & \cos\psi \end{pmatrix} \tag{2A2}$$

The matrix for the transformation from the specimen frame of reference to the laboratory frame of reference $\Omega^{L\leftarrow S}$ is the product of the two matrices:

$$\Omega^{L\leftarrow S} = a_\psi a_\varphi \tag{2A3}$$

Hence, the mechanical stress tensor in the laboratory frame of reference can be calculated from the mechanical stress tensor in the specimen frame of reference:

$$\left\langle \sigma^L \right\rangle = \Omega^{L\leftarrow S} \left\langle \sigma^S \right\rangle \left(\Omega^{L\leftarrow S} \right)^T . \tag{2A4}$$

Appendix 2.2. Consequences of macroscopic elastic isotropy for the grain interaction tensor

The calculation of $A_{ijkl}^{L'}\left(hkl,\varphi,\psi,s^{C},\Upsilon\right)$ (in the absence of texture) can be reformulated as follows:

$$
A_{ijkl}^{L'}\left(hkl,\varphi,\psi,s^{C},\Upsilon\right)=\frac{\displaystyle\int_{0}^{2\pi} s_{ijmn}^{L'}\left(hkl,\lambda'\right)\Upsilon_{mnkl}^{L'}\left(hkl,\lambda'\right)d\lambda'}{2\pi}=
$$

$$
=\frac{\displaystyle\int_{0}^{2\pi}\Delta_{im}^{\delta}\Delta_{jn}^{\delta}\Delta_{qo}^{\delta}\Delta_{rp}^{\delta}s_{mnop}^{L}\left(hkl,\lambda+\delta\right)\Delta_{qs}^{\delta}\Delta_{rt}^{\delta}\Delta_{ku}^{\delta}\Delta_{lv}^{\delta}\Upsilon_{stuv}^{L}\left(hkl,\lambda+\delta\right)d\lambda}{2\pi}
$$

(2A5)

$A_{ijkl}^{L'}\left(hkl,\varphi,\psi,s^{C},\Upsilon\right)$ in equation (2A5) can only be identical to $A_{ijkl}^{L}\left(hkl,\varphi,\psi,s^{C},\Upsilon\right)$ if:

$$
\Delta_{im}^{\delta}\Delta_{jn}^{\delta}\Delta_{ko}^{\delta}\Delta_{lp}^{\delta}\Upsilon_{mnop}^{L}\left(hkl,\lambda+\delta\right)=\Upsilon_{ijkl}^{L}\left(hkl,\lambda\right)
$$

(2A6)

as

$$
\Delta_{im}^{\delta}\Delta_{jn}^{\delta}\Delta_{ko}^{\delta}\Delta_{lp}^{\delta}s_{mnop}^{L}\left(hkl,\lambda+\delta\right)=s_{ijkl}^{L}\left(hkl,\lambda\right).
$$

(2A7)

Equation (2A7) is the transformation rule for the compliance tensor, which holds always. Equation (2A6) expresses a condition for the grain interaction for macroscopically elastically isotropic specimens.

3. Diffraction analysis of internal strain/stress fields in textured transversely isotropic thin films; theoretical basis and simulation

M. Leoni, U. Welzel, P. Lamparter, E. J. Mittemeijer & J.-D. Kamminga

Abstract

Polycrystalline films produced via physical vapour deposition often possess a microstructure composed of columnar oriented grains. From the mechanical point of view, they cannot be treated as isotropic bulk solids; rather their elastic macroscopic behaviour is only transversely isotropic. In this context, the effect of texture on the elastic response of such films has been investigated for different grain interaction models. In particular, the determination of macroscopic stress by X-ray diffraction methods has been analysed. Traditional grain-interaction models as those due to Voigt and Reuss, have been compared with the one proposed by Vook and Witt, compatible with the presence of only transverse isotropy of the body (even in the absence of crystallographic texture). By simulation, it has been demonstrated that, although texture only moderately affects the values of the macroscopic mechanical elastic constants of the transversely isotropic body, it can pronouncedly influence the results from the X-ray diffraction measurements. This effect is shown to depend strongly on the type of grain interaction.

3.1. Introduction

Knowledge of the internal strain/stress fields in thin deposits is of key importance for optimising the corresponding production process and service life. De-adhesion failure and surface-quality dependent properties such as hardness, wear and corrosion resistance are highly dependent on the presence of stresses in the deposited layer (Machlin, 1995).

X-ray diffraction is a powerful tool for the non-destructive measurement of the internal stresses in thin films. Various methods based on X-ray diffraction have been presented for the analysis of macroscopically mechanically isotropic (sometimes termed as *quasi-isotropic* (Hauk, 1997)) bodies subjected to homogeneous (Noyan & Cohen, 1987, Hauk, 1997, Kamminga *et al.,* 2000) or depth-dependent (Sasaki *et al.,* 1993, Genzel, 1994, 1997, 1998, Hauk, 1997, Leoni, 1998, Leoni *et al.,* 1999, Scardi *et al.,* 1999) strain/stress

fields. Special procedures, like the Crystallite Group Method (CGM; see e.g. Hauk, 1997), have been proposed for the diffraction stress analysis of specimens exhibiting distinct macroscopic anisotropy due to texture.

Owing to their microstructure, thin films cannot usually be considered as macroscopically isotropic. Thin films produced via Physical Vapour Deposition provide a good example, as they are often composed of columnar grains aligned along a preferential direction usually parallel to the surface normal (Machlin, 1995). In this manner, they can exhibit rotational symmetry of the macroscopic (elastic) properties with respect to the surface normal. From the microstructural crystallographic point of view, such films show a *fibre texture* (see for instance Bunge, 1982a), while from the mechanical (macroscopic) point of view, they can be considered as transversely isotropic (Love, 1927, van Leeuwen *et al.,* 1999). All macroscopically isotropic bodies are obviously also macroscopically transversely isotropic, whereas the reverse does *not* necessarily hold. It should be noted that also in the absence of crystallographic texture only transverse isotropy on a macroscopic scale can occur (van Leeuwen *et al.,* 1999).

The macroscopic elastic response of a polycrystalline aggregate differs, in general, from that of a single crystal. By means of suitable models, the macroscopic elastic behaviour of a polycrystalline material (as given by the *full* macroscopic compliance or stiffness tensors) can be calculated from single-crystal elastic data.

In the absence of texture, the most common models, due to Voigt, Reuss, Neerfeld-Hill or Eshelby-Kröner (see for instance Noyan & Cohen, 1987, Hauk, 1997, van Leeuwen *et al.,* 1999) predict macroscopic mechanical isotropy for the aggregate. Thus, if these models are used for the description of an only transversely isotropic untextured thin film, the symmetry of the calculated macroscopic elastic tensor is higher than that really presented by the specimen.

Vook and Witt have presented an alternative grain interaction model that can be used for the analysis of a thin film with the symmetry axis parallel to the surface normal in the sixties (Vook & Witt, 1965, Witt & Vook, 1968). The Vook-Witt model was originally intended for the study of thermal stresses in thin films. As such, it was used and in some way extended by several investigators (Murakami & Yogi, 1985, Wieder, 1995a-c, 1996), but in most cases it was applied erroneously in the analysis of diffraction data. Only recently (van Leeuwen *et al.,* 1999), the model was revisited, elaborated and adapted to the analysis of residual stresses in thin films using X-ray diffraction. However, the consequences of crystallographic texture have not been considered until now. In the present paper, the

approach by van Leeuwen *et al.,* (1999) is extended to textured films. To demonstrate the distinct influence of texture on the strain data obtained from a diffraction experiment, simulations have been conducted for various materials covering a large range of elastic (single crystal) anisotropy. In this way the large differences become apparent between the values of the stress components obtained by application of the traditional diffraction methods and the actually imposed stress field. Therefore, a more appropriate analysis of diffraction strain data can be proposed.

3.2. Theoretical basis

3.2.1. Mechanical and diffraction response of transversely isotropic films

An elaboration of the Vook-Witt hypotheses and their application to the diffraction analysis of (macro)stress in randomly oriented (textureless) thin films, has been recently presented by van Leeuwen *et al.* (1999). The essentials will be briefly summarised here.

In order to describe the orientation of a crystallite within the specimen, and its relations with the experimental apparatus, three Cartesian reference frames are usually considered: the crystal (*C*), sample (*S*) and laboratory (*L*) systems (see figure 3.1 and Appendix 3.1). A suitable superscript, indicating the corresponding reference (basis), will be given to the representation in components of a rank-*n* tensor (e.g. ε_{ij}^S is the (i,j) component of the strain tensor represented in the *S* system). The transformation from one to another basis is accomplished by means of suitable rotation (orthonormal) matrices (further details are presented in Appendix 3.1; similar conventions as in van Leeuwen *et al.* (1999) are adopted).

Adopting the Einstein notation (i.e. summation over repeated indices (Nye, 1957)), Hooke's law can be written for every crystallite in the sample, as:

$$\varepsilon_{ij}^S = s_{ijkl}^S \sigma_{kl}^S \tag{3.1}$$

Equation (3.1) represents a system of six relations between six ε_{ij}^S and six σ_{ij}^S (i.e. there are 12 unknowns). From a mathematical point of view, the stress and strain tensors are fully determined if six more independent equations are given. These additional hypotheses are provided by adopting a suitable *grain interaction model* i.e. by assigning, to six of the unknowns, values independent of the orientation of the crystallite in the *S* system.
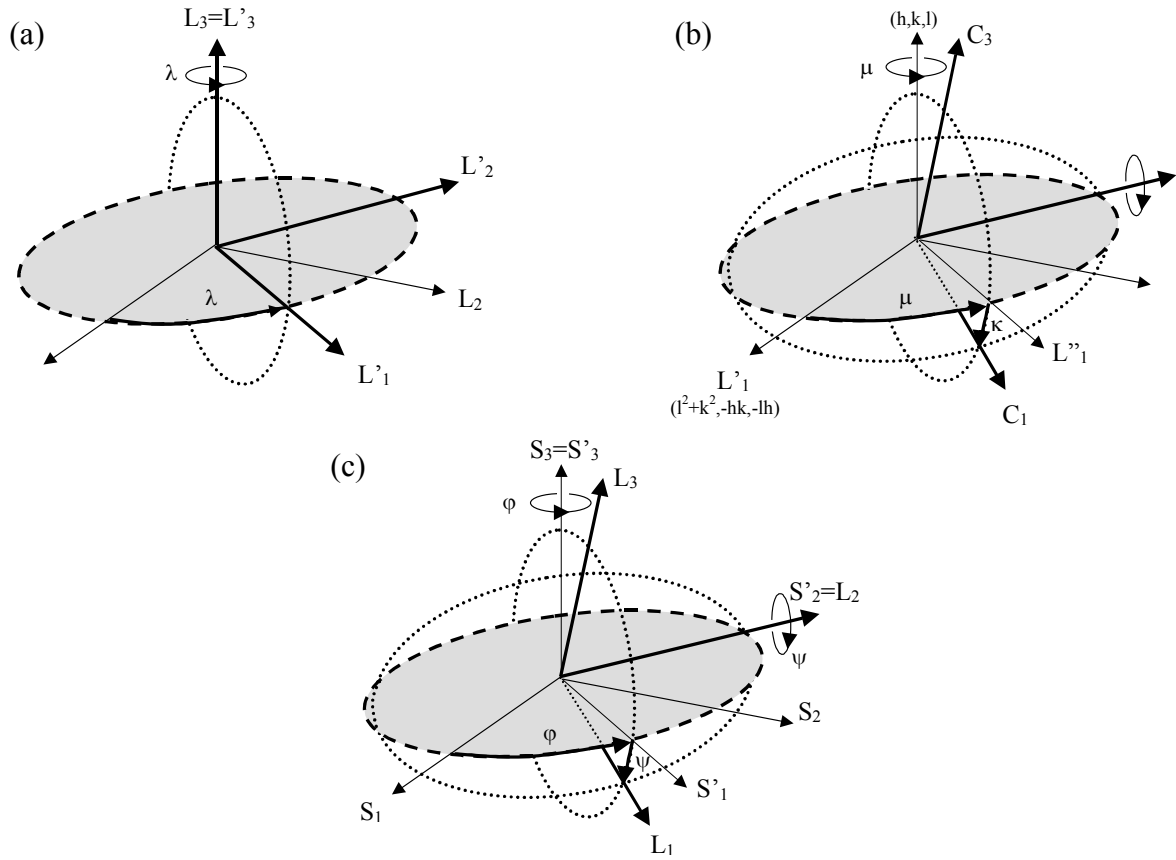
Figure 3.1: Definition of and relations between the crystal (*C*), sample (*S*) and laboratory (*L*) reference frames. (a) Relation between the *L* system and the intermediate *L'* system. (b) Transformation between the *L'* system and the *C* system through the intermediate system *L"*. (c) Transformation between the *S* system and the *L* system through the intermediate system *S"*.

The analysis will be focused on a transversely isotropic thin film subject to a plane state of stress. Both the symmetry axis of the elastic properties and the one of the stress field are chosen parallel to the sample normal. Mechanical equilibrium requires the macroscopic average stress components perpendicular to the sample surface to be zero. Denoting by $\langle \; \rangle$ the volume-weighed averaging over all *occurring* crystallite orientations, mechanical equilibrium for the thin film thus implies:

$$\langle \sigma_{i3}^{S} \rangle = \langle \sigma_{3i}^{S} \rangle = 0 \qquad (3.2)$$

The film is free to expand along its normal, and the average strain along that direction is:

$$\langle \varepsilon_{33}^{S} \rangle \overset{def}{=} \varepsilon_{\perp}^{S} \qquad (3.3)$$

Due to the transverse isotropy, the rotational symmetry of the stress field as expressed by

$$\left\langle \sigma_{11}^{S} \right\rangle = \left\langle \sigma_{22}^{S} \right\rangle \overset{def}{=} \sigma_{\parallel}^{S} \qquad\qquad \left\langle \sigma_{12}^{S} \right\rangle = \left\langle \sigma_{21}^{S} \right\rangle = 0 \qquad\qquad (3.4)$$

induces a rotational symmetry of the strain field:

$$\left\langle \varepsilon_{11}^{S} \right\rangle = \left\langle \varepsilon_{22}^{S} \right\rangle \overset{def}{=} \varepsilon_{\parallel}^{S} \qquad\qquad \left\langle \varepsilon_{12}^{S} \right\rangle = \left\langle \varepsilon_{21}^{S} \right\rangle = 0 \qquad\qquad (3.5)$$

Five independent elastic constants suffice to completely describe the *macroscopic* elastic behaviour of a transversely isotropic body (Love, 1927, Hendrix and Yu, 1998, Leigh and Berndt, 1999). The relations (3.2)-(3.5) do not permit the determination of all these five constants (using Hooke's law). However, only two elastic constants are required to fully describe the relation between the stress and strain tensors for a transversely isotropic body subjected to a plane state of stress (symmetry axis parallel to the sample normal): only two strain tensor components and one stress tensor component are independent and non-zero. Thus:

$$\varepsilon_{\parallel}^{S} = \mathrm{A}\sigma_{\parallel}^{S} \qquad\qquad (3.6)$$

$$\varepsilon_{\perp}^{S} = \mathrm{B}\sigma_{\parallel}^{S} \qquad\qquad (3.7)$$

where A and B are *mechanical elastic constants*, i.e. macroscopic averages of the elastic compliance tensor over all crystallites constituting the transversely isotropic body.

The average *mechanical* strain and stress tensor components in the S system are obtained by integrating the respective tensor components over all the crystallites composing the sample (this is equivalent with taking a single crystallite and integrating over all its possible, i.e. occurring, orientations in space). The orientation of each crystallite in the S system can be univocally identified by three Euler angles; the convention of Roe in the definition of these angles will be adopted (Roe & Krigbaum, 1964). In accordance with Matthies *et al.* (1987, 1988), the three angles will be called α,β,γ. It is usual to associate a set of Euler angles to a vector $\vec{g} = (\alpha,\beta,\gamma)$ in the three-dimensional orientation (Euler) space G (more details are given in Appendix 3.1). In this way, each point in the orientation space represents a possible orientation of the C system with respect to the S system.

Given the vector $\vec{g} = (\alpha,\beta,\gamma)$ in G, the volume fraction $dV(\vec{g})/V$ of crystallites in the infinitesimal orientation range $d^3g = \sin(\beta)d\alpha d\beta d\gamma$ around $\vec{g}$, is provided by the Orientation Distribution Function (ODF) $f(g)$ according to:

$$\frac{dV(\vec{g})}{V} = \frac{f(\vec{g})}{8\pi^2}d^3g = \frac{f(\alpha,\beta,\gamma)}{8\pi^2}\sin(\beta)d\alpha d\beta d\gamma \qquad\qquad (3.8)$$

Owing to this definition, the ODF is a probability density (cf. Matthies *et al.*, 1987), and it holds:

$$\iiint\limits_{G} \frac{f\left(\vec{g}\right)}{8\pi^2} d^3g = 1 \tag{3.9}$$

With these definitions, the average value of the (i,j) component of a rank-2 tensor Ω (in this case, ε or σ) in the S system, is given in terms of Euler angles by the three-fold integral:

$$\left\langle \Omega_{ij}^S \right\rangle = \frac{\iiint\limits_{G} \Omega_{ij}^S \frac{f\left(\vec{g}\right)}{8\pi^2} d^3g}{\iiint\limits_{G} \frac{f\left(\vec{g}\right)}{8\pi^2} d^3g} = \frac{1}{8\pi^2} \iiint\limits_{G} \Omega_{ij}^S f\left(\vec{g}\right) d^3g =$$

$$\frac{1}{8\pi^2} \int\limits_{\gamma=0}^{2\pi} \int\limits_{\beta=0}^{\pi} \int\limits_{\alpha=0}^{2\pi} \Omega_{ij}^S f(\alpha,\beta,\gamma)\sin(\beta)\,d\alpha\,d\beta\,d\gamma \tag{3.10}$$

All strain and stress tensor components can be averaged in this way, but a grain interaction model is needed for actual computation of the values (see discussion below equation (3.1) and Chapter 3.2.3).

On this basis, equations (3.6) and (3.7) can be reformulated:

$$A = \frac{\varepsilon_{\parallel}^S}{\sigma_{\parallel}^S} = \frac{\left\langle \varepsilon_{11}^S \right\rangle}{\left\langle \sigma_{11}^S \right\rangle} = \frac{\iiint\limits_{G} \varepsilon_{11}^S f\left(\vec{g}\right) d^3g}{\iiint\limits_{G} \sigma_{11}^S f\left(\vec{g}\right) d^3g} \tag{3.11}$$

$$B = \frac{\varepsilon_{\perp}^S}{\sigma_{\parallel}^S} = \frac{\left\langle \varepsilon_{33}^S \right\rangle}{\left\langle \sigma_{11}^S \right\rangle} = \frac{\iiint\limits_{G} \varepsilon_{33}^S f\left(\vec{g}\right) d^3g}{\iiint\limits_{G} \sigma_{11}^S f\left(\vec{g}\right) d^3g} \tag{3.12}$$

permitting the value for the two mechanical elastic constants A and B to be calculated if the ODF, i.e. the texture, is known.

As discussed in the introduction, (X-ray) diffraction affords a measure of the macroscopic deformation in solids. However, it does not provide a direct evaluation of the average stress/strain in the whole sample, in the sense of equation (3.10). A diffraction line contains data on only a subset of the crystallites for which the diffracting planes are perpendicular to the chosen measurement direction. Because only the direction of the diffraction vector is defined, a degree of freedom occurs for the diffracting crystallites: the rotation around the diffraction vector (denoted by the angle λ). Thus the diffraction experiment is insensitive to features perpendicular to the diffraction vector and an average

over these crystallites is observed experimentally. Hence, the *diffraction strain* is in general not equal to the overall *mechanical strain*.

In a diffractometer, the measurement direction, i.e. the orientation of the diffraction vector with respect to the sample surface normal, is indicated by two angles ψ and φ. The tilt of the sample with respect to the diffraction plane is indicated by ψ, while φ denotes the rotation of the sample around its surface normal. For a textured specimen the average strain in the measurement direction of the diffraction experiment for the *hkl* reflection is given by:

$$\varepsilon_{\varphi,\psi}^{hkl} = \left\langle \varepsilon_{33}^{L} \right\rangle = \left\langle s_{33kl}^{L} \sigma_{kl}^{L} \right\rangle = \frac{\int_{0}^{2\pi} \varepsilon_{33}^{L} f^{*}(hkl,\lambda,\varphi,\psi) d\lambda}{\int_{0}^{2\pi} f^{*}(hkl,\lambda,\varphi,\psi) d\lambda} \tag{3.13}$$

where $f^{*}(hkl,\lambda,\varphi,\psi)$ is the representation of the ODF in terms of the measurement parameters. The ODF as defined in equation (3.8) cannot be directly used in equation (3.13) in analogy to equation (3.10) since the angles λ,φ,ψ are *not* Euler angles representing a rotation of the *C* system with respect to the *S* system (in fact they provide the rotation of the system *L* with respect to the system *S*). However, the rotation matrix a^{CS} is known in terms of the measurement angles φ, ψ, and of *hkl* and λ (see Appendix 3.1 for application to cubic materials). The same rotation in terms of Euler angles is represented by a rotation matrix associated to $\vec{g} = (\alpha,\beta,\gamma)$ (see Appendix 3.1); by equating this matrix to a^{CS}, the values of α, β, γ and thus $f(\alpha,\beta,\gamma)$ at every λ can be determined, to be finally substituted for $f^{*}(hkl,\lambda,\varphi,\psi)$ in equation (3.13).

A simplification of (3.13) is possible if the ODF exhibits symmetry. A typical example is the case of the so-called *fibre texture*, i.e. the texture is rotationally symmetric around the sample surface normal (see, for instance, Roe & Krigbaum, 1964). Due to this rotational symmetry, the measured strain becomes independent of the rotation φ. In terms of the Euler angles α, β, γ, the presence of a revolution axis causes the ODF to loose its dependence on α (the angle α is the rotation of the *C* system around the S_3 axis, i.e. the sample surface normal).

To describe the measured lattice strain values in terms of the macroscopic stress/strain fields acting on the sample, equation (3.13) should contain quantities defined in the sample S system. By using Hooke's law and the appropriate tensor rotations, equation (3.13) is transformed into the following basic relation for the diffraction stress analysis of fibre textured films (note that in this case $\varepsilon_{\varphi,\psi}^{hkl} = \varepsilon_{\psi}^{hkl}$):

$$\varepsilon_{\psi}^{hkl} = \frac{\int\limits_0^{2\pi} a_{3i}^{LS} a_{3j}^{LS} a_{im}^{SC} a_{jn}^{SC} a_{ko}^{SC} a_{lp}^{SC} s_{mnop}^C \sigma_{kl}^S f^*\left(hkl,\lambda,\psi\right)d\lambda}{\int\limits_0^{2\pi} f^*(hkl,\lambda,\psi)d\lambda} \tag{3.14}$$

where a_{ij}^{LS} and a_{ij}^{SC} are the direction cosines in the corresponding rotation matrices (for cubic materials see Appendix 3.1 for more details).

When, for a given set of *hkl* and ψ in equation (3.14), the number of diffracting crystallites is zero, then $f^*(hkl,\lambda,\psi)=0$ independent of λ and, obviously, the corresponding ε_{ψ}^{hkl} cannot be evaluated by the diffraction experiment.

The stress tensor components σ_{kl}^S to be used in equation (3.14) can be calculated only if a grain interaction model is adopted.

3.2.2. The Vook-Witt grain interaction assumptions

Calculations of the average stress/strain tensors, and thus of the constants A and B as well as the diffraction response, require adoption of a grain interaction model (cf. discussion of equation (3.1)). In a thin film (irrespective of texture), the perpendicular direction and the in-plane directions differ on a macroscopic scale. This is compatible with the assumptions of the Vook-Witt grain interaction model:

(*i*)   the film is subject to a strain field possessing a rotational symmetry axis parallel to the sample normal;

(*ii*)   the in-plane strain components are equal for all crystallites;

(*iii*)   the stresses perpendicular to the film are zero for all crystallites;

Under these hypotheses, equations (3.2)-(3.5) for the stress and strain values in *each* crystallite become:

$$\left.\begin{aligned} \varepsilon_{11}^S &= \varepsilon_{22}^S \overset{def}{=} \varepsilon_{//}^S \\ \varepsilon_{12}^S &= \varepsilon_{21}^S \overset{def}{=} 0 \\ \sigma_{i3}^S &= \sigma_{3i}^S \overset{def}{=} 0 \end{aligned}\right\} \tag{3.15}$$

These equations, setting for each crystallite σ_{i3}^S, ε_{11}^S, ε_{22}^S and ε_{12}^S to values independent of its orientation, provide the six additional independent relations (cf. discussion of equation (3.1)) that permit (for each crystallite) calculation of the full stress and strain tensors.

3.2.3. Evaluation of A and B and the diffraction strain

A and B as well as the diffraction response of the body can be calculated from equations (3.11), (3.12), and (3.13). To this end strain and stress tensor components in the S system have to be calculated for all occurring crystals, using equation (3.1).

For traditional models (Reuss, Voigt) the procedure is straightforward, since either the full stress or the full strain tensors are imposed to be the same, in the S frame, for all crystallites (for details see Appendix 3.2). The procedure becomes more tedious for the Vook-Witt grain-interaction model (van Leeuwen $et\ al.$, 1999). Since the compliance tensor for all crystallites in the S system is known (calculated by suitable rotation of s^C for which literature values are available), combining the Vook-Witt model (see also equation (3.15)) with Hooke's law permits the calculation of three non-zero stress tensor components of a crystallite in the S system according to:

$$
\begin{pmatrix} s_{1112}^S & s_{1222}^S & 2s_{1212}^S \\ s_{1111}^S & s_{1122}^S & 2s_{1112}^S \\ s_{1122}^S & s_{2222}^S & 2s_{1222}^S \end{pmatrix}
\begin{pmatrix} \sigma_{11}^S \\ \sigma_{22}^S \\ \sigma_{12}^S \end{pmatrix} =
\begin{pmatrix} \varepsilon_{12}^S \\ \varepsilon_{11}^S \\ \varepsilon_{22}^S \end{pmatrix}
\overset{def}{=}
\begin{pmatrix} 0 \\ \varepsilon_\parallel^S \\ \varepsilon_\parallel^S \end{pmatrix}
\tag{3.16}
$$

and, analogously, the three not-imposed strain tensor terms from:

$$
\begin{pmatrix} s_{1311}^S & s_{1322}^S & 2s_{1312}^S \\ s_{2311}^S & s_{2322}^S & 2s_{2312}^S \\ s_{3311}^S & s_{3322}^S & 2s_{3312}^S \end{pmatrix}
\begin{pmatrix} \sigma_{11}^S \\ \sigma_{22}^S \\ \sigma_{12}^S \end{pmatrix} =
\begin{pmatrix} \varepsilon_{13}^S \\ \varepsilon_{23}^S \\ \varepsilon_{33}^S \end{pmatrix}
\tag{3.17}
$$

The symmetry of the compliance tensor s has been used in these equations. The desired stress components can be obtained easily by matrix inversion from equation (3.16) and, due to the simple nature of the problem, an analytical solution of equation (3.16) is readily obtained:

$$
\sigma_{11}^S = \varepsilon_\parallel^S \frac{s_{1222}^S \left(s_{1222}^S - s_{1211}^S \right) + s_{1212}^S \left(s_{1122}^S - s_{2222}^S \right)}{\Delta}
\tag{3.18}
$$

$$
\sigma_{22}^S = \varepsilon_\parallel^S \frac{s_{1212}^S \left(s_{1211}^S - s_{1111}^S \right) + s_{1211}^S \left(s_{1211}^S - s_{1222}^S \right)}{\Delta}
\tag{3.19}
$$

$$
\sigma_{12}^S = \frac{1}{2} \varepsilon_\parallel^S \frac{s_{1211}^S \left(s_{1111}^S - s_{1211}^S \right) + s_{1211}^S \left(s_{2222}^S - s_{1122}^S \right)}{\Delta}
\tag{3.20}
$$

where

$$
\Delta \overset{def}{=} s_{1122}^S s_{1112}^S (s_{1212}^S - s_{1222}^S) - (s_{1112}^S)^2 (s_{1222}^S + s_{2222}^S) + s_{1111}^S ((s_{1222}^S)^2 - s_{1212}^S s_{2222}^S)
\tag{3.21}
$$

is the determinant of the matrix in equation (3.16).

From equation (3.17), the missing strain tensor components can then be calculated.

A and B are calculated by imposing an (arbitrary) macroscopic in-plane strain $\varepsilon_\parallel^S$ (the elastic constants A and B are obviously independent of the actual strain/stress state which must be compatible with the loading conditions according to equations (3.2)-(3.5)). Using equations (3.16) to (3.21) the unknowns in the equations (3.11) and (3.12) ($\sigma_{11}^S, \varepsilon_{33}^S$) can be calculated for each crystallite (each orientation) and the evaluation of the integrals in equations (3.11) and (3.12) is then possible.

The diffraction strain for a given reflection and a given stress/strain state is calculated as a function of $\sin^2\psi$ in an analogous way by imposing a macroscopic strain $\varepsilon_\parallel^S$ and calculating the stress tensor components σ_{kl}^S for each crystallite (each orientation) from equation (3.16). The integral in equation (3.14) can then be calculated (see Appendix 3.1 for the definition of the rotational matrices).

As a concluding note it is remarked that the elastic constant s^L appearing in equation (3.13) is, for each ψ tilting, dependent on λ and *cannot* be evaluated just once, as holds for the traditional Reuss grain interaction model (as was erroneously done by Diz & Humbert, 1992 and Wieder, 1995a, 1995b, 1995c, 1996). Since only in the Reuss limit σ_{kl}^S is a constant (i.e. the same for each grain), the following relation then holds (cf. equation (3A10))

$$\left\langle \varepsilon_{33}^L \right\rangle = \left\langle s_{33kl}^L \sigma_{kl}^L \right\rangle = \left\langle s_{33kl}^L \right\rangle \left\langle \sigma_{kl}^L \right\rangle \tag{3.22}$$

and one set $\left\langle s_{33kl}^L \right\rangle$ suffices.

In the case of the adopted Vook-Witt grain-interaction model, due to the particular (mixed) nature of the grain interaction conditions (cf. equation (3.15)), it is immediately clear that equation (3.22) cannot hold.

3.3. Simulations

Based on equation (3.14), simulations of diffraction measurements have been carried out for different cubic materials characterised by different extents of elastic anisotropy, defined by the parameter A_i:

$$A_i = \frac{\left(s_{1111}^C - s_{1122}^C \right)}{2 s_{1212}^C} \tag{3.23}$$

Tungsten (A_i=1.00), niobium (A_i=0.49) and gold (A_i=2.85) were selected for the simulations: the respective single-crystal elastic constants corresponding to the *C* system have been collected in table 3.1.

For most of the known materials, the anisotropy is in the range defined here by the 'limiting' values of A_i for niobium and gold. For each material, the expected (X-ray) diffraction strain was calculated (equation (3.14)) as function of $\sin^2 \psi$ (the so-called *$sin^2 \psi$ plot*), for a number of reflections. The calculations were performed assuming an average stress $\sigma_\parallel^S = 100$MPa for the film. Note that this average stress can be transferred immediately to the average strain parallel to the substrate $\varepsilon_\parallel^S$ from equation (3.11) and to the strain perpendicular to the substrate $\varepsilon_\perp^S$ from equation (3.12), when the elastic constants A and B are known.

The $\sin^2 \psi$ plot is a traditional way of X-ray residual stress analysis (Noyan & Cohen, 1987, Hauk, 1997) based on traditional grain-interaction models compatible with macroscopic isotropy.

Therefore, in order to evaluate the errors arising from the adoption of a classical grain interaction model, the $\sin^2 \psi$ plots simulated for the current transversely isotropic film have also been tentatively fitted according to the traditional macroscopically isotropic model for the same value of average stress $\sigma_\parallel^S$. In the case of macroscopic isotropy, the common form of equation (3.14) reads (see for instance Noyan & Cohen, 1987, Hauk, 1997, Stickforth, 1966, see also Chapter 2)

$$\left\langle \varepsilon_{33}^L \right\rangle = S_1^{hkl} \left[\left\langle \sigma_{11}^S \right\rangle + \left\langle \sigma_{22}^S \right\rangle \right] + \tfrac{1}{2} S_2^{hkl} \left[\left\langle \sigma_{11}^S \right\rangle \cos^2 \varphi + \left\langle \sigma_{22}^S \right\rangle \sin^2 \varphi \right] \sin^2 \psi \qquad (3.24)$$

where S_1^{hkl} and $\tfrac{1}{2} S_2^{hkl}$ denote the *X-ray elastic constants* (XECs) which arise from the explicit elaboration of equation (3.14) for the macroscopically isotropic body. In view of the rotational symmetry of the film, there is no dependence on φ, thus $\left\langle \sigma_{11}^S \right\rangle = \left\langle \sigma_{22}^S \right\rangle$ and

$$\varepsilon_\psi^{meas} = \left\langle \varepsilon_{33}^L \right\rangle = \left(2 S_1^{hkl} + \tfrac{1}{2} S_2^{hkl} \sin^2 \psi \right) \sigma_\parallel^S = q + m \sin^2 \psi \qquad (3.25)$$

where $\sigma_\parallel^S$, as in equation (3.4), is the average stress in the S system, parallel to the sample surface. As demonstrated by Stickforth (Stickforth, 1966, see also Chapter 2), the two XECs are independent of ψ for a macroscopically isotropic body. Thus, if the XECs are known, the average stress parallel to the surface can be calculated from the slope of the straight line defined by equation (3.25). On the other hand, for a homogeneous specimen and a homogeneous strain/stress field, the absence of such linearity in the $\sin^2 \psi$ plot implies the absence of macroscopic isotropy of the body (see Chapter 2).

To demonstrate the pronounced effects of texture on the diffraction stress analysis, a simple Gaussian fibre texture (Bunge, 1982a), with 5° pole-width (Half-Width at Half-

Maximum, HWHM) was used for two different preferred orientations, namely {110} and {111}. In addition to the calculation of the diffraction strain, the elastic constants A and B where also evaluated as a function of the texture pole width using equations (3.11) and (3.12).

The ODF was supplied numerically for the calculation of A, B and the diffraction strain according to equations (3.11), (3.12) and (3.14). The corresponding section of the pole figure, i.e. the peak area (integrated intensity of the reflection considered) *versus* ψ is also shown in for the diffraction strain calculations. Note that instrumental aberrations and sample effects, as absorption, are not considered. For details on the calculations using the traditional models of Voigt, Reuss and Neerfeld-Hill refer to Appendix 3.2.

Table 3.1: Single crystal elastic constants and anisotropy factor A_i for the elements used in the $\sin^2\psi$ plot simulations. The stiffness matrix components (c_{ij}) and the corresponding compliance matrix components (s_{ij}) are shown. The Voigt 2-index notation (Nye, 1957) is used: to revert to the traditional tensorial notation, the index must be replaced according to: 1=11, 2=22, 4=12 and remembering that $s_{mn} = 4s_{ijkl}$ if m,n>3. The values in bold have been calculated here by tensor inversion.

	c_{11} (GPa)	c_{12} (GPa)	c_{44} (GPa)	s_{11} (TPa^{-1})	s_{12} (TPa^{-1})	s_{44} (TPa^{-1})	A_i	ref.
Au (fcc)	192.9	163.8	41.5	**23.5**	**-10.8**	**24.1**	2.85	Ledbetter & Naimon, 1974
W (fcc)	501	198	151.4	2.57	-0.73	6.6	1.00	Meyers & Chawla, 1984
Nb (bcc)	**244.6**	**138.1**	**29.2**	6.9	-2.49	34.2	0.55	Meyers & Chawla, 1984

3.4. Results and discussion

3.4.1 Tungsten film

Due to the elastic isotropy of tungsten, the response of the film is independent of the particular averaging conducted, i.e. the same trend for the $\sin^2\psi$ curve is expected for all grain interaction models and for all reflections. As long as the specimen and the stress/strain fields are homogeneous (absence of gradients), it is impossible to observe non-linear $\sin^2\psi$ plots for tungsten (cf. discussion below equation (3.25)). Accordingly, the mechanical elastic constants are also independent of the adopted grain-interaction model.
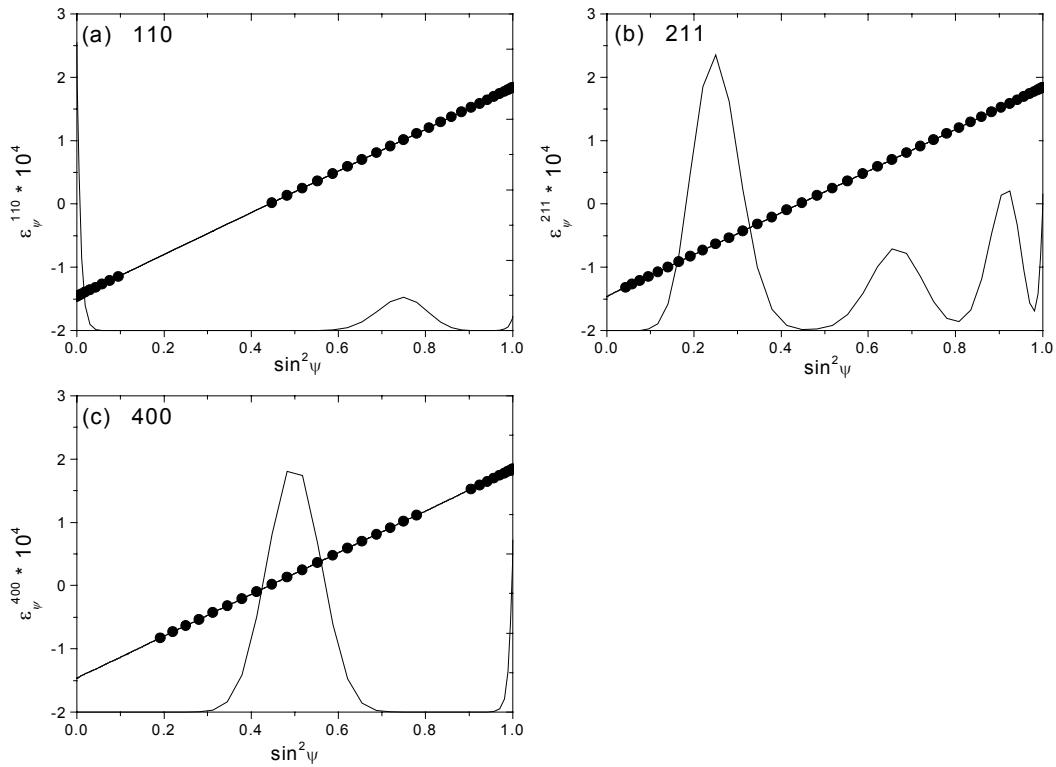

Figure 3.2: Textured, macroscopically isotropic tungsten film (Gaussian {110} fibre texture, 5º half width at half maximum pole width). Lattice strain ε_ψ^{hkl} ($\sin^2\psi$ plots; line with dots) and integrated intensity (lines without dots; arbitrary units) *vs.* $\sin^2\psi$ for the 110 (a), 211 (b) and 400 (c) reflections, respectively. In this case, the ε_ψ^{hkl} curves for all grain-interaction models coincide; in the textured case, only the points that can be calculated (i.e. integrated intensity larger than zero) are shown.

53

Sin$^2\psi$ plots for a {110} textured transversely isotropic tungsten film subjected to a rotationally symmetric stress $\sigma_{\parallel}^{S}$=100MPa are shown in figures 3.2a-c for the 110, 211 and 400 reflections.

The presence of a texture is revealed by the impossibility to record diffracted intensity at all ψ values because of the non-uniform distribution of crystallite orientation. The sections shown of the corresponding pole figure make this clear by presenting the distribution of intensity as a function of ψ.

It should be realised that, due to the texture, the distribution of the intensity as a function of λ (i.e. rotation around the normal of the diffracting *hkl* planes) at constant ψ ($\neq$0º) is strongly varying, in contrast with the corresponding distribution of the strain that does not change with λ for tungsten. As an example, the integrated intensity of the 110 reflection and the corresponding strain for the {110} textured tungsten film at ψ=52º and ψ=88º are shown in figures 3.3a and b, respectively. The evident symmetry of these intensity distributions reflects that of the {110} plane. Corresponding results for the 321 peak at ψ=74º are shown in figure 3c; clearly the {321} plane lacks such symmetry.
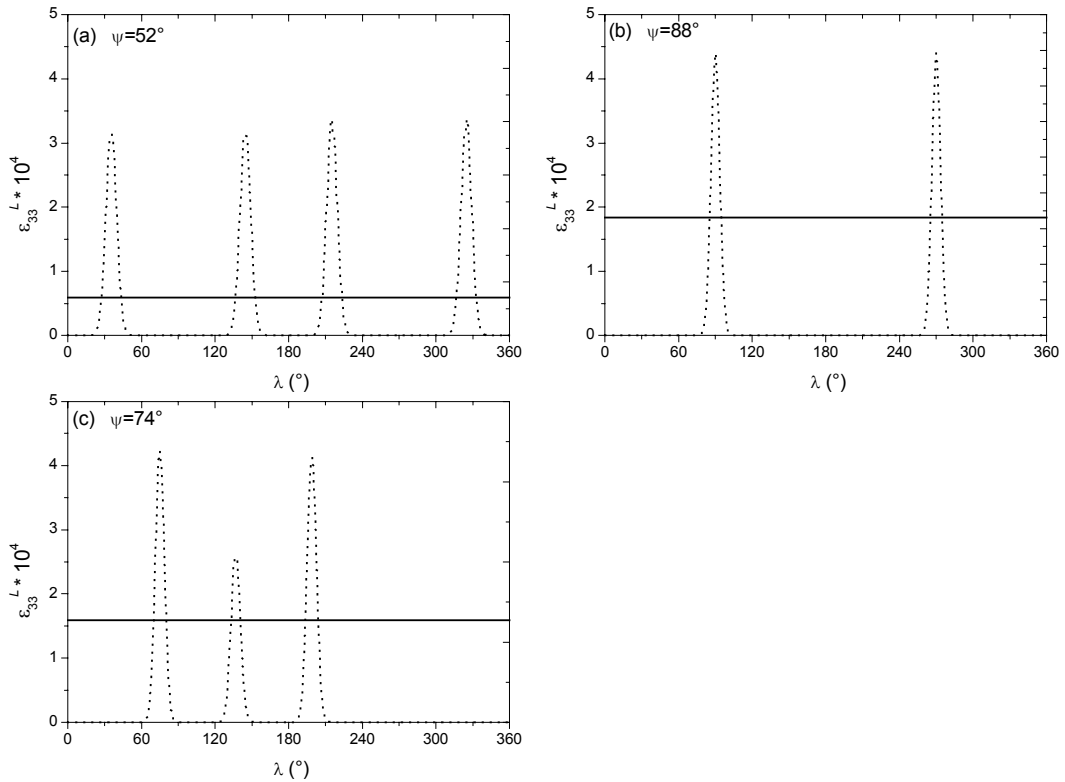
Figure 3.3: Textured, macroscopically isotropic tungsten film (Gaussian {110} fibre texture, 5°
HWHM). Strain ε_{33}^{L} (solid line) and relative integrated intensity (dotted line; arbitrary units) as a
function of the rotation λ around the diffraction vector for the 110 reflection at $\psi=52°$ (a) and
$\psi=88°$ (b), and for the 321 reflection at $\psi=74°$ (c).

3.4.2. Niobium film

Niobium is distinctly anisotropic: $A_i<1$, indicating that the $<hhh>$ direction is 'softer'
than the $<00l>$ one. From the results discussed below, the differences between the values for
the elastic constants as calculated for the various grain-interaction models, in the presence or
absence of texture, might be considered moderate. As will be shown, the consequences of the
intrinsic elastic anisotropy in the diffraction-stress analysis, through the effects of texture and
of the choice of grain-interaction model, are noticeable.

The mechanical elastic constants A and B for {110} and {111} fibre-textured niobium
films are shown in figure 3.4 as a function of the texture pole width. For a cubic material and

a perfect {111} fibre-texture, it is possible to evaluate the elastic constants A and B analytically (Kamminga *et al.,* 2000, Vook and Witt, 1965):

$$A = \frac{2}{3}s_{11}^{C} + \frac{4}{3}s_{12}^{C} + \frac{1}{6}s_{44}^{C} \qquad (3.26)$$

$$B = \frac{2}{3}s_{11}^{C} + \frac{4}{3}s_{12}^{C} - \frac{1}{3}s_{44}^{C} = A - \frac{1}{2}s_{44}^{C} \qquad (3.27)$$

In this case, A and B are independent of the choice of the grain interaction model; the values obtained according to equations (3.26) and (3.27) agree with the numerical results shown in figures 3.4c, and 3.4d. The convergence to a single value for A and B for pole width going to zero, independent of the type of grain-interaction model adopted, is not expected for the {110} texture and is indeed not observed (cf. figures 3.4a-b).
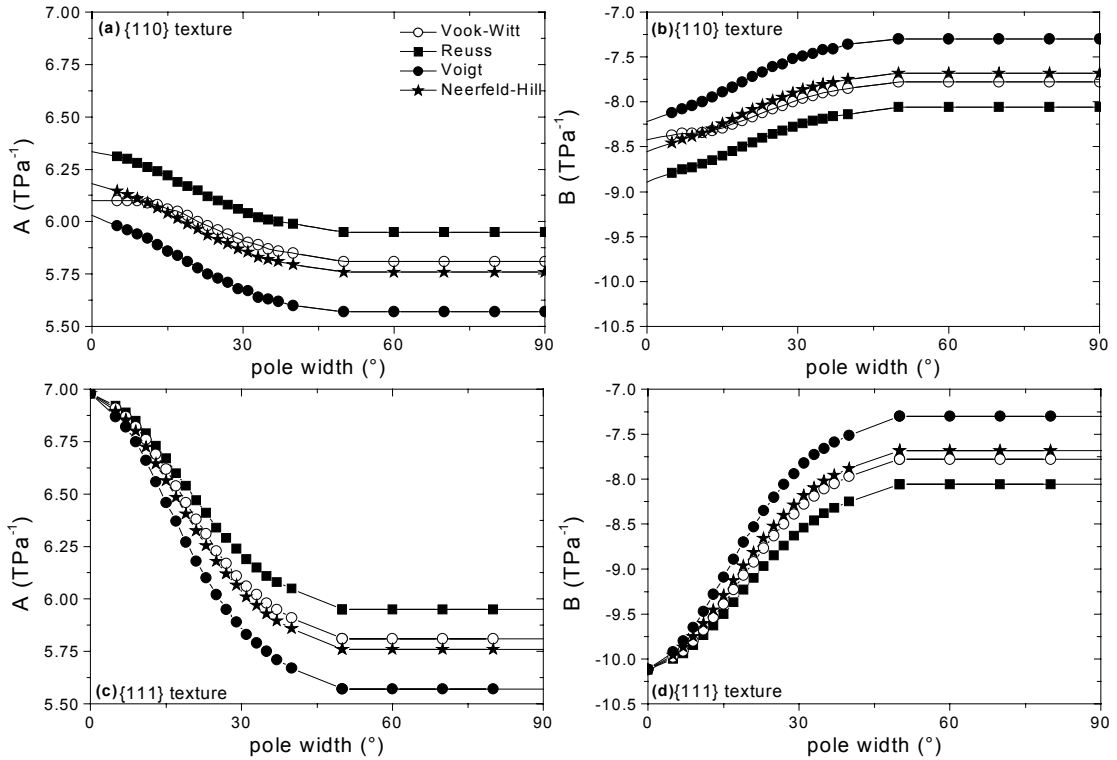

Figure 3.4: Textured, transversely isotropic niobium film. Variation of the macroscopic elastic constants A and B as function of the texture pole width for a Gaussian {110} fibre texture (a and b, respectively) and for a Gaussian {111} fibre texture (c and d, respectively). A legend, valid for all four plots, is presented in (a).

The proof of Hill (1952) that the average elastic constants for a macroscopically mechanically isotropic aggregate should fall within the limits imposed by the Reuss and Voigt models, is in accordance with the numerical results for A and B. However, it should be recognised that the 'effective' X-ray elastic constants need *not* to be within the Voigt and Reuss bounds, as demonstrated by the $\sin^2\psi$ plots for untextured (van Leeuwen *et al.,* 1999) and textured films (this work).

The $\sin^2\psi$ plots for untextured and {110} textured niobium films, containing a stress $\sigma_\parallel^S$ of 100MPa are shown in figure 2.5a for the 211 reflection.

Relatively minor differences occur between the results of the various models, namely Reuss, Voigt and Vook-Witt, in the absence of texture.
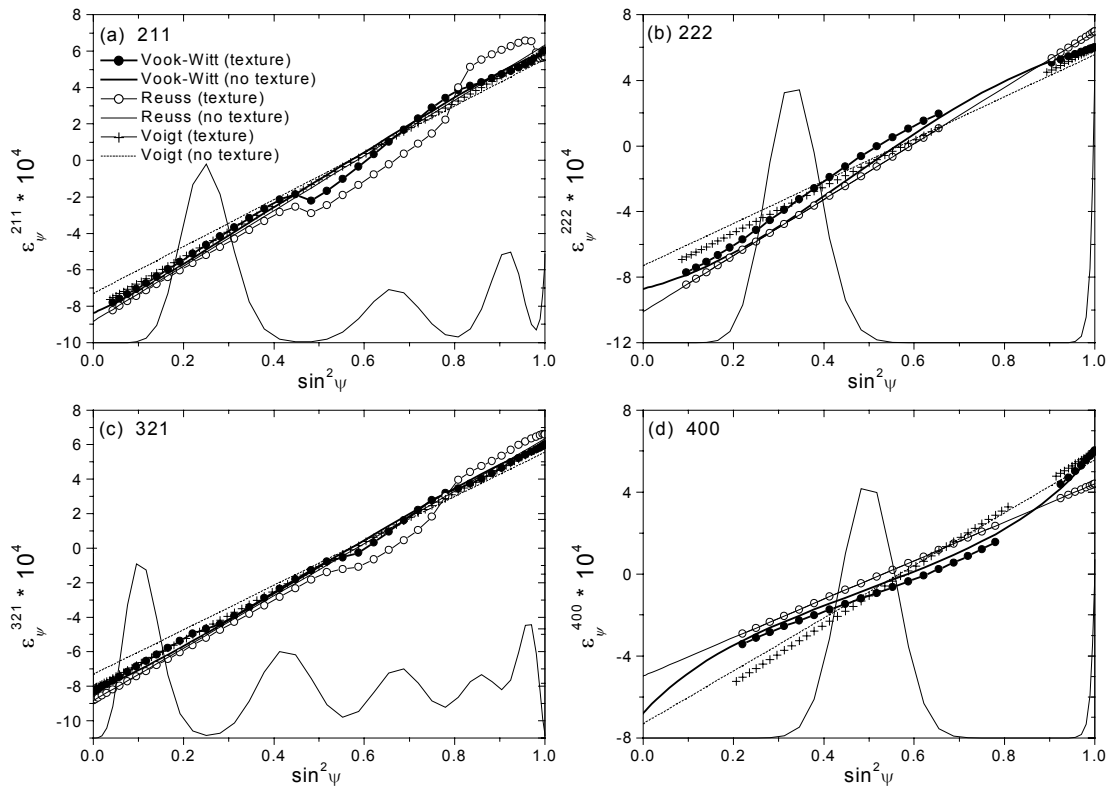

Figure 3.5: Textured, transversely isotropic niobium film (Gaussian {110} fibre texture, 5° HWHM). Lattice strain ε_ψ^{hkl} ($\sin^2\psi$ plots) and integrated intensity (arbitrary units) *vs.* $\sin^2\psi$ for the 211 (a), 222 (b), 321 (c) and 400 (d) reflections, respectively. A legend, valid for all four plots, is presented in (a). The relative integrated intensity is also shown in the figures (lines without dots; arbitrary units).

However, if texture is present, as characterised by three intensity maxima occurring in the plot of integrated intensity *vs.* $\sin^2\psi$, significant differences with the untextured case are observed.

Thus, a clearly non-linear ('discontinuous') dependence of ε_ψ^{hkl} on $\sin^2\psi$ is visible according to the Vook-Witt and Reuss grain-interaction models: the effects in the diffraction stress analysis of the intrinsic (single-crystal) elastic anisotropy of the material are enhanced by the presence of texture.

Similar observations as above can be made considering corresponding results for the 222, 321 and 400 reflections as shown in figures 3.5b-d, respectively. Again, non-linear $\sin^2\psi$ curves occur according to the Vook-Witt grain-interaction model. Note that for the 400 reflection particularly large differences occur between the results of the various grain-interaction models. For the Reuss model it is possible to demonstrate that the $\sin^2\psi$ plot corresponding to the 00*l* and *hhh* reflections is always linear, independent of the texture (see also Brakman, 1983).

An interesting comparison with tungsten is offered by figure 3.6, analogous to figure 3.3. The anisotropy of niobium changes the distribution of strain at constant ψ as a function of λ, in contrast with what is observed for tungsten.

In all the presented $\sin^2\psi$ plots, the strain curve exhibits a change of trend (maxima or minima of the first derivative) at a value of ψ where a minimum occurs in the texture contribution (i.e. diffraction peak area).

Now, to resemble what is normally done in practice, the simulated data according to the Vook-Witt grain-interaction model for the case of a textured film (figure 3.5, full dots) can be reinterpreted in terms of the fully macroscopically isotropic models, i.e. using equation (3.25). Thereby, in principle erroneous values for the stress $\sigma_\parallel^S$ are obtained. To approach closely reality, data points at ψ angles where the integrated intensity is very low (<5% of the maximum value), and data points at high tilting angle, which are affected by large instrumental effects, are not considered. Such 'reduced' plots for the 211, 222, 321 and 400 reflections are shown in figure 3.7.

The straight lines fitted to the data are also shown in figure 3.7 and the resulting $\sigma_\parallel^S$ values are presented in table 3.2. The stress was calculated from the slope of the straight line (cf. equation (3.25)) using the Reuss, Voigt and Neerfeld-Hill models. Considering table 3.2, it follows that very large differences occur in the value of the stress derived: none of the
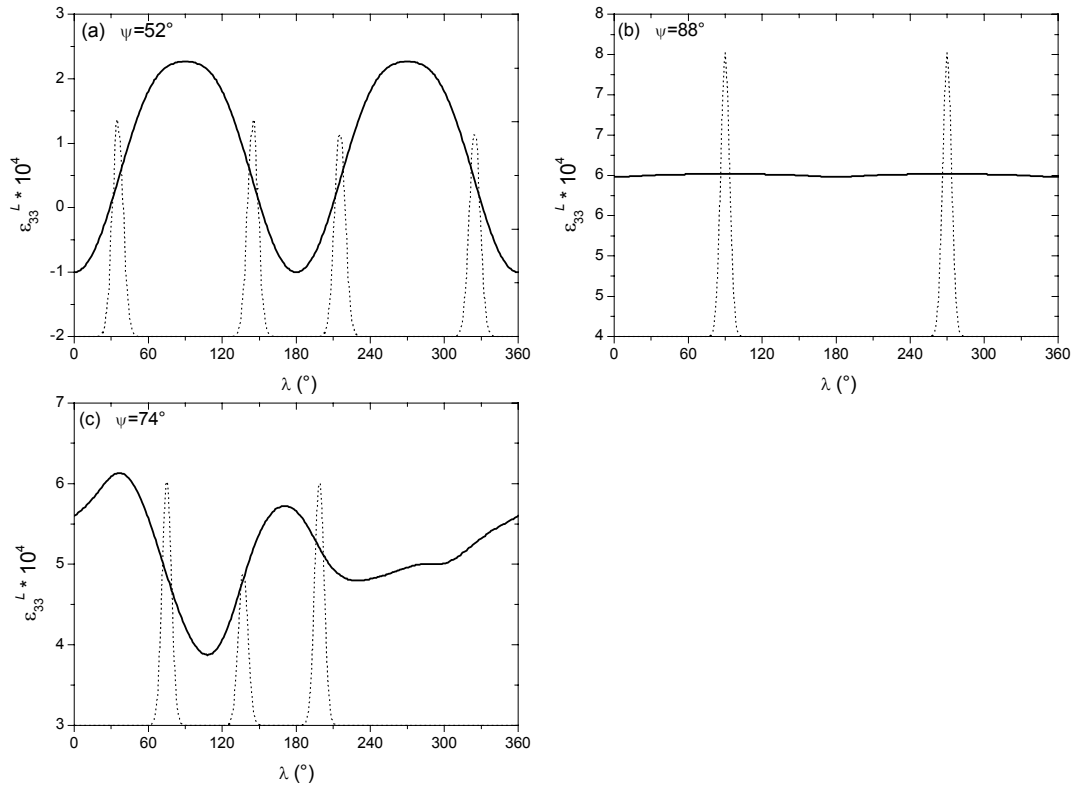
Figure 3.6: Textured, transversely isotropic niobium film (Gaussian {110} fibre texture, 5° HWHM). Strain ε_{33}^L (solid line) and relative integrated intensity (dotted line; arbitrary units) as a function of the rotation λ around the diffraction vector for the 110 reflection at $\psi=52°$ (a) and $\psi=88°$ (b), and for the 321 reflection at $\psi=74°$ (c).

normally used procedures is able to recover the true stress (100MPa) from all the considered reflections (deviations up to 50% occur).

Although the strain data in such plots may apparently be reasonably well fitted with a straight line (equation (3.25)), the results shown in table 3.2 demonstrate that erroneous values for the stress can be obtained.

Commonly, reflections at high Bragg angles are employed in order to minimise errors in the lattice spacing value, due to the uncertainty in peak position determination. The results obtained here show that the application of the normal procedure (equation (3.25)) to the corresponding strain data can lead to quite erroneous results (e.g. see results for the 400 reflection and {110} fibre texture in table 3.2).
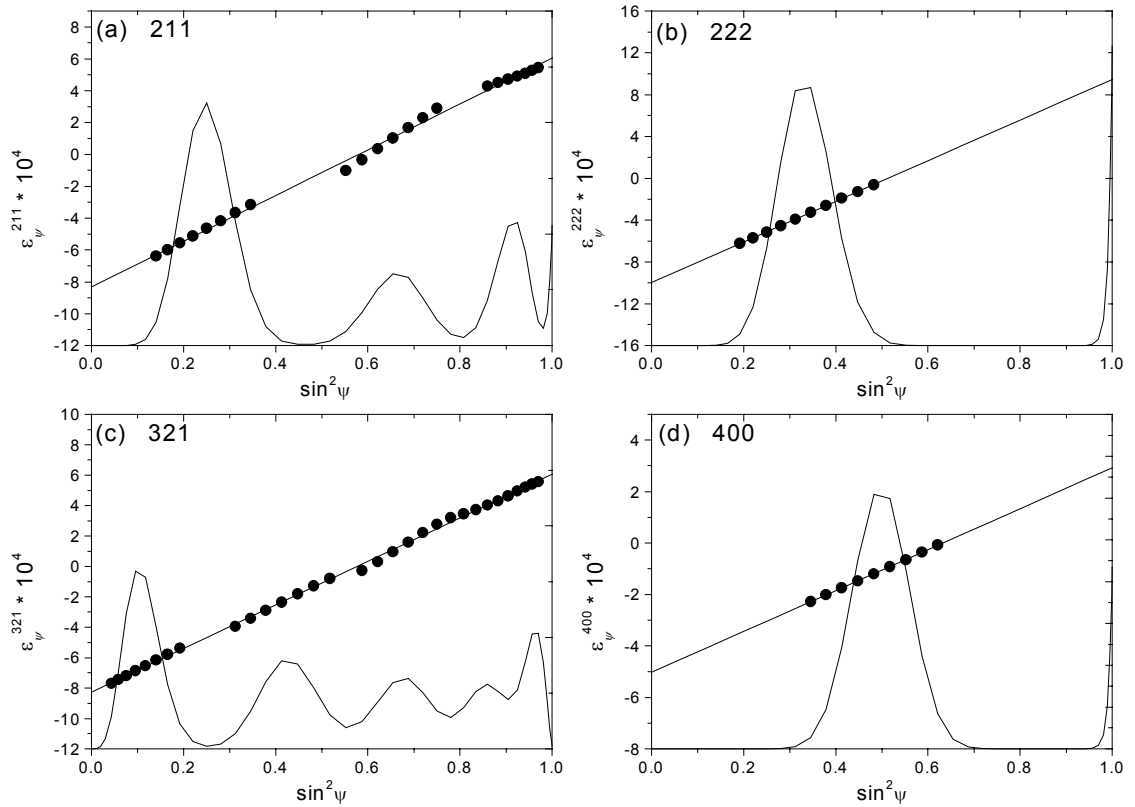
Figure 3.7: Textured, transversely isotropic niobium film (Gaussian {110} fibre texture, 5º HWHM). 'Reduced' $\sin^2\psi$ plots for the 211 (a), 222 (b), 321 (c) and 400 (d) reflections (strain data taken from figures 3.5a-d) as used for the application of the traditional, macroscopically isotropic models: straight line fits according to equation (3.25). The relative integrated intensity is also shown in the figures (lines without dots; arbitrary units).

Table 3.2: Apparent stress values for the niobium film calculated from simulated data by using the macroscopically isotropic models (Voigt, Reuss and Neerfeld-Hill (N-H) respectively). Intercept and slope for the straight line fitted according to equation (3.25) are given together with the correlation coefficient R. The true stress is 100MPa. The fibre texture is indicated by the fibre axis; the orientation distribution around the fibre axis is Gaussian with a 5º HWHM.

reflection hkl	texture	intercept [x10^{-4}]	slope [x10^{-4}]	R	$\frac{1}{2}S_2^{hkl}$ Voigt (TPa^{-1})	$\frac{1}{2}S_2^{hkl}$ Reuss (TPa^{-1})	$\frac{1}{2}S_2^{hkl}$ N-H (TPa^{-1})	$\sigma_\parallel^S$ Voigt (MPa)	$\sigma_\parallel^S$ Reuss (MPa)	$\sigma_\parallel^S$ N-H (MPa)
111	{110}	-9.98	19.4	0.999	14.14	17.10	15.62	137	113	124
112	{110}	-8.32	14.4	0.998	14.14	15.17	14.27	102	95	101
123	{110}	-8.26	14.7	0.999	14.14	15.17	14.42	104	95	102
004	{110}	-5.02	7.95	0.999	14.14	9.39	11.05	56	85	72
111	{111}	-10.2	17.2	0.998	16.89	17.10	17.00	102	101	101
112	{111}	-10.0	17.0	0.997	16.89	15.17	16.03	101	112	106
123	{111}	-9.97	16.9	0.997	16.89	15.17	16.03	100	112	106
004	{111}	-6.22	11.4	0.998	16.89	9.39	13.14	67	121	87

3.4.3. Gold film

The mechanical elastic constants A and B for {110} and {111} fibre-textured gold films are shown in figure 3.8 as a function of the texture pole width. Gold is distinctly anisotropic (A_i>1, indicating that the <00l> direction is 'softer' than the <hhh> one). With reference to the results discussed for the niobium film, it holds also in this case that the consequences of the intrinsic elastic anisotropy through the effects of texture and of choice of the grain-interaction model are most dramatically revealed in the diffraction stress analysis, as shown next.

Gold and niobium possess different crystal structures (bcc and fcc, respectively). As compared to the case of the niobium film, different reflections were thus selected for the study of the gold film, namely the 111, 311, 400 and 331 ones.
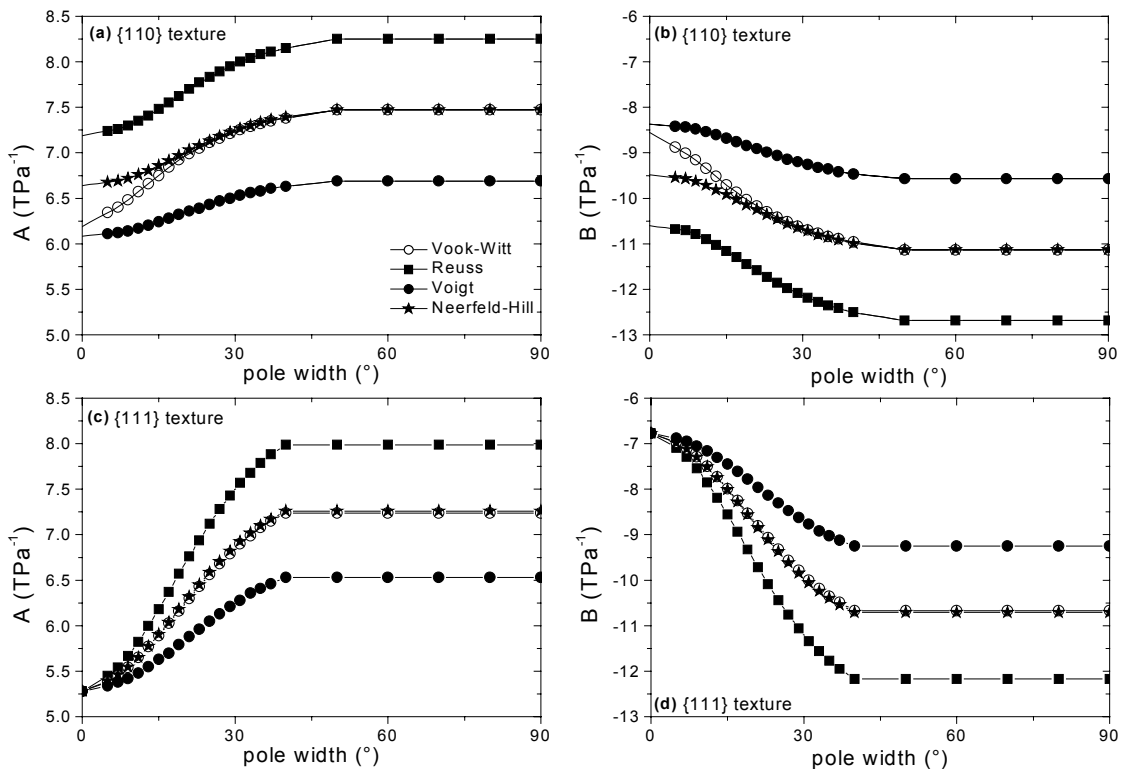

Figure 3.8: Textured, transversely isotropic gold film. Variation of the macroscopic elastic constants A and B as function of the texture pole width for a Gaussian {110} fibre texture (a and b, respectively) and for a Gaussian {111} fibre texture (c and d, respectively). A legend, valid for all four plots, is presented in (a).
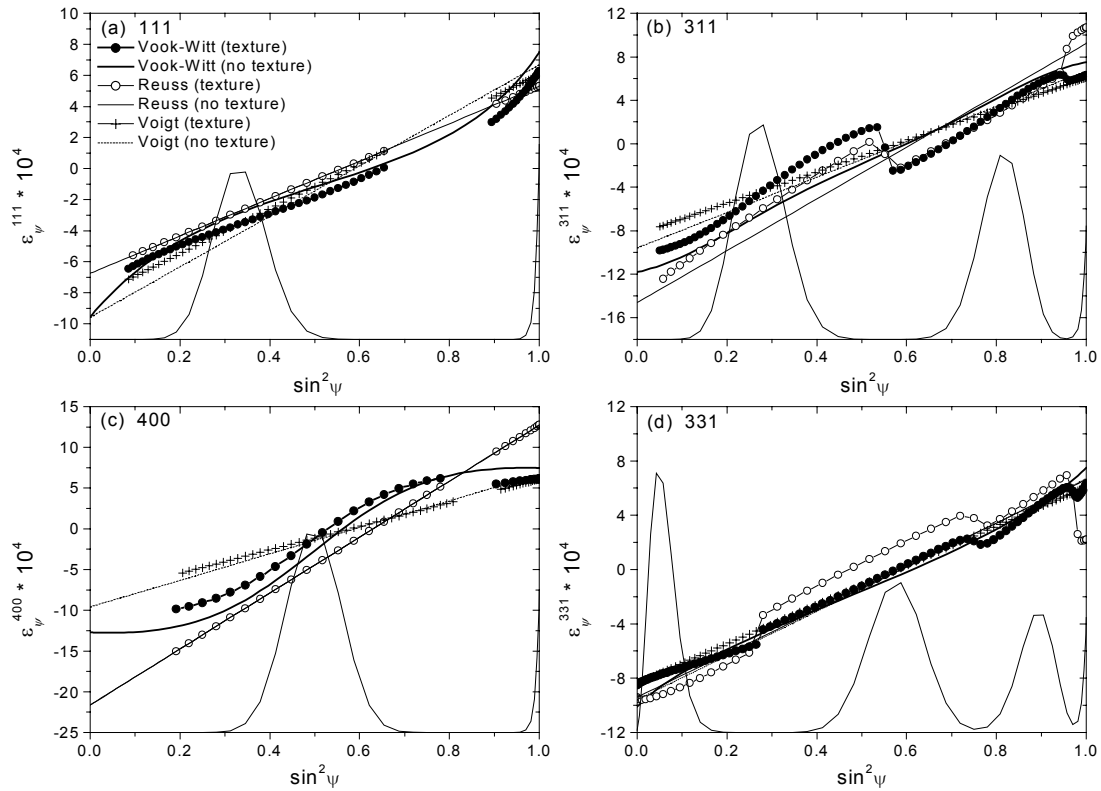
Figure 3.9: Textured, transversely isotropic gold film (Gaussian {110} fibre texture, 5° HWHM). Lattice strain ε_ψ^{hkl} ($\sin^2\psi$ plots) and integrated intensity (arbitrary units) *vs.* $\sin^2\psi$ for the 111 (a), 311 (b), 400 (c) and 331 (d) reflections, respectively. A legend, valid for all four plots, is presented in (a). The relative integrated intensity is also shown in the figures (lines without dots; arbitrary units).

The corresponding $\sin^2\psi$ plots for the untextured and {110} textured gold films containing a stress $\sigma_\parallel^S$ of 100MPa are shown in figures 3.9a-d. The largest differences between the various grain-interaction models are observed for the 111 and 400 reflections where the Reuss model predicts linear $\sin^2\psi$ plots.

For fcc metals as gold, the {111} fibre-texture is more common than the {110} one. The effects of the different texture can be observed by comparing figures 3.9 ({110} fibre texture) and 3.10 ({111} fibre texture). From figure 3.9b and figure 3.10a, the decisive influence of the type of texture on the $\sin^2\psi$ dependence of the strain becomes evident.

As shown for the niobium films, to resemble what is usually done in practice, the simulated data can be interpreted based on traditional analysis involving the incorrect

assumption of macroscopic isotropy. As an example, figure 3.11 shows the 'reduced' (see above for the niobium film) data set for the 331 gold reflection ({110} fibre-texture, see figure 3.9d). A linear dependence of ε_ψ^{hkl} on $\sin^2\psi$ is imposed according to the traditional analyses. Wrong and highly different (from reality) results are obtained by applying the macroscopically isotropic models to obtain a stress value from the simulated data (see table 3.3: note that the true stress is 100MPa).

Table 3.3: Apparent stress values for the gold film calculated from simulated data by using the macroscopically isotropic models (Voigt, Reuss and Neerfeld-Hill (N-H) respectively). Intercept and slope for the straight line fitted according to equation (3.25) are given with the Goodness-of-Fit (R) parameter. The true stress is 100 MPa. The fibre texture is indicated by the fibre axis; the orientation distribution around the fibre axis is Gaussian with a 5º HWHM.

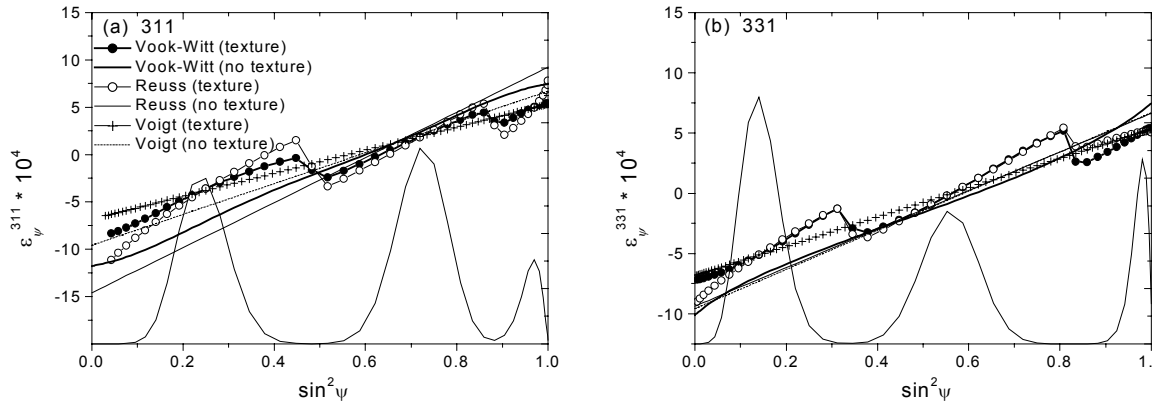| reflection hkl	texture	intercept	slope	R	$\frac{1}{2}S_2^{hkl}$ Voigt	$\frac{1}{2}S_2^{hkl}$ Reuss	$\frac{1}{2}S_2^{hkl}$ N-H	$\sigma_\parallel^S$ Voigt	$\sigma_\parallel^S$ Reuss	$\sigma_\parallel^S$ N-H
		[x10⁻⁴]	[x10⁻⁴]		(TPa⁻¹)	(TPa⁻¹)	(TPa⁻¹)	(MPa)	(MPa)	(MPa)
111	{111}	-6.7	11.7	0.998	12.17	12.05	12.11	96	97	97
113	{111}	-7.3	12.7	0.992	12.17	23.85	18.01	104	53	71
004	{111}	-13.9	22.7	0.998	12.17	34.36	23.27	187	66	98
133	{111}	-6.9	12.1	0.996	12.17	16.01	14.09	99	76	86

Figure 3.10: Textured, transversely isotropic gold film (Gaussian {111} fibre texture, 5º HWHM). Lattice strain ε_ψ^{hkl} ($\sin^2\psi$ plots) and integrated intensity (arbitrary units) *vs.* $\sin^2\psi$ for the 311 (a) and 331 (b) reflections, respectively. A legend, valid for both plots, is presented in (a). The relative integrated intensity is also shown in the figures (lines without dots; arbitrary units).

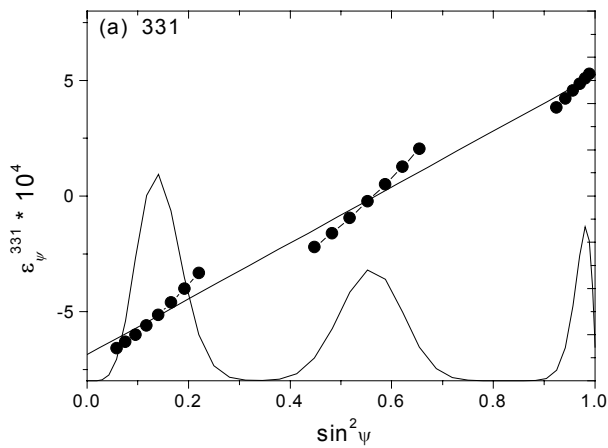*Figure 3.11*. Textured transversely isotropic gold film (Gaussian {111} fibre texture, 5º HWHM). 'Reduced' $\sin^2\psi$ plot for the 331 reflection (strain data taken from figure 3.10b) as used for the application of the traditional, macroscopically isotropic models: straight line fits according to equation (3.25). The relative integrated intensity is also shown in the figure (line without dots; arbitrary units).

3.5. Conclusions

The values of the macroscopic mechanical elastic constants of a polycrystalline body are affected moderately by the type of grain interaction model adopted, irrespective of the presence of texture. Fibre texture (with the fibre axis perpendicular to the specimen surface) in a polycrystalline thin film made of an intrinsically anisotropic material, drastically influences the dependence of lattice strain on measurement direction, i.e. non-linearity occurs in the $\sin^2\psi$ plots. In addition, this kind of texture induces a strong dependence of the lattice strain on the type of grain interaction.

Correct values for the stress components in a textured thin film can be obtained by fitting, to the measured data, the values of strain calculated as a function of the measurement direction by means of equation (3.13) (general) or (3.14) (fibre texture).

The grain interaction in strained polycrystalline thin films is more likely of transversely isotropic character than of macroscopically isotropic nature. The application of the traditional Voigt, Reuss or Neerfeld-Hill models leads to very erroneous values (errors as large as 50%) for the stress derived from classical diffraction analyses (e.g. $\sin^2\psi$ plots) if a Vook-Witt type of grain interaction, compatible with transverse isotropy as in thin films, holds.

Appendix 3.1.

Reference frames

The representation of a tensorial quantity depends on the reference frame. The transformation of a tensor component from one to another orthogonal frame of reference is performed by means of suitable rotations, defined in terms of direction cosines. Consider two orthogonal systems A and B; the cosine of the angle between the unit vector j in the B system and the corresponding unit vector i in the A system, a_{ij}^{AB}, is called *direction cosine*. The direction cosines can be grouped in a *rotation matrix* a^{AB}. Since the rotation preserves norm and angular relations between the reference axes, the rotation matrix is orthonormal and thus its inverse is equivalent to its transposed.

On this basis, the representation in A of a vector v^B represented in B, is given by:

$$v_i^A = a_{ij}^{AB} v_j^B \tag{3A1}$$

Similarly, the inverse transformation is realised by the transposed matrix $\left(a_{ij}^{AB}\right)^{\mathrm{T}}$:

$$v_i^B = a_{ij}^{BA} v_j^A = \left(a_{ij}^{AB}\right)^{\mathrm{T}} v_j^A = a_{ji}^{AB} v_j^A \tag{3A2}$$

It is easy to prove that consecutive transformations are accomplished by consecutive multiplication of the corresponding rotation matrices. Analogous rules are valid for the transformation of higher rank tensors (than pertaining to v^B).

A quick way to evaluate the matrices representing the transformations indicated in this paper, namely a^{LS} and a^{CL} (from which $a^{SC} = (a^{CL} a^{LS})^T$ follows), consists in the decomposition of complex rotations into elementary ones. The transformation from the reference S (sample) to L (laboratory) can be conceived as combination of a rotation φ around S_3 to get an intermediate S' system, followed by a rotation ψ around S'_2 to reach L:

$$a^{LS} = a^{LS'} a^{S'S} = \begin{pmatrix} \cos\psi & 0 & -\sin\psi \\ 0 & 1 & 0 \\ \sin\psi & 0 & \cos\psi \end{pmatrix} \cdot \begin{pmatrix} \cos\varphi & \sin\varphi & 0 \\ -\sin\varphi & \cos\varphi & 0 \\ 0 & 0 & 1 \end{pmatrix} \tag{3A3}$$

These two rotations correspond to the traditional ψ and φ positioning of the specimen in a stress/texture diffractometer.

For the transformation from the laboratory L to the crystal C system, the intermediate reference frame L', fixed with respect to C, is introduced (van Leeuwen *et al.*, 1999). *Cubic* materials (i.e. <hkl>⊥{hkl}) are considered, and L_3 is chosen parallel to the <h,k,l> direction. By setting L'_3 parallel to L_3, the other two orthogonal directions (corresponding to L'_1 and L'_2)

67

can be defined in the plane (h,k,l) as the vectors $(k^2+l^2,-hk,-hl)$ and $(0,-l,k)$; a subsequent rotation around L_3' according to the angle λ, accomplishes the desired a^{CL} transformation

$$a^{CL} = a^{CL'}a^{L'L} = \begin{pmatrix} \dfrac{k^2+l^2}{\sqrt{k^2+l^2}\sqrt{h^2+k^2+l^2}} & 0 & \dfrac{h}{\sqrt{h^2+k^2+l^2}} \\ \dfrac{-hk}{\sqrt{k^2+l^2}\sqrt{h^2+k^2+l^2}} & \dfrac{l}{\sqrt{k^2+l^2}} & \dfrac{k}{\sqrt{h^2+k^2+l^2}} \\ \dfrac{-hl}{\sqrt{k^2+l^2}\sqrt{h^2+k^2+l^2}} & \dfrac{-k}{\sqrt{k^2+l^2}} & \dfrac{l}{\sqrt{h^2+k^2+l^2}} \end{pmatrix} \cdot$$

$$\begin{pmatrix} \cos\lambda & \sin\lambda & 0 \\ -\sin\lambda & \cos\lambda & 0 \\ 0 & 0 & 1 \end{pmatrix}$$

(3A4)

Note the different convention used in this paper with respect to van Leeuwen *et al.*, (1999) concerning the direction for the λ rotation (α rotation in the paper cited). Following equation (A2), the inverse transformation a^{LC} is performed by $(a^{CL})^{-1}=(a^{CL})^T$.

The matrix in equation (A4) is expressed in terms of the Miller indices of the diffraction vector **h**=(h,k,l). The diffraction vector direction can also be expressed in terms of two polar coordinates μ and κ. The following relations between the Miller indices h,k,l and the polar co-ordinates exist ($\kappa=\lambda$ in van Leeuwen *et al.*, 1999)

$h = \sin\mu \sin\kappa$

$k = \sin\mu \cos\kappa$ (3A5)

$l = \cos\mu$

which makes it possible to express a^{CL} and a^{LC} in terms of continuous angles, instead of the integers h,k,l, for an easier integration in Euler space.

Euler space and Euler angles

The orientation of a crystallite with respect to the sample is described by the rotation matrix a^{CS} that transforms the reference frame S of the specimen into the reference frame C associated with the crystal lattice. As follows from the above, the matrix a^{CS} depends on the angles ψ,φ, relating the L and S systems, and on **h** and λ relating the L and C systems. In general, any orientation of the C system with respect to the S system can be represented by three subsequent non-commutative rotations of the S reference frame (Euler angles). The three rotation angles can be conceived as coordinates of a vector in the so-called orientation or Euler space G. A vector $\vec{g}=(\alpha,\beta,\gamma)$ in the Euler space thus represent a possible rotation

matrix a^{CS}.

According to the order of the axes chosen for the rotation, different sets of Euler angles can be defined. In the following, the variant proposed by Roe (Roe & Krigbaum, 1964, Krigbaum & Roe, 1964, Roe, 1965), with the naming convention of Matthies, Vinel & Helming (1987), will be used:

- rotation of S about the axis S_3 through the angle α to get S'; the corresponding vector

  $(\alpha,0,0)$ in Euler space, represents the rotation matrix $\begin{pmatrix} \cos\alpha & \sin\alpha & 0 \\ -\sin\alpha & \cos\alpha & 0 \\ 0 & 0 & 1 \end{pmatrix}$

- rotation of S' about the axis S'_2 through the angle β to get S''; the corresponding vector

  $(0,\beta,0)$ in Euler space, represents the rotation matrix $\begin{pmatrix} \cos\beta & 0 & -\sin\beta \\ 0 & 1 & 0 \\ \sin\beta & 0 & \cos\beta \end{pmatrix}$

- rotation of S'' about the axis S''_3 through the angle γ to get $S''' \equiv C$; the corresponding

  vector $(0,0,\gamma)$ in Euler space, represents the rotation matrix $\begin{pmatrix} \cos\gamma & \sin\gamma & 0 \\ -\sin\gamma & \cos\gamma & 0 \\ 0 & 0 & 1 \end{pmatrix}$

A generic rotation $\vec{g} = (\alpha,\beta,\gamma)$ is thus a combination of the single rotations outlined above:

$$
\begin{aligned}
g = (\alpha,\beta,\gamma) &= (0,0,\gamma)\cdot(0,\beta,0)\cdot(\alpha,0,0) \\
&= \begin{pmatrix} \cos(\gamma) & \sin(\gamma) & 0 \\ -\sin(\gamma) & \cos(\gamma) & 0 \\ 0 & 0 & 1 \end{pmatrix} \cdot \begin{pmatrix} \cos(\beta) & 0 & -\sin(\beta) \\ 0 & 1 & 0 \\ \sin(\beta) & 0 & \cos(\beta) \end{pmatrix} \cdot \begin{pmatrix} \cos(\alpha) & \sin(\alpha) & 0 \\ -\sin(\alpha) & \cos(\alpha) & 0 \\ 0 & 0 & 1 \end{pmatrix}
\end{aligned}
\tag{3A6}
$$

Analogous expressions hold if the convention of Bunge (1982a) is adopted for the definition of the Euler angles.

Appendix 3.2.

Evaluation of A and B: traditional grain interaction models (Voigt, Reuss, Neerfeld-Hill)

The Voigt, Reuss and Neerfeld-Hill models for the calculation of macroscopic elastic properties of polycrystalline solids (Voigt, 1910, Reuss, 1929, Neerfeld, 1942, Hill, 1952) are well known and therefore they will be only briefly discussed. Adopting the Voigt model, the complete *strain* tensor is set equal for all crystallites in the sample reference frame, whereas, adopting the Reuss model, the complete *stress* tensor is set equal for all crystallites in the sample reference frame. In the Voigt case, the stress tensor components are therefore different for the various crystallites:

$$\sigma_{ij}^S = c_{ijkl}^S \varepsilon_{kl}^S \tag{3A7}$$

whereas, in the Reuss case, the strain tensor components are different

$$\varepsilon_{ij}^S = s_{ijkl}^S \sigma_{kl}^S \tag{3A8}$$

as a consequence of the variable crystallite orientation.

In equations (3A7) and (3A8), c^S and s^S represent, respectively, the single-crystal elastic stiffness and compliance tensors transformed to the sample reference frame.

Under these assumptions the macroscopic elastic properties of the polycrystal can be calculated by averaging the compliance tensor in the Reuss-case and by averaging the stiffness tensor in the Voigt-case over all possible crystallite orientations using the ODF as a weighting function (cf. equation (3.10)).

$$\left\langle \sigma_{ij}^S \right\rangle = \left\langle c_{ijkl}^S \varepsilon_{kl}^S \right\rangle = \left\langle c_{ijkl}^S \right\rangle \varepsilon_{kl}^S = c_{ijkl}^{Voigt} \varepsilon_{kl}^S \qquad \text{Voigt model} \tag{3A9}$$

$$\left\langle \varepsilon_{ij}^S \right\rangle = \left\langle s_{ijkl}^S \sigma_{kl}^S \right\rangle = \left\langle s_{ijkl}^S \right\rangle \sigma_{kl}^S = s_{ijkl}^{Reuss} \sigma_{kl}^S \qquad \text{Reuss model} \tag{3A10}$$

The strain tensor can be taken out of the averaging adopting the Voigt model, whereas the stress tensor can be taken out of the averaging adopting the Reuss model, as these tensors are set fixed for all crystallites in equation (3A9) and (3A10), respectively.

The elastic constants A and B describing the elastic behaviour under a rotational symmetric strain field with zero average stress components perpendicular to the film surface (same hypotheses adopted for the Vook-Witt model, see above) can be calculated for the Voigt and Reuss models by imposing the corresponding strain and stress fields.

$$\left\langle \varepsilon^S \right\rangle = \begin{pmatrix} \varepsilon_\parallel & 0 & 0 \\ 0 & \varepsilon_\parallel & 0 \\ 0 & 0 & \varepsilon_\perp \end{pmatrix} = \varepsilon_{Voigt}^S \ , \qquad \left\langle \sigma^S \right\rangle = \begin{pmatrix} \sigma_\parallel & 0 & 0 \\ 0 & \sigma_\parallel & 0 \\ 0 & 0 & 0 \end{pmatrix} = \sigma_{Reuss}^S \tag{3A11}$$

The evaluation of A and B is then a straightforward calculation by substituting the pair of

70

equations (3A9) and (3A10) into equations (3.6) and (3.7). The Voigt and Reuss models predict macroscopically isotropic properties in the absence of texture and transversely isotropic properties for fibre textured specimens.

The two models cannot represent the true elastic behaviour of a polycrystalline aggregate (apart for a body composed of a truly intrinsically elastically isotropic material), due to the extreme nature of the grain interaction assumptions. The Voigt model, for example, violates mechanical equilibrium, as the stress is discontinuous at crystallite boundaries. Further, the macroscopic elastic constants derived from both models are incompatible (Matthies & Humbert, 1995), i.e. $c^{Voigt} \neq (s^{Reuss})^{-1}$.

Hill proved that the Reuss and Voigt models represent, respectively, the lower and upper bounds for the elastic moduli of a macroscopically isotropic aggregate (Hill, 1952). Therefore, it is reasonable to assume that the true average elastic constants are better approximated by the arithmetic average of the values predicted by the Reuss and Voigt models. This approach is generally referred to as the Neerfeld-Hill model (Neerfeld, 1942, Hill, 1952). The Neerfeld-Hill approach is just an averaging procedure and does not represent a specific grain-interaction model in the sense that specific grain-interaction parameters can be indicated. This holds also for alternative models, which do obey the compatibility relation $c = s^{-1}$ (like that based on the geometric averaging of the elastic tensors; Matthies & Humbert,1995).

72

4. The determination of stresses in thin films; modelling elastic grain interaction

U. Welzel, M. Leoni & E. J. Mittemeijer

Abstract

X-ray diffraction is frequently employed for the analysis of mechanical stresses in polycrystalline specimens. To this end, suitable so-called diffraction elastic constants are needed for determining the components of the mechanical stress tensor from measured lattice strains. These diffraction elastic constants depend on the single crystal elastic constants of the material considered and the so-called grain interaction, describing the distribution of stresses and strains over the crystallographically differently oriented crystallites composing the specimen. Well-known grain-interaction models, as due to Voigt, Reuss, Neerfeld-Hill and Eshelby-Kröner, may be applied to bulk specimens, but they are generally not suitable for thin films. In this paper, an average, 'effective' grain-interaction model is proposed that consists of a linear combination of basic, extreme models including new models specially suited for thin films. Experimental verification has been achieved by X-ray diffraction strain measurements performed on a sputter-deposited copper film. This is the first time that anisotropic grain interaction has been analysed quantitatively.

4.1. Introduction

X-ray residual stress analysis is routinely employed for the determination of homogeneous macrostress states in polycrystalline solids (see, for example, Noyan & Cohen, 1987, Hauk, 1997). Generally, diffraction lines of one or more *hkl* reflections are recorded at various sample tilt (and possibly, dependent on the complexity of the stress state, rotation) angles. From the measured peak positions lattice strains can be calculated.

A straightforward interpretation of strains in terms of stresses can be obstructed if the single crystallites composing the specimen are elastically anisotropic. In this case neither the mechanical elastic constants (relating mechanical (macroscopic) strains to mechanical (macroscopic) stresses) nor the diffraction elastic constants (diffraction stress factors for elastically anisotropic samples), relating (diffraction) lattice strains to mechanical stresses, can be derived without more ado from single-crystal elastic compliances (or stiffnesses) of the crystallites composing the specimen. A so-called grain-interaction model is needed to describe the distribution of stresses and strains over the crystallographically differently oriented crystallites in the specimen.

Common grain-interaction models are the Voigt (1910), Reuss (1929) and Eshelby-Kröner (Eshelby, 1957, Kröner, 1958, see also Kneer, 1965) models, which were devised for the calculation of mechanical elastic constants of bulk polycrystals from single-crystal elastic compliances. Such models can also be used for the calculation of X-ray elastic constants from single-crystal elastic compliances. The models according to Voigt and Reuss present extremes for the grain interaction: either the strain tensor (Voigt model) or the stress tensor (Reuss model) for each crystallite is assumed to be equal to the mechanical strain or stress tensor, respectively; they are incompatible with physical reality because of the corresponding stress, respectively strain discontinuities at the grain boundaries. It was shown that the Voigt and Reuss models set bounds for the mechanical elastic constants (Hill, 1952). Further, Neerfeld (1942) and Hill (1952), on an empirical basis, suggested that the arithmetic (or geometric[2]) averages of X-ray (Neerfeld, 1942) and macroscopic (Neerfeld, 1942, Hill, 1952) elastic constants calculated according to the models of Voigt and Reuss yield values that come close to experimental values. The mathematically more tedious Eshelby-Kröner model gives numerical values close to those obtained by this Neerfeld-Hill approach.

---

[2] Usually the arithmetic and not the geometric average is used.

The above models have been devised for bulk materials. Yet, these models are also frequently applied to thin film stress analysis. Owing to their microstructure and reduced dimensionality, the elasticity of thin films can be different from the elasticity of bulk polycrystals. Thin films cannot generally be considered as macroscopically elastically isotropic, rather they can exhibit macroscopically transversely isotropic properties (even in the absence of texture; van Leeuwen *et al.*, 1999). The traditional models for grain interaction (Voigt, Reuss, Eshelby-Kröner, Neerfeld-Hill) are compatible only with macroscopically isotropic elastic properties (in the absence of texture) and hence these models are inappropriate for the analysis of stress in such thin films.

Only recently it has been demonstrated experimentally by van Leeuwen *et al.* (1999) for an untextured Ni film that diffraction effects can be observed (curved $\sin^2\psi$-plots; see further) that are incompatible with the traditional models for grain interaction. Van Leeuwen *et al.* (1999) demonstrated that a grain-interaction model, which is adapted to the microstructure of a columnar thin film, can explain these experimental findings. To this end, grain-interaction assumptions proposed by Vook and Witt (Vook & Witt, 1965, Witt & Vook, 1968) were, for the first time, employed for the analysis of diffraction stress measurements. Leoni *et al.* (2001) extended this Vook-Witt based model to fibre-textured specimens and showed by simulations that erroneous results (errors as large as 50%) for the stress can easily occur when this type of grain interaction holds and, yet, traditional models are employed in stress analysis.

The Vook-Witt based grain-interaction model is the first model taking the microstructure of a (columnar) thin film into account by assuming that all crystallites exhibit the same in-plane strain whereas they can deform freely in a direction perpendicular to the film surface as a consequence of the columnar grain structure, implying a predominant orientation of the grain boundaries perpendicular to the film surface. A grain-interaction model involving different grain interaction assumptions for different directions in the specimen will be called a direction-dependent grain interaction model in the following.

Although the Vook-Witt approach can be considered as some 'intermediate' model of grain interaction (with reference to the Voigt and Reuss models), it still imposes extreme constraints: identical in-plain strain and completely unconstrained deformation perpendicular to the surface, for all grains. Extreme grain-interaction assumptions are in general not compatible with the true elastic behaviour of real polycrystals. Therefore, in this paper a more general approach to grain interaction (in thin films) is presented. The method proposed is applied to the diffraction analysis of stress in a fibre-textured copper layer.

4.2. Theory

4.2.1. Calculation of mechanical and diffraction averages of elastic stress and strain tensors by adopting a grain-interaction model

For the considerations presented in the following it is convenient to make use of three Cartesian frames of reference:

- The *crystal reference frame* (C): the conventional definition of an orthonormal crystal system, such as the one given by Nye (1957) (for a detailed treatment, see also Giacovazzo *et al.*, 1998) is adopted. Thus, for cubic crystal symmetry, the axes are chosen parallel to the *a*, *b* and *c* axis of the crystal lattice.

- The *specimen reference frame* (S): The S_3-axis is oriented perpendicular to the specimen surface and the S_1- and S_2-axes are in the surface plane.

- The *laboratory reference frame* (L): This frame is chosen in such a way that the L_3-axis coincides with the diffraction vector in the (X-ray) diffraction experiment.

In the following a superscript (C, S or L) indicates the reference frame used for the representation of tensors. The absence of any superscript implies the validity of an equation independent of the reference frame used for tensor representation (but the same reference frame has to be adopted for all tensors in the equation). For the relative orientations of laboratory and the specimen frames of reference, consider also figure 4.1.

Transformations of tensors can be accomplished by suitable rotation matrices (for a general introduction on the use of transformation matrices in the context of X-ray diffraction, see for example, Hauk (1997), for detailed information on matrices within the context of this Chapter, see also Chapter 3.2.1 and the corresponding Appendix).

The orientation of each crystallite in the S system can be identified by three Euler angles. The convention of Roe and Krigbaum (1964) in the definition of these angles will be adopted and the angles will be called α, β and γ. It is usual to associate a set of Euler angles to a vector $\vec{g} = (\alpha, \beta, \gamma)$ in the three-dimensional orientation (Euler) space G (for example, see Bunge, 1982a). In this way, each point in the orientation space G represents a possible orientation of the C system with respect to the S system. Only in the absence of texture it holds, that the volume fraction of crystallites having an orientation in the infinitesimal orientation range $d^3g = \sin(\beta)d\alpha d\beta d\gamma$ around $\vec{g}$ is independent of $\vec{g}$.
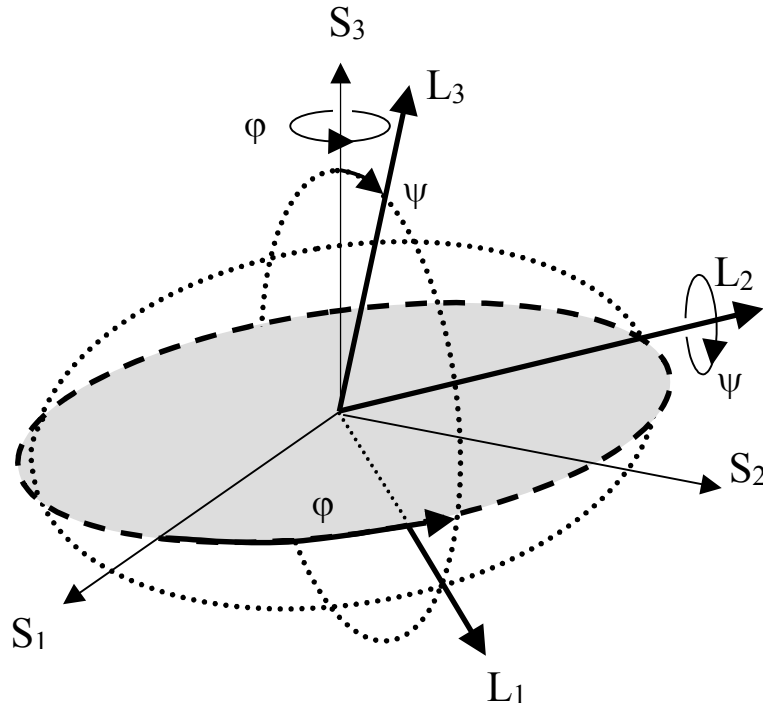
Figure 4.1: Definition of and relations between the sample (*S*) and laboratory (*L*) reference frames.

The occurrence of texture implies the introduction of the so-called orientation distribution function (ODF) $f(\alpha,\beta,\gamma)$, which is a function of the Euler angles, specifying the volume fraction of crystallites having an orientation in the infinitesimal orientation range $d^3g = \sin(\beta)d\alpha d\beta d\gamma$ around $\vec{g}$:

$$\frac{dV(\vec{g})}{V} = \frac{f(\vec{g})}{8\pi^2}d^3g = \frac{f(\alpha,\beta,\gamma)}{8\pi^2}\sin(\beta)d\alpha d\beta d\gamma .\qquad (4.1)$$

The ODF is normalised such that it holds:

$$\iiint_G \frac{f(\vec{g})}{8\pi^2}d^3g = 1 .\qquad (4.2)$$

On the basis of the Euler angles it is possible to calculate mechanical and diffraction averages of elastic-, stress- and strain tensors. In the following, angular brackets $\langle\ \rangle$ denote volume-weighed averages for all crystallites in the aggregate considered (i.e. mechanical averages) whereas braces $\{\ \}$ denote volume-weighed averages for diffracting crystallites only (i.e.

diffraction averages). The group of diffracting crystallites is selected by specifying the reflection *hkl* under consideration and the orientation of the diffraction vector with respect to the specimen reference frame, which will be specified by the angles (ψ,φ), where ψ is the inclination of the diffraction vector with respect to the surface normal of the sample and φ is the rotation angle around the sample surface normal (see also figure 4.1).

Mechanical averages of a tensor Ω, e.g. the strain tensor ε, can be calculated by integration over all Euler angles, using the ODF as a weighting factor:

$$\langle\Omega\rangle = \frac{1}{8\pi^2}\iiint_G \Omega\ f\left(\vec{g}\right) d^3g =$$
$$= \frac{1}{8\pi^2}\int_{\gamma=0}^{2\pi}\int_{\beta=0}^{\pi}\int_{\alpha=0}^{2\pi}\Omega(\alpha,\beta,\gamma)\ f(\alpha,\beta,\gamma)\ \sin(\beta)d\alpha d\beta d\gamma \qquad (4.3)$$

For the corresponding diffraction averages only the diffracting crystallites have to be taken into account. As the orientation of the diffracting crystallites differs only by a rotation around the diffraction vector, the averaging has to be performed with respect to this degree of freedom, in the following called λ (see Chapter 3.2.1):

$$\{\Omega\}_{\varphi,\psi}^{hkl} = \frac{\int_0^{2\pi}\Omega(hkl,\lambda,\varphi,\psi)\ f^*(hkl,\lambda,\varphi,\psi)d\lambda}{\int_0^{2\pi}f^*(hkl,\lambda,\varphi,\psi)d\lambda} \ . \qquad (4.4)$$

$f^*(hkl,\lambda,\varphi,\psi)$ is the representation of the ODF in terms of the measurement parameters and the rotation angle with respect to the diffraction vector. The ODF as defined in equation (4.1) cannot be directly used in equation (4.4) in analogy to equation (4.3) since the angles λ,φ,ψ are *not* Euler angles representing a rotation of the *C* system with respect to the *S* system (they provide the rotation of the system *L* with respect to the system *S*). However, the values of α, β, γ and thus $f(\alpha,\beta,\gamma)$ at every λ can be calculated from *hkl*, λ, φ and ψ, to be finally substituted for $f^*(hkl,\lambda,\varphi,\psi)$ in equation (4.4) (for a more detailed treatment of the necessary calculations, see Chapter 3.2.1). Thus, the diffraction strain measured for a particular reflection *hkl* at the orientation of the diffraction vector (φ,ψ) can be calculated according to:

$$\varepsilon_{\varphi,\psi}^{hkl} = \{\varepsilon_{33}^L\}_{\varphi,\psi}^{hkl} = \frac{\int_0^{2\pi}\varepsilon_{33}^L(hkl,\lambda,\varphi,\psi)f^*(hkl,\lambda,\varphi,\psi)d\lambda}{\int_0^{2\pi}f^*(hkl,\lambda,\varphi,\psi)d\lambda} \ . \qquad (4.5)$$

The analysis will be focused on an at least transversely isotropic thin film subjected to a plane, rotationally symmetric state of stress. This requires that the film is either untextured or fibre-textured (fibre texture is frequently encountered in thin films grown on (amorphous) substrates by physical or chemical vapour deposition). Thus, both the symmetry axis of the elastic properties and the symmetry axis of the stress field are parallel to the specimen normal.

The rotational symmetric, plane state of stress is characterised by the following stress tensor:

$$\langle\sigma^S\rangle = \begin{pmatrix} \sigma_{\parallel}^S & 0 & 0 \\ 0 & \sigma_{\parallel}^S & 0 \\ 0 & 0 & 0 \end{pmatrix}. \tag{4.6}$$

Owing to the transverse isotropy, the stress field induces a rotational symmetric strain field:

$$\langle\varepsilon^S\rangle = \begin{pmatrix} \varepsilon_{\parallel}^S & 0 & 0 \\ 0 & \varepsilon_{\parallel}^S & 0 \\ 0 & 0 & \varepsilon_{\perp}^S \end{pmatrix}. \tag{4.7}$$

Only two elastic constants are required to describe fully the relation between the stress and strain tensors for a transversely isotropic body subjected to a plane state of stress, as only two strain tensor components and one stress tensor component are independent and non-zero. In analogy to van Leeuwen *et al.* (1999) (see also Chapter 3. in this work), those elastic constants will be called A and B:

$$\varepsilon_{\parallel}^S = A\sigma_{\parallel}^S, \tag{4.8}$$

$$\varepsilon_{\perp}^S = B\sigma_{\parallel}^S. \tag{4.9}$$

For the calculation of the stress $\sigma_{\parallel}^S$ from lattice strains measured by X-ray diffraction (cf. equation (4.5)), the $\sin^2\psi$-method is employed traditionally: the peak position of a particular *hkl* reflection is measured at different specimen tilt angles ψ and the lattice strain perpendicular to the *hkl* planes at the different tilt angles ψ is calculated from the measured peak positions. For a macroscopically isotropic specimen the following equation relates the lattice strain to the components of the mechanical stress tensor (see, for example, Hauk, 1997, see also Chapter 2):

$$\varepsilon_{\varphi,\psi}^{hkl} = \tfrac{1}{2} S_2^{hkl} \sin^2 \psi \left(\langle \sigma_{11}^S \rangle \cos^2 \varphi + \langle \sigma_{12}^S \rangle \sin(2\varphi) + \langle \sigma_{22}^S \rangle \sin^2 \varphi \right) +$$
$$+ \tfrac{1}{2} S_2^{hkl} \left(\langle \sigma_{13}^S \rangle \cos \varphi \sin(2\psi) + \langle \sigma_{23}^S \rangle \sin \varphi \sin(2\psi) + \langle \sigma_{33}^S \rangle \cos^2 \psi \right) \quad (4.10)$$
$$+ S_1^{hkl} \left(\langle \sigma_{11}^S \rangle + \langle \sigma_{22}^S \rangle + \langle \sigma_{33}^S \rangle \right)$$

For the case of a plane, rotationally symmetric state of mechanical stress ($\langle \sigma_{12}^S \rangle = \langle \sigma_{13}^S \rangle = \langle \sigma_{23}^S \rangle = \langle \sigma_{33}^S \rangle = 0$), $\varepsilon_{\varphi,\psi}^{hkl}$ is independent of φ and equation (4.10) can be simplified:

$$\varepsilon_{\psi}^{hkl} = \left(2 S_1^{hkl} + \tfrac{1}{2} S_2^{hkl} \sin^2 \psi \right) \sigma_{\parallel}^S . \qquad (4.11)$$

The stress $\sigma_{\parallel}^S$ can be deduced from the slope of a plot of the diffraction strain versus $\sin^2 \psi$. The constants S_1^{hkl} and $\tfrac{1}{2} S_2^{hkl}$ are independent of ψ and φ and are called X-ray elastic constants. These constants were introduced on an empirical basis by Möller & Martin (1939).

Decades later Stickforth (1966) has proved on the basis of symmetry considerations that the concept of X-ray elastic constants is justified for any macroscopically elastically isotropic aggregate, i.e. thereby confirming the validity of equation (4.11) in such a case (see also Chapter 2 in this work; note that the analysis of shear components of the stress tensor was discussed explicitly by Evenschor & Hauk (1975) for the first time).

Preferred crystallographic orientation (crystallographic texture) leads to macroscopically anisotropic elastic properties for a polycrystalline aggregate, if intrinsic (single crystal) elastic anisotropy occurs. This is the only case of macroscopic elastic anisotropy considered traditionally. Within this context the X-ray stress factors have been introduced (Dölle & Hauk, 1978, Dölle & Hauk, 1979). The φ, ψ and *hkl*-dependent X-ray stress factors relate the diffraction strain to mechanical stress expressed in the *S*-system (the Einstein convention, i.e. summation over indices appearing at least twice in a formula, is adopted):

$$\varepsilon_{\varphi,\psi}^{hkl} = F_{kl}(\psi, \varphi, hkl) \langle \sigma_{kl}^S \rangle . \qquad (4.12)$$

Note that the $F_{kl}(\psi, \varphi, hkl)$ are not components of a tensor since they relate the lattice strain (a number) to the stress tensor (expressed in the *S*-system).

For the case of a plane, rotationally symmetric state of stress equation (4.12) can be simplified.

$$\varepsilon_{\varphi,\psi}^{hkl} = \left(F_{11}(\psi, \varphi, hkl) + F_{22}(\psi, \varphi, hkl) \right) \sigma_{\parallel}^S . \qquad (4.13)$$

For the case of transverse elastic isotropy, the diffraction strain is independent of the angle φ, thus, φ can be set to zero (or any other value) for the X-ray stress factors and φ as an index can be suppressed for the diffraction strain:

$$\varepsilon_\psi^{hkl} = \left(F_{11}(\psi, 0, hkl) + F_{22}(\psi, 0, hkl) \right) \sigma_\parallel^S \tag{4.14}$$

Only recently, it has been demonstrated both theoretically and experimentally by van Leeuwen *et al.* (1999) that direction-dependent grain interaction leads to macroscopically anisotropic elastic behaviour, even in the absence of texture. Also in this case, an analysis on the basis of equation (4.11) is not possible, but equation (4.12) can be employed (this has been shown for the first time in Chapter 2).

The X-ray stress factors can, like the X-ray elastic constants, be calculated by adopting a grain-interaction model. In the following, a model for the calculation of macroscopic and X-ray (diffraction) elastic constants will be called a grain-interaction model, when it enables the calculation of the strain tensor $\varepsilon(\alpha, \beta, \gamma)$ and the stress tensor $\sigma(\alpha, \beta, \gamma)$ for every crystallite in the aggregate considered from the average stress $\langle \sigma^S \rangle$ and/or strain $\langle \varepsilon^S \rangle$. The basics common to all grain-interaction models considered here are as follows:

For each crystallite, the stress and strain tensors in the specimen reference frame satisfy Hooks law:

$$\varepsilon_{ij}^S = s_{ijkl}^S \sigma_{kl}^S . \tag{4.15}$$

The s_{ijkl}^S denote the single crystal elastic compliances expressed in the specimen frame of reference. Equation (4.15) represents a system of nine equations for eighteen unknowns, but as the strain and stress tensors are symmetric (i.e. $\varepsilon_{ij} = \varepsilon_{ji}$ and $\sigma_{ij} = \sigma_{ji}$), equation (4.15) thus is a short notation for six independent equations for twelve independent unknowns. If six components of the twelve unknowns are known, as a consequence, the other components can be calculated by solving the system of equations (4.15). In the type of grain-interaction models considered here, a total of six stress and/or strain tensor components in the S system are taken equal to the mechanical averages for all crystallites and thus the other six (unknown) components can be calculated from the system of equations (4.15).

The elastic constants A and B can thus be calculated from (cf. equations (4.8) and (4.9)):

$$A = \frac{\varepsilon_\parallel^S}{\sigma_\parallel^S} = \frac{\langle \varepsilon_{11}^S \rangle}{\langle \sigma_{11}^S \rangle} = \frac{\iiint\limits_G \varepsilon_{11}^S f(\vec{g}) d^3 g}{\iiint\limits_G \sigma_{11}^S f(\vec{g}) d^3 g} \tag{4.16}$$

and

$$B = \frac{\varepsilon_\perp^S}{\sigma_\parallel^S} = \frac{\left\langle \varepsilon_{33}^S \right\rangle}{\left\langle \sigma_{11}^S \right\rangle} = \frac{\iiint\limits_G \varepsilon_{33}^S f(\vec{g}) d^3 g}{\iiint\limits_G \sigma_{11}^S f(\vec{g}) d^3 g} .$$

(4.17)

The diffraction strain can be calculated following equation (4.5) and the stress factors follow from equation (4.14):

$$\left(F_{11}(\psi, 0, hkl) + F_{22}(\psi, 0, hkl) \right) = \frac{\varepsilon_\psi}{\sigma_\parallel^S} .$$

(4.18)

However, only the sum of the two X-ray stress factors is needed. This sum will be abbreviated as:

$$F(\psi, hkl) \stackrel{def}{=} F_{11}(\psi, 0, hkl) + F_{22}(\psi, 0, hkl)$$

(4.19)

4.2.2. 'Average grain interaction'

Neerfeld (1942) and Hill (1952) found on an empirical basis, that the arithmetic (or geometric[1]) averages of (X-ray and macroscopic) elastic constants calculated according to the models of Voigt and Reuss yield values that come close to the true, i.e. experimental ones. This 'average' Neerfeld-Hill (NH) model is, strictly speaking, not a grain-interaction model, as it is not possible to specify the grain-interaction assumptions for each individual grain composing a polycrystalline aggregate.

In a similar way, X-ray stress factors can be calculated as the arithmetic average of the stress factors calculated according to the Reuss (R) and Voigt (V) models (see, for example, Brakman, 1988, Serruys *et al.*, 1987). A generally accepted physical basis for mixing the models of Reuss and Voigt lacks, but a few authors have tried to give a physical basis of such a averaging procedure (Serruys *et al.*, 1987, Serruys *et al.*, 1989). The background of any averaging of (extreme) grain- interaction models to represent physical reality could be described as follows. A real sample is conceived to be constituted from separate volume fractions of crystallites, each of which obeys a certain type of grain interaction. For the following discussion an average of (extreme) grain-interaction models will be called an effective grain-interaction model. It will be shown that, depending on the type of specimen considered, appropriate choices of the grain- interaction models 'to be averaged' can be made.

For an at least transversely isotropic body in a plane, rotationally symmetric state of stress, two mechanical constants, A and B, suffice for describing the macroscopic elastic behaviour (cf. equations (4.8) and (4.9)). If it is assumed that the volume fraction f_i of the

polycrystalline aggregate obeys the (extreme) grain-interaction model i (in Chapter 4.3.2 four grain-interaction models will be considered), the average macroscopic strain of the aggregate $\left\langle \varepsilon_\parallel^S \right\rangle_i$ parallel to the substrate can be calculated as an arithmetic average:

$$\left\langle \varepsilon_\parallel^S \right\rangle_i = \left(\sum_i f_i A_i \right) \sigma_\parallel^S , \tag{4.20}$$

where the subscript i indicates that the averaging has to be performed with respect to the various volume fractions. Thus, the averaged mechanical constant $\left\langle A \right\rangle_i$ reads in this case:

$$\left\langle A \right\rangle_i = \sum_i f_i A_i . \tag{4.21}$$

Analogously, the average mechanical constant $\left\langle B \right\rangle_i$ can be obtained from:

$$\left\langle B \right\rangle_i = \sum_i f_i B_i . \tag{4.22}$$

4.2.3. Direction-dependent grain interaction

4.2.3.1. The Vook-Witt model

Only recently, a direction-dependent grain-interaction model, based on adopting the grain-interaction assumptions of Vook and Witt, has been presented and tested experimentally by van Leeuwen *et al.* (1999). A generalised treatment for the case of (fibre-) texture is given in this work, see Chapter 3. The essentials will be briefly summarised here; for more details the reader is referred to van Leeuwen *et al.* (1999) and Chapter 3 of this work.

Thin films often exhibit a columnar microstructure. In such a film, in contrast with bulk specimens, each crystallite is surrounded by other crystallites in two dimensions only. The interaction between the columns in a direction perpendicular to the surface of the film can be assumed to be weak (there are often voids at the grain boundaries). As a consequence, the grain interaction cannot be the same for in-plane directions and the direction perpendicular to the film surface. For this reason, a columnar thin film will exhibit transversely isotropic elastic properties (even in the absence of texture), the surface normal being the axis of symmetry, whereas the traditional grain-interaction models are compatible only with macroscopic isotropy.

The Vook-Witt grain-interaction model is the first model taking the microstructure (of a thin film) into account. The assumptions are: (i) the strain is rotationally symmetric in the plane of the film and (ii) the in-plane strain is equal for all crystallites and (iii) the stresses

perpendicular to the layer are zero for all crystallites, i.e. the crystallites can deform freely in this direction. These assumptions fix parts of the stress and strain tensor for all crystallites:

$$\varepsilon^S = \begin{pmatrix} \varepsilon_\parallel^S & 0 & \Diamond \\ 0 & \varepsilon_\parallel^S & \Diamond \\ \Diamond & \Diamond & \Diamond \end{pmatrix}, \quad \sigma^S = \begin{pmatrix} \Diamond & \Diamond & 0 \\ \Diamond & \Diamond & 0 \\ 0 & 0 & 0 \end{pmatrix}. \tag{4.23},(4.24)$$

The tensor components marked by $\Diamond$ are not explicitly specified for every crystallite, but these components can be calculated from Hooke's law for every crystallite according to equation (4.15). Thus, for a particular value of the strain parallel to the substrate $\varepsilon_\parallel^S$, all non-zero strain and stress tensor components can be calculated by solving the system of equations (4.15) (for explicit equations, see Chapter 3.2.3). The elastic constants A and B can thus be calculated from (cf. also equations (4.8) and (4.9)) equations (4.16) and (4.17). The diffraction strain can be calculated following equation (4.5) and the stress factors follow from equation (4.18).

This model was applied to the stress analysis of an untextured nickel layer by van Leeuwen *et al.* (1999). Experimental findings not compatible with the traditional models, i.e. curved $\sin^2\psi$-plots in the absence of texture, became understandable as a consequence of the direction-dependent grain interaction.

However, the Vook-Witt assumptions represent extreme grain-interaction assumptions for the in-plane direction (crystallites are *tightly* connected together) and the direction perpendicular to the surface of the film (crystallites can deform *freely*, independent from neighbouring crystallites). It could be said: in terms of the bulk models, a Voigt behaviour is attributed to the in-plane directions, whereas a Reuss behaviour is attributed to the direction perpendicular to the film surface. For this reason, the Vook-Witt model will, in general, not be able to describe the true elastic behaviour of a real thin film. Therefore, the following development of a suitable 'average grain-interaction model' can be useful, as the experimental data presented later in this work will show.

It should be recognised that also in a bulk polycrystal, the elastic behaviour of crystallites located adjacent to the surface could be different from the elastic behaviour of crystallites located at some distance from the surface. This effect was first considered (on hypothetical basis) by Stickforth (1966) and named 'surface anisotropy'. In this case, the 'average grain-interaction model' proposed in this work may also be used for diffraction stress analysis. So far, experimental evidence of surface anisotropy lacks (Hauk, 1997, see also Hartmann, 1973, Nikolin, 1983 and discussion in Chapter 2.4), but only few investigators have paid attention to this phenomenon. Until recently (van Leeuwen *et al.*, 1999), also the

importance of direction dependent grain interaction for the elastic behaviour of thin films has not been realised. Thus, it should be recognised that, even if the following discussion is focused on thin films, the model proposed may also be applicable for the diffraction stress analysis of surface adjacent material of bulk polycrystals.

4.2.3.2. A generalised effective grain-interaction model

As compared to bulk materials where all directions for grain interaction can be equivalent, columnar thin films posses two principal directions exhibiting possibly different types of grain interactions; the in-plane direction (all in-plane directions are equivalent) and the direction perpendicular to the surface of the film. For this reason, the number of grain-interaction models of extreme types of grain-interaction assumptions is two for bulk materials (Reuss and Voigt, provided that all directions within the bulk are equivalent for grain interaction). But, on the basis of the same reasoning, four types of extreme grain-interaction models then can be formulated for columnar thin films, as two principal directions, each with two possible extreme grain interactions, occur (the Voigt and Reuss models and the Vook-Witt model have already been discussed):

1. *The Voigt model*

   All crystallites are tightly connected together with respect to both principal directions and exhibit identical strains.

2. *The Reuss model*

   All crystallites are subjected to identical stresses, but can deform freely with respect to both principal directions under these stresses.

3. *The Vook-Witt model*

   All crystallites are tightly connected together (or to a common substrate) with respect to the in-plane directions and exhibit identical in-plane strains, whereas they can deform freely in the perpendicular direction.

The fourth extreme model has not been presented before in the literature:

4. *The inverse Vook-Witt model*

   All crystallites can deform freely with respect to the in-plane directions under identical in-plane stresses, whereas they are tightly connected together with respect to the perpendicular direction and exhibit identical strains perpendicular to the surface.

The inverse Vook-Witt model

The inverse Vook-Witt model, is a new grain-interaction model. It is required for the construction of an effective grain-interaction model. The grain-interaction assumptions for this model are as follows: (i) the in-plane stress is rotational symmetric and (ii) equal for all crystallites and (iii) the strain perpendicular to the film surface is equal for all crystallites. Like in the (regular) Vook-Witt model, these assumptions fix certain strain and stress tensor components for all crystallites (cf. equations (4.23) and (4.24)):

$$\varepsilon^S = \begin{pmatrix} \lozenge & \lozenge & 0 \\ \lozenge & \lozenge & 0 \\ 0 & 0 & \varepsilon_\perp^S \end{pmatrix}, \qquad \sigma^S = \begin{pmatrix} \sigma_\parallel^S & 0 & \lozenge \\ 0 & \sigma_\parallel^S & \lozenge \\ \lozenge & \lozenge & \lozenge \end{pmatrix}. \tag{4.25},(4.26)$$

The missing strain and stress tensor components for each crystallite, marked by $\lozenge$, can be calculated by solving the system of equations (4.15).

For the calculation of the mechanical elastic constants, A and B, it is necessary to assure that $\sigma_\perp^S = \left\langle \sigma_{33}^S \right\rangle$ is zero (with the VW approach this is already assumed by the boundary conditions). The following approach can be followed:

Starting from arbitrary values for the in-plane stress $\sigma_{\parallel,1}^S$ and the strain perpendicular to the surface $\varepsilon_{\perp,1}^S$, the mechanical averages of the strain and stress tensor are calculated. In general, the stress perpendicular to the surface, $\sigma_\perp^S = \left\langle \sigma_{33}^S \right\rangle$, will be non-zero. However, by changing the mechanical strain perpendicular to the surface $\varepsilon_\perp^S$ (keeping $\sigma_\parallel^S$ fixed), $\sigma_\perp^S$ can be made zero, so that a plane, rotational symmetric stress state is achieved as required for a thin film unloaded in the direction perpendicular to the film surface. To this end, the above calculation has to be repeated for another value for the strain perpendicular to the surface, $\varepsilon_{\perp,2}^S$. As $\sigma_\perp^S$ is linearly related to $\varepsilon_\perp^S$,

$$\sigma_\perp^S = m \cdot \varepsilon_\perp^S + c \tag{4.27}$$

the strain making $\sigma_\perp^S$ equal to zero can be determined from equation (4.27) once the constants m and c have been calculated from the two (arbitrary) values of the strain perpendicular to the film surface $\varepsilon_{\perp,1}^S, \varepsilon_{\perp,2}^S$ and the corresponding stresses perpendicular to the

film surface $\sigma_{\parallel,1}^S$ and $\sigma_{\parallel,2}^S$. As an alternative, the mechanical stress parallel to the surface, $\sigma_{\parallel}^S$, can be varied with the mechanical strain perpendicular to the substrate, $\varepsilon_{\perp}^S$, fixed to assure that $\sigma_{\perp}^S = \left\langle \sigma_{33}^S \right\rangle$ is zero.

When it has been realised that $\sigma_{\perp}^S$ is zero for a given combination of $\sigma_{\parallel}^S$ and $\varepsilon_{\perp}^S$, the elastic constants A and B can be calculated according to (cf. equations (4.16) and (4.17)):

$$A = \frac{\varepsilon_{\parallel}^S}{\sigma_{\parallel}^S} = \frac{\left\langle \varepsilon_{11}^S \right\rangle}{\left\langle \sigma_{11}^S \right\rangle}, \tag{4.28}$$

$$B = \frac{\varepsilon_{\perp}^S}{\sigma_{\parallel}^S} = \frac{\left\langle \varepsilon_{33}^S \right\rangle}{\left\langle \sigma_{11}^S \right\rangle}. \tag{4.29}$$

The diffraction strain can be calculated following equation (4.5) and the stress factors follow from equation (4.18) (cf. also Chapter 2.1).

Constructing an effective grain-interaction model

On the basis of the models for the four types of extreme grain interaction, an effective grain interaction model can be constructed for a thin film (see discussion in Chapter 4.2.2). The following example is relevant to the present work.

The Reuss approach and the Vook-Witt approach are combined by assuming that a volume fraction f_R of the sample obeys the Reuss model and a volume fraction f_{VW} obeys the Vook-Witt model. Such a combined model leads, effectively, to partial in-plane Reuss-behaviour: whereas the crystallites are tightly connected together with respect to the in-plane direction in the Vook-Witt approach, the combination with the Reuss constraint gives the crystallites some degree of freedom for in-plane deformation independent of the neighbouring crystallites, by relieving the (unrealistic) constraint of identical planar strain for every crystallite.

A quantification of this effect of model mixing on the grain interaction can be achieved by defining interaction parameters for the two principal directions:

- in-plane interaction parameter $w_{\parallel}$: equals 1 for a Voigt-type interaction (crystallites are tightly connected together) and zero for a Reuss-type interaction (crystallites can deform independently of neighbouring crystallites but their stresses are identical)

- the out-of plane interaction parameter $w_\perp$: definition analogous to the in-plane parameter $w_\perp$, i.e. $w_\perp$ equals 1 for Voigt-type interaction and zero for a Reuss-type interaction.

Combining the models for extreme types of grain interaction results in average values $\langle w_\parallel \rangle$ and $\langle w_\perp \rangle$ for the interaction parameters:

$$\langle w_\parallel \rangle = \sum_i f_i w_{\parallel,i} \tag{4.30}$$

$$\langle w_\perp \rangle = \sum_i f_i w_{\perp,i}. \tag{4.31}$$

In equation (4.30) and equation (4.31), the f_i represent, like in equations (4.20) to (4.22), volume fractions of grains obeying the grain-interaction model i:

$$\sum_i f_i = 1. \tag{4.32}$$

The four models for the extreme types of grain interaction are summarised, together with the in-plane and out-of-plane interaction parameters, in table 4.1.

For a given combination of grain-interaction models, the average interaction parameters can be calculated following equation (4.30) and equation (4.31). However, it is obvious that the same values of the interaction parameters can be realised by different combinations of the grain-interaction models. As an example, $w_\parallel = 0.5$ and $w_\perp = 0.5$ can be realised by the effective model with $f_R = 0.5$ and $f_V = 0.5$ and by the effective model with $f_{VW} = 0.5$ and $f_{IVW} = 0.5$ as well. Numerical evaluations of the mechanical elastic constants A and B

Table 4.1: Grain interaction models (first column) with grain-interaction assumption for the in-plane direction (second column, V...Voigt type of grain interaction, i.e. crystallites are tightly connected, R...Reuss type of grain interaction, i.e. crystallites can deform freely) and for the direction perpendicular to the sample surface (third column) and the corresponding grain-interaction parameters $w_\parallel$ and $w_\perp$ (fourth and fifth columns).

	in-plane direction	perpendicular to sample surf.	$w_\parallel$	$w_\perp$
Voigt	V	V	1	1
Reuss	R	R	0	0
Vook-Witt	V	R	1	0
inverse Vook-Witt	R	V	0	1

exhibit, that their values are practically independent of the choice of combination of models as long as the same values of the interaction parameters $\langle w_\parallel \rangle$ and $\langle w_\perp \rangle$ hold (see last two columns of table 4.3 for an example; calculation using single crystal elastic constants for copper taken from table 4.2).

However, this does not hold for the diffraction strain (or the stress factors), as can be seen in figure 4.2 (calculation using single crystal elastic constants for copper taken from table 4.2): noticeable differences (large enough to be detected in a lattice strain measurement) in the diffraction strain occur as function of $\sin^2\psi$ for different combinations of grain-interaction models, although the same set of values holds for the parameters $\langle w_\parallel \rangle$ and $\langle w_\perp \rangle$.

This observation is not in contradiction to the (approximate) independence of the elastic constants A and B for the type of grain interaction: the diffraction strain stems only from a fraction of all crystallites, whereas the mechanical elastic constants are calculated as averages for all crystallites. Therefore, diffraction strain analysis is a sensitive method to investigate direction dependent grain interaction.

Table 4.2: Single crystal elastic constants (Meyers & Chawla, 1984) and anisotropy factor used. The compliance matrix components s_{ij} have been given together with the anisotropy factor A_i (see Chapter 4.3). The Voigt two-index notation (see, for example, Hauk, 1997) is used; to change to the tensorial notation, the indices must be replaced following the scheme: $s_{ij} \rightarrow s_{mnop}$, $i \rightarrow mn$, $j \rightarrow op$ with $1 \rightarrow 11$, $2 \rightarrow 22$, $4 \rightarrow 12$ and recognizing that $s_{ij} = 4 s_{mnop}$ if $i, j > 3$.

	s_{11} (TPa^{-1})	s_{12} (TPa^{-1})	s_{44} (TPa^{-1})	A_i
Cu (fcc)	14.98	-6.29	13.26	3.21
Nb (bcc)	6.90	-2.49	34.20	0.55

Table 4.3: Macroscopic, mechanical elastic constants A and B according to the separate grain-interaction models and two effective models ($f_R = f_V = 0.5$ and $f_{VW} = f_{IVW} = 0.5$) for an untextured copper film. The single crystal elastic constants of copper given in Table 2 have been used.

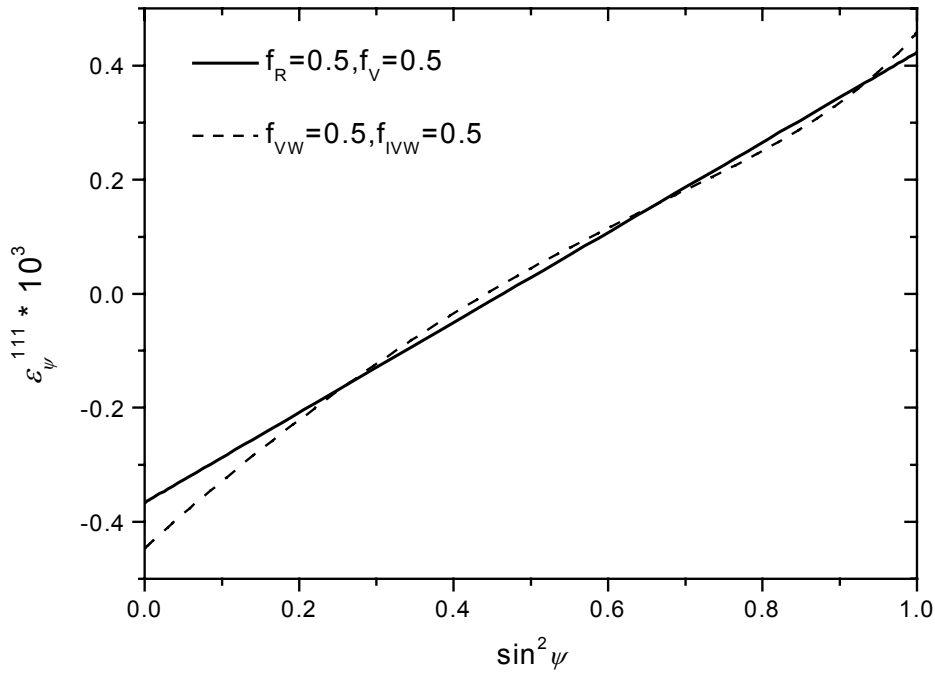|	$f_V = 1$	$f_R = 1$	$f_{VW} = 1$	$f_{IVW} = 1$	$f_R = f_V = 0.5$ $w_\parallel = w_\perp = 0.5$	$f_{VW} = f_{IVW} = 0.5$ $w_\parallel = w_\perp = 0.5$
A (TPa^{-1})	4.65	5.77	5.24	4.92	5.21	5.08
B (TPa^{-1})	-4.50	-6.73	-5.68	-5.03	-5.62	-5.36

Figure 4.2: Calculated diffraction strain for the 111 reflection of an untextured copper film subjected to a plane, rotationally symmetric, tensile stress of 100MPa for two effective grain-interaction models: a combination of the Voigt and the Reuss model ($f_R=f_V= 0.5$, continuous line) and a combination of the Vook-Witt and the inverse Vook-Witt model ($f_{VW}= f_{IVW} = 0.5$, dashed line).

4.3. Diffraction-strain simulations on the basis of the various grain-interaction models

Based on equation (4.5), simulations of diffraction strain have been carried out for two different cubic materials with two distinctly different extents of elastic anisotropy as characterised by the anisotropy factor:

$$A_i = \frac{\left(s_{1111}^C - s_{1122}^C\right)}{2s_{1212}^C}. \tag{4.33}$$

Niobium (A_i=0.49) and copper (A_i=3.20) were selected for the simulations. The single-crystal

elastic compliances corresponding to the C system have been summarised in table 4.2. For most of the known materials, the anisotropy is in the range defined here by the "limiting" values of A_i for niobium and copper. For each material, the (X-ray) diffraction strain was calculated and has been presented as a function of $\sin^2\psi$ (in the so-called $\sin^2\psi$-plot), for a number of reflections. The calculations were performed assuming an average stress $\sigma_{\parallel}^S$=100MPa for the film. In addition, the mechanical elastic constants A and B have been calculated following equations (4.16) and equation (4.17).

Copper Film

Copper is strongly elastically anisotropic: the anisotropy factor is much larger than one, i.e. the $<00l>$ direction is much softer than the $<hhh>$ direction. The calculations were conducted for an untextured copper film, imposing a tensile, rotationally symmetric in-plane stress of 100MPa. For an intrinsically elastically isotropic material, only straight, coinciding lines can be expected in the $\sin^2\psi$-plots. Clearly, as follows from figures 4.3a and 4.3b, in general the results for the various types of grain interaction do not coincide, and also distinct curvature occurs in the $\sin^2\psi$-plots.

Due to the elastic anisotropy of copper, the maximum (absolute) diffraction strain is equal or higher for the 200 reflection than for the 111 reflection for a particular grain-interaction model (note that this statement, in fact, holds not only for the maximum strain but also for large parts of the $\sin^2\psi$-range). Whereas, in the absence of texture, linear $\sin^2\psi$-plots are obtained for all reflections from the traditional models (Reuss, Voigt), this is not the case for the direction-dependent grain-interaction models (Vook-Witt, inverse Vook-Witt; see figures 4.3a, 4.3b, 4.3c and 4.3d; note that, although hardly visible, also in figure 4.3d a curved behaviour can be observed). This result is caused by the *macroscopic* anisotropy of the specimen, in case of direction-dependent grain interaction: the specimen presents mechanically anisotropic behaviour when it obeys the Vook-Witt or the inverse Vook-Witt grain-interaction models, whereas macroscopically isotropic behaviour results when the film obeys one of the traditional grain-interaction models.
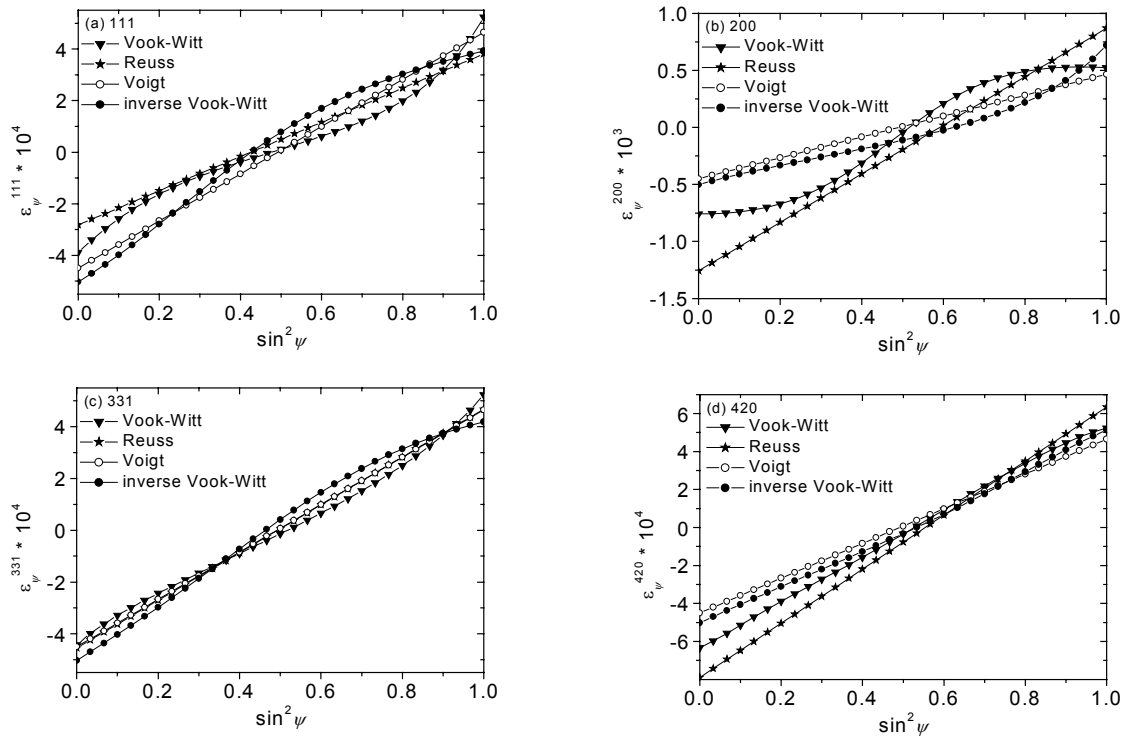
Figure 4.3: Untextured copper film subjected to a plane, rotational symmetric state of stress (tensile stress, 100MPa). Simulations of the diffraction strain ε_ψ^{hkl} versus $\sin^2\psi$ ('$\sin^2\psi$-plot') for (a) the 111, (b) the 200, (c) the 331 and (d) the 420 reflection. A legend indicating the symbols used for the different grain-interaction models has been given in the figures.

The (additional) effect of texture on the $\sin^2\psi$-plots is demonstrated in figure 4.4; a {111}-fibre-texture with a pole width of 5° half width at half maximum was assumed for the calculation. The volume fraction of diffracting crystallites, as represented by the integrated intensity of a diffraction line in a measurement, is indicated in the figures by the continuous line. Major differences become evident upon comparing figure 4.3 and figure 4.4. As a consequence of the presence of texture, the calculation of the diffraction strain, as well as its measurement for a real sample with the texture considered, is not possible for all tilt angles ψ, and therefore certain ranges of the $\sin^2\psi$-plot cannot be accessed (see figures 4.4a, b, c and d). The Reuss model yields non-linear $\sin^2\psi$-plots for the 331 and the 420 reflections (figures 4.4c and 4.4d), whereas the 111 and the 200 reflections still exhibit linear behaviours (figures 4.4a and 4.4b). This non-linearity observed for the Reuss model is a consequence of the texture, leading to an anisotropic (i.e. transversely isotropic) mechanical behaviour of the film. For the Voigt model, linear $\sin^2\psi$-plots are obtained independently of the texture.
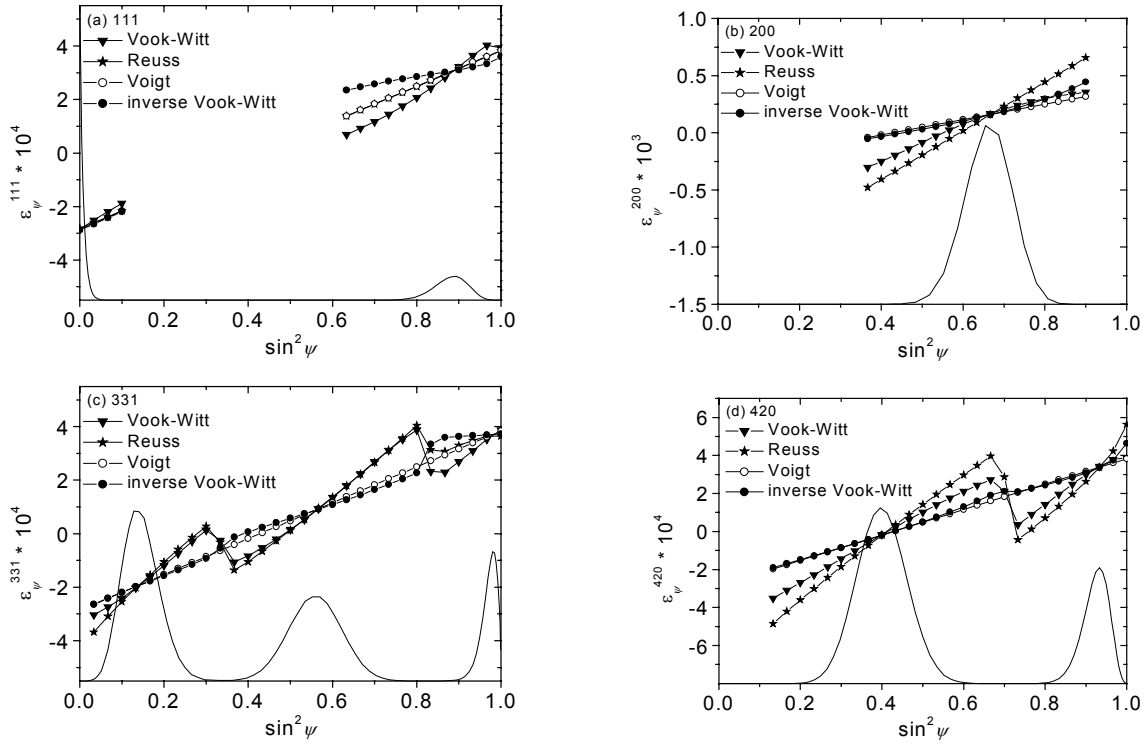
92

Figure 4.4: Textured copper film (Gaussian {111}-fibre texture, 5° pole half width at half maximum) subjected to a plane, rotational symmetric state of stress (tensile stress, 100MPa). Simulations of the diffraction strain ε_ψ^{hkl} versus $\sin^2\psi$ ('$\sin^2\psi$-plot') for (a) the 111, (b) the 200, (c) the 331 and (d) the 420 reflection. A legend indicating the symbols used for the different grain-interaction models has been given in the figures. The relative integrated intensity is also shown in the figures (lines without dots; arbitrary units).

A general observation is, that the $\sin^2\psi$-plots of the Vook-Witt model and those of the inverse Vook-Witt model exhibit curvatures with opposite signs for large portions of the $\sin^2\psi$-range.

The macroscopic, mechanical elastic constants A and B are summarised (for both cases: no texture and fibre texture) in table 4.4 for the grain-interaction models Voigt, Reuss, Vook-Witt, inverse Vook-Witt. The mechanical elastic constants are bounded by the constants calculated according to the Voigt and the Reuss model. Due to the pronounced intrinsic elastic anisotropy of copper, the macroscopic elastic constants of the textured film differ significantly from those for an untextured film.

Table 4.4: Macroscopic, mechanical elastic constants A and B of a copper film (untextured and fibre textured; {111} fibre texture with a pole width of 5° half width at half maximum) according to the grain-interaction models Voigt, Reuss, Vook-Witt, inverse Vook-Witt and Neerfeld-Hill. Single crystal elastic data taken from Meyers & Chawla (1984).

Cu		R	V	VW	IVW	NH
no	A (TPa^{-1})	5.77	4.65	5.24	4.92	5.21
texture	B (TPa^{-1})	-6.73	-4.50	-5.68	-5.03	-5.62
fibre-	A (TPa^{-1})	3.89	3.83	3.86	3.84	3.85
texture	B (TPa^{-1})	-2.98	-2.87	-2.92	-2.88	-2.93

Niobium Film

Diffraction-strain simulations have been conducted also for an untextured film and a film with fibre texture. For niobium, a bcc-metal, the occurrence of a {110}-texture is more likely than the occurrence of a {111}-texture; thus, a {110}-fibre texture with a pole width of 5° half width at half maximum was used. For niobium, the anisotropy factor is smaller than one, i.e. the $<00l>$ direction is stiffer than the $<hhh>$ direction. In the absence of texture, linear $\sin^2\psi$-plots are obtained for all reflections from the traditional models (Reuss, Voigt); this is not the case for the direction-dependent grain-interaction models (Vook-Witt, inverse Vook-Witt, see figures 4.5a, b, c and d; note that, although hardly visible, also in figures 4.5a and d a curved behaviour can be observed). Due to the elastic anisotropy of niobium, the maximum (absolute) diffraction strain is equal or higher for the 222 reflection than for the 200 reflection.

The effect of texture on the $\sin^2\psi$-plots is presented in figure 4.6: analogous effects as for copper can be seen: the Voigt model yields linear $\sin^2\psi$-plots for all reflections; the Reuss model results in non-linear $\sin^2\psi$-plots for a textured film for the 110- and the 321-reflection, whereas the $\sin^2\psi$-plot for the 200 and the 222 reflections is linear. Again, as a general observation, the $\sin^2\psi$-plots of the direction dependent grain-interaction Vook-Witt and inverse Vook-Witt models exhibit curvatures with opposite signs for large portions of the
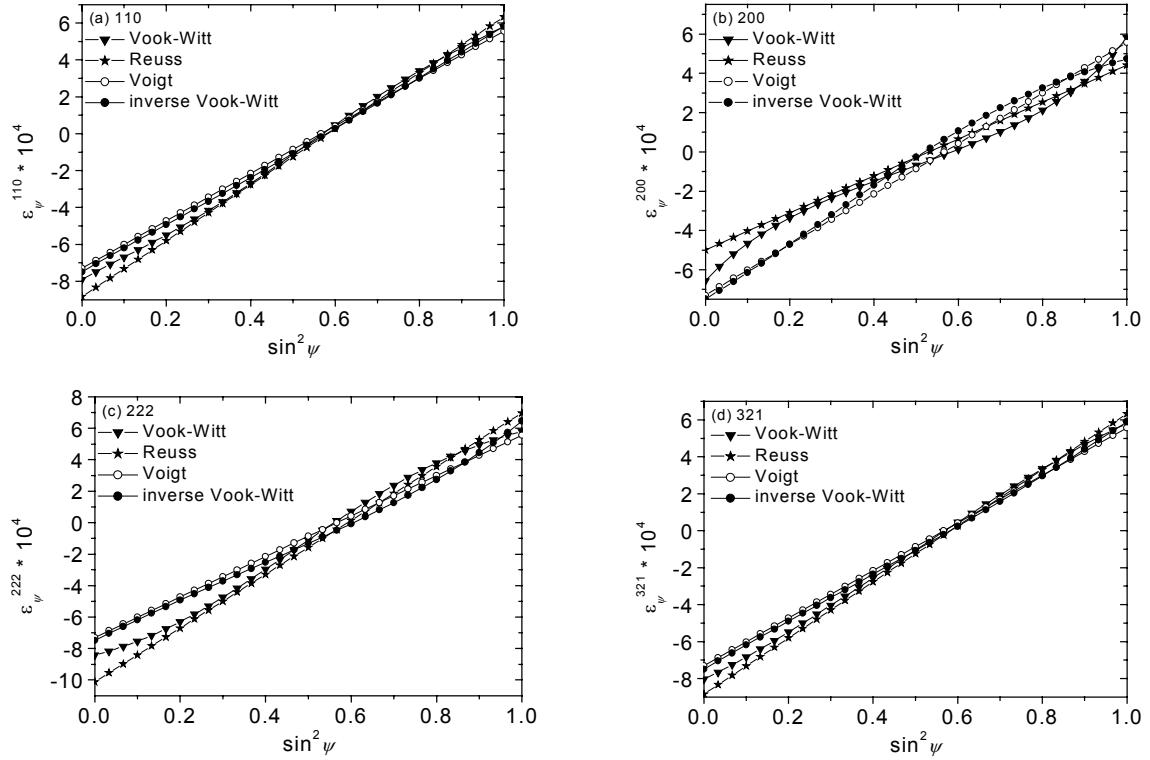
Figure 4.5: Untextured niobium film subjected to a plane, rotational symmetric state of stress (tensile stress, 100MPa). Simulations of the diffraction strain ε_ψ^{hkl} versus $\sin^2 \psi$ ('$\sin^2 \psi$-plot') for (a) the 111, (b) the 200, (c) the 331 and (d) the 420 reflection. A legend indicating the symbols used for the different grain-interaction models is given in the figures.

Table 4.5: Macroscopic, mechanical elastic constants *A* and *B* of a niobium film (untextured and fibre textured; {110}-fibre texture with a pole width of 5° half width at half maximum) according to the grain-interaction models Voigt, Reuss, Vook-Witt, inverse Vook-Witt and Neerfeld-Hill. Single crystal elastic data taken from Meyers & Chawla (1984).

Nb		R	V	VW	IVW	NH
no	A (TPa^{-1})	5.95	5.57	5.81	5.66	5.76
texture	B (TPa^{-1})	-8.06	-7.30	-7.78	-7.49	-7.68
fibre-	A (TPa^{-1})	6.32	5.99	6.11	6.30	6.16
texture	B (TPa^{-1})	-8.80	-8.14	-8.38	-8.75	8.47

$\sin^2 \psi$-range.

The macroscopic, mechanical elastic constants A and B are summarised (for both cases: no texture and fibre texture) in table 4.5 for the grain-interaction models Voigt, Reuss, Vook-Witt, inverse Vook-Witt.

Due to the intrinsic elastic anisotropy of niobium, the elastic constants of the textured film differ from those obtained for an untextured film (cf. above results for copper).
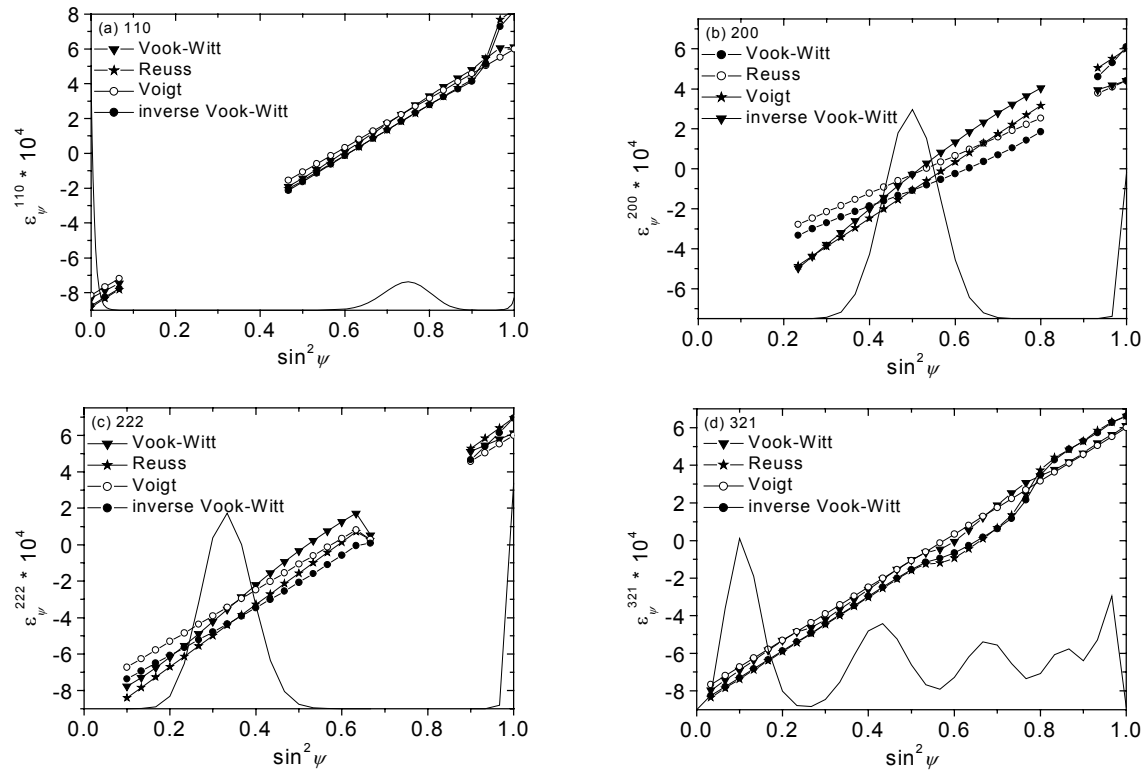

Figure 4.6: Textured niobium film (Gaussian {110}-fibre texture, 5° pole half width at half maximum) subjected to a plane, rotational symmetric state of stress (tensile stress, 100MPa). Simulations of the diffraction strain ε_ψ^{hkl} versus $\sin^2\psi$ ('$\sin^2\psi$-plot') for (a) the 110, (b) the 200, (c) the 222 and (d) the 321 reflection. A legend indicating the symbols used for the different grain-interaction models has been given in the figures.

4.4. Stress analysis on the basis of an effective grain-interaction model

Generally, a stress analysis can be done as follows (for a review of different methods of diffraction stress analysis, see also Welzel *et al.*, 2002). When the diffraction (X-ray) elastic constants (in the case of macroscopically elastically isotropic specimens; cf. equation (4.12)) or stress factors (in the case of macroscopically elastically anisotropic specimens; cf. equation (4.10)) are known, either by measurement or by calculation from single crystal elastic data by adopting a grain-interaction model, the unknown stress tensor components can be obtained as fit parameters in a (least-squares) minimisation of the difference χ^2,

$$\chi^2 = \sum_i \omega_i^2 \left(\varepsilon_i^{calc} \left(\left\langle \sigma^S \right\rangle, hkl, \varphi, \psi \right) - \varepsilon_i^{meas} \left(hkl, \varphi, \psi \right) \right)^2 \tag{4.34}$$

where ε_i^{meas} represents the measured lattice strains.

The index *i* stands for all measured lattice strains (for all different ψ, φ and/or *hkl* analysed). The ω_i are weighing factors which can be used to reflect the statistical relevance of the measured strains $\varepsilon_i^{meas} \left(hkl, \varphi, \psi \right)$ in the result of the minimisation and could correspond to the inverse of the standard deviations of the measured strains.

For the case of macroscopically elastically anisotropic specimens, the diffraction strains, ε_i^{calc}, have to be calculated following equation (4.12)

$$\varepsilon_i^{calc} \left(\left\langle \sigma^S \right\rangle, hkl, \varphi, \psi \right) = F_{kl}(\psi, \varphi, hkl) \left\langle \sigma_{kl}^S \right\rangle . \tag{4.35}$$

For the case of macroscopically elastically isotropic specimens, the diffraction strains, ε_i^{calc}, can be calculated following equation (4.10):

$$\begin{aligned}
\varepsilon_i^{calc} \left(\left\langle \sigma^S \right\rangle, hkl, \varphi, \psi \right) &= \tfrac{1}{2} S_2^{hkl} \sin^2 \psi \left(\left\langle \sigma_{11}^S \right\rangle \cos^2 \varphi + \left\langle \sigma_{12}^S \right\rangle \sin(2\varphi) + \left\langle \sigma_{22}^S \right\rangle \sin^2 \varphi \right) + \\
&\quad + \tfrac{1}{2} S_2^{hkl} \left(\left\langle \sigma_{13}^S \right\rangle \cos \varphi \sin(2\psi) + \left\langle \sigma_{23}^S \right\rangle \sin \varphi \sin(2\psi) + \left\langle \sigma_{33}^S \right\rangle \cos^2 \psi \right) \\
&\quad + S_1^{hkl} \left(\left\langle \sigma_{11}^S \right\rangle + \left\langle \sigma_{22}^S \right\rangle + \left\langle \sigma_{33}^S \right\rangle \right)
\end{aligned} \tag{4.36}$$

Note that equation (4.35) could be used as well in this case, but the use of equation (4.34), based on ψ- and φ-independent X-ray elastic constants may be more convenient.

The following variant of the above-described method is relevant to the present work. If the type of grain interaction, i.e. the parameters f_i (cf. Chapter 4.2.2), are not known a priori, they can be used as fitting parameters in addition to the unknown stress tensor components (cf. Serruys *et al.*, 1989). It is suggested to use measured data from multiple reflections

simultaneously in the fitting, which can considerably improve the uniqueness of the obtained fit results.

In the present work, the analysis has been focused on untextured and fibre textured specimens subjected to a plane, rotationally symmetric state of stress. In this case, only one stress tensor component, $\left\langle \sigma_{11}^{S} \right\rangle = \left\langle \sigma_{22}^{S} \right\rangle = \sigma_{\parallel}^{S}$, has to be determined. Thus, following the above described method, four parameters ($\sigma_{\parallel}^{S}$ and the three volume fractions f_i, cf. Chapter 4.2.3.2) have to be determined on the basis of equation (4.34).

The required minimum number of reflections and the minimum number of lattice-strain measurements at different tilt angles for a particular reflection cannot be given in general. However, it should be noted in this context that the *hhh* and 00*l* reflections always yield linear $\sin^2 \psi$-plots (in the absence of shear stresses, which lead to elliptical $\sin^2 \psi$-plots), independent of texture, according to a grain-interaction model consisting of a mixture of only the Reuss and Voigt models. For that reason, deviations of the actual grain interaction from these traditional models (Reuss, Voigt) are easily detected from lattice-strain measurements using the *hhh* and 00*l* reflections: whenever non-linear $\sin^2 \psi$-plots are obtained for these reflections (and the influence of other sources of curvature, like depth gradients, can be excluded), one of the direction-dependent grain-interaction models has to be incorporated in the analysis.

4.5. Experiment

4.5.1. Copper-layer preparation

Copper films of thickness 500nm were sputter deposited onto pieces (size 14mm x 14mm) of an thermally oxidised <510>-silicon wafer using a dc-magnetron with a copper target (purity 99.95 at.-%) in an ultra high vacuum chamber (base pressure below $2 \cdot 10^{-10}$ mbar). In one deposition run, four samples were prepared. The magnetron was operated at 100W using precleaned (Messer Griessheim Oxisorb gas cleaning cartridge) Ar 6.0 with a pressure of $3.5 \cdot 10^{-3}$ mbar as a sputter gas. Immediately before the layer deposition the substrates were cleaned by heating them to 673K and, after cooling down to room temperature, by argon ion bombardment using an ion gun. The film thickness was determined by calibration of the deposition rate using a stylus profilometer (Dektak). For this purpose a sample with a step in height was produced.

4.5.2. Focused ion beam microscopy

The microstructure (grain shape and size) was investigated by using a FEI Fib 200 ion beam workstation. The workstation allows cutting cross-sections and their imaging with the help of a Ga-ion beam. The images were taken employing an ion beam current of 67pA at a viewing angle of 45° after cutting a cross section.

4.5.3. X-ray diffraction measurement

The X-ray diffraction measurements were carried out using a Philips X'Pert MRD Pro diffractometer equipped with an Eulerian cradle (4-circle goniometer). Cu Kα radiation emerging from the point focus of a sealed X-ray tube operated at 45kV and 40mA was paralleled by an X-ray lens. The lens aperture had a diameter of approximately 7mm. The size of the beam was adjustable by crossed slits placed directly in front of the lens and the size was set to 4mm by 4mm for all measurements. The diffracted beam passed a parallel plate collimator (0.27° acceptance angle) and a flat graphite analyser set to select CuKα radiation before being detected by a proportional counter. Diffraction patterns were recorded in continuous mode. The sample tilt angle ψ was varied in step mode from 0° to 90° with a step size of 3°.

Table 4.6: Measurement parameters for diffraction measurements of lattice strain from a sputtered, 500nm thick copper film: *hkl*, 2θ-range, step size($\Delta 2\theta$) and counting time per step.

reflection	$2\theta_{min}$ (°)	$2\theta_{max}$ (°)	steps size (°)	counting time (s)
111	40.5	46.5	0.05	20
200	47.5	53.5	0.05	25
220	71.0	77.0	0.05	25
311	87.0	93.0	0.05	30
331	131.0	141.0	0.1	50
420	140.0	150.0	0.1	50

For some reflections, the measurements were performed also at negative ψ and at various φ to verify that the results obtained were independent of the sign of the tilt angle and of the selection of a particular φ angle. The measurement ranges were at least ten times the full width at half maximum of the α_1 peak of a diffraction line. The scan parameters for the measured reflections have been gathered in table 4.6.

4.5.3.1 Determination of peak position and integrated intensity

Diffraction patterns were evaluated by fitting split Pearson VII functions (for the definition of the profile function, see for instance Sonneveld *et al.*, 1991) using a custom peak fit program. Peak positions, heights, half widths at half maximum (HWHM), asymmetries and shape parameters were refined. No significant differences of the peak position and the integrated intensity were observed for symmetric and asymmetric peak fits. The Kα2 component was taken into account by simultaneous fitting of two Pearson VII functions, one for each radiation component. A Kα2:Kα1 intensity ratio of 0.5 was assumed (this assumption was checked by setting the ratio free as a fit parameter for some evaluations). For each diffraction peak (or group of overlapping diffraction peaks) a linear background was fitted.

4.5.3.2 Determination of the Orientation Distribution Function

The integrated areas of six diffraction lines (see table 4.6) were determined by peak fitting (see above). The integrated intensity depended on the sample tilt angle ψ but was independent of the rotation angle φ (see Chapter 4.6). Thus, it can be concluded that the layer exhibited a

fibre texture. In this case, pole figures exhibit rotational symmetry (for rotation around the fibre axis) and the pole figure can be constructed from only the ψ-dependency of the integrated intensity.

Pole figures for the 111 and the 200 reflections were generated from the measured integrated intensity of the diffraction lines measured as a function of the tilt angle ψ considering the fibre-symmetry, i.e. the same integrated intensity was attributed to every φ for a given ψ. A step size of 3° was used in φ and ψ. The pole figures obtained in this way cannot be used without more ado for the calculation of the orientation distribution function, because instrumental effects obstruct an interpretation of integrated intensities in terms of volume fractions. The pole figures have to be corrected for absorption, the increase of illuminated sample area upon tilting the sample and instrumental intensity loss occurring if a fraction of the incident beam misses the sample surface or a fraction of the diffracted beam misses the detector. For details of the corresponding correction procedure applied here, see Chapter 5.

For the correction of the integrated intensities for instrumental intensity loss, standard measurements for eight reflections from a texture-free tungsten powder sample were used. The absorption corrections were performed using the linear (bulk) absorption coefficient of copper (0.04559 $1/\mu$m, Leroux & Thinh, 1977) and the sample thickness value of 500nm. The ODF was calculated from the corrected pole figures (111 and 200 reflections) using the software package X'Pert Texture (Philips Analytical, Almelo, The Netherlands). The use of more than two reflections for texture analysis did not change the resulting orientation distribution function, thus two reflections are sufficient for the ODF calculation (see below). The ODF was exported in ASCII-format (on a grid with 3° spacing for the three Euler angles) and used in the calculations of the elastic constants (see equations (4.16) and (4.17)), the diffraction strain (see equation (4.5)) and the X-ray stress factors (see equation (4.18)).

4.6. Results and discussion

4.6.1. Focused ion beam microscopy

An image of the microstructure is shown in figure 4.7. The top view and the cross section can be seen in one image. To that end, a rectangular section of the layer was removed using a Ga ion sputter beam.
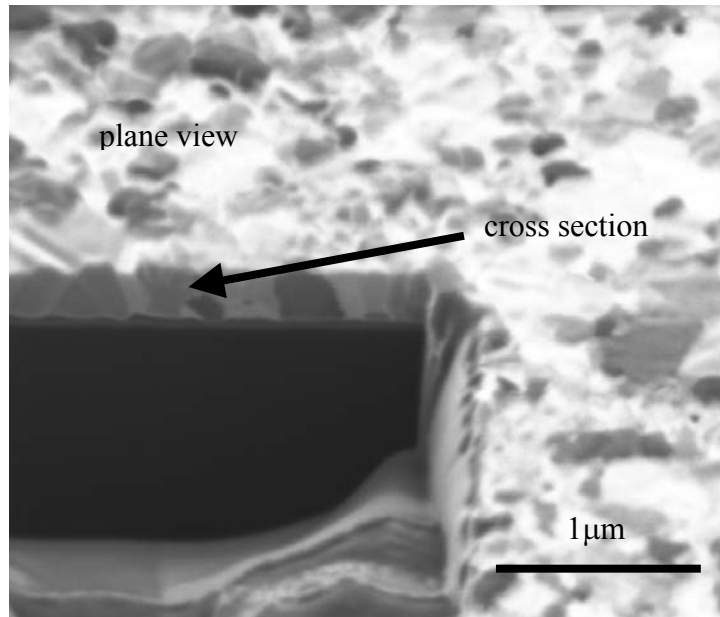
Figure 4.7: Micrograph of the investigated copper specimen taken with a focused ion beam workstation. Before taking the image, a rectangular section of the layer was removed by sputtering (employing the Ga-ion beam). For imaging, the specimen was inclined by 45° with respect to the ion beam. Thus, the cross section is visible simultaneously with the plane view.

The layer has a columnar microstructure; grain boundaries of most grains are extending from the interface to the layer surface. The lateral grain size is of the order of the film thickness, 500nm.

4.6.2. Texture

The investigated copper sample has a pronounced {111}-fibre texture with minor additional texture components. The integrated intensity as measured and corrected (cf. Chapter 4.5.3.2) and as recalculated from the orientation distribution function (ODF) is presented in Figure 4.8 as a function of the sample tilt angle ψ.
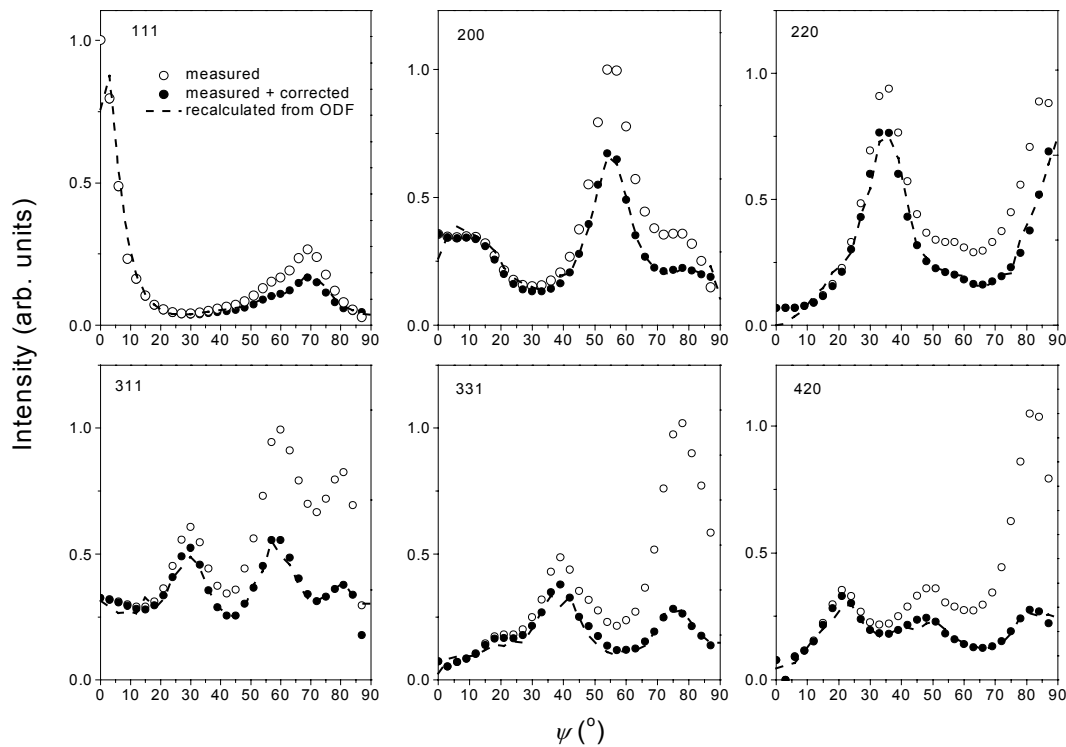
Figure 4.8: Textured copper film. The experimentally determined integrated intensity for six diffraction peaks as a function of the sample tilt angle ψ: as measured (open circles), as measured and corrected for absorption and instrumental aberrations (filled circles), and as recalculated from the corresponding orientation distribution function (dashed line). The orientation distribution function was calculated on the basis of pole figures for the 111 and the 200 reflection.

Clearly, the ODF, as derived from the 111 and the 200 reflections, provides a very good representation of the texture of the specimen; excellent agreement is observed also for the intensities of the reflections that have not been used for the calculation of the orientation distribution function. It should be recognised that the correction of the measured intensity (cf. Chapter 4.5.3.2) is a prerequisite to arrive at such a consistent texture representation.

4.6.3. Stress

As the diffraction-line positions for a particular reflection *hkl* and tilt angle ψ were found to be independent of the rotation angle φ, the stress state is rotationally symmetric. Shear components do not occur because no splitting of the $\sin^2\psi$-plots for positive and negative ψ, typical for the presence of shear stresses, was observed. It follows, that only one

(independent) stress tensor component had to be determined, namely the stress parallel to the substrate, $\sigma_{\parallel}^S = \left\langle \sigma_{11}^S \right\rangle = \left\langle \sigma_{22}^S \right\rangle$.

The lattice strain ε_ψ^{hkl} was calculated from the measured hkl lattice plane spacing d_m^{hkl} and the strain-free hkl lattice plane spacing d_0^{hkl} :

$$\varepsilon_\psi^{hkl} = \frac{d_m^{hkl} - d_0^{hkl}}{d_0^{hkl}} \qquad (4.37)$$

To this end, the spacing of the hkl lattice planes was calculated from the measured peak position $2\theta_m^{hkl}$ by using Bragg's law (a wavelength of 1.540562Å for the Kα_1 component of copper radiation was used (International Tables For X-ray Crystallography, 1974). For the determination of d_0^{hkl}, see below.

For an accurate determination of the stress, the lattice- (diffraction-) strain measurements should have accuracy in the order 10^{-5}. The measurement of peak *shifts* ($\Delta 2\theta$) with the required accuracy poses no problems when the diffractometer is well aligned (note that alignment errors are less critical in the parallel beam set-up used as compared to a focusing, e.g. Bragg-Brentano geometry), sufficiently long counting times are used and the measurement temperature and the temperature of the cooling water of the X-ray source are controlled to within a few Kelvin. The absolute determination of the peak *position* is, in general, more difficult, as instrumental effects (in particular a shift of the zero position of the goniometers 2θ scale and the instrumental contribution to the peak broadening), unimportant for tracing peak shifts, can be of crucial importance for the absolute determination of the peak position. However, when multiple reflections are combined in a stress analysis, as suggested in Chapter 4, absolute peak positions have to be measured very accurately.

Two approaches have been followed for dealing with this difficulty.
(i) One possibility is to use the strain free lattice spacing d_0^{hkl} for each $\sin^2\psi$-plot used in a stress analysis as an additional fit parameter. In this way, no accurate determination of the *absolute* peak position is required. In this case, ten fit parameters are determined from six $\sin^2\psi$-plots, each corresponding to one hkl reflection: six strain free lattice spacings d_0^{hkl}, the stress parallel to the substrate $\sigma_{\parallel}^S$ and three (independent) volume fractions pertaining to the effective grain-interaction model involved (i.e. the Voigt, Reus, Vook-Witt and inverse Vook-Witt contributions). Note that the strain free lattice spacings have no direct physical meaning

and *cannot* be used for the calculation of the lattice constant *a*, as they are biased by instrumental errors.

Following approach (i), the measured $\sin^2\psi$-plots for six reflections have been presented in figure 4.9 together with the simulation corresponding to the fit. Clearly, a very good agreement between experiment and fit has been achieved. The results of the fit are:

- $\sigma_\parallel^S = 165$MPa (tensile),

- volume fractions for the grain-interaction models: $f_{VW} = 0.6, f_R = 0.3, f_{IVW} = 0.1, f_V = 0.0$
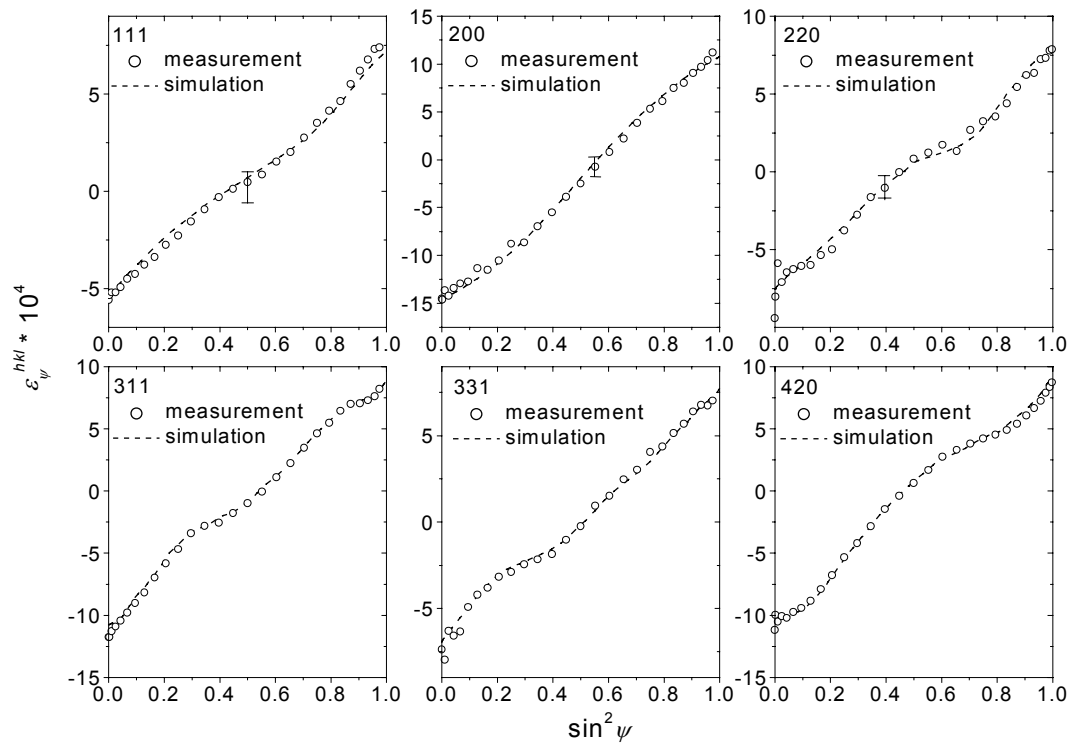
Figure 4.9: Textured copper film. Measured (open circles) and simulated (dashed line) diffraction strain data for six different reflections as function of $\sin^2\psi$ ($\sin^2\psi$ - plots). For details of the simulation, see text.

(ii) Considering that the only significant instrumental error for the parallel beam geometry used in the investigations is a zero-shift of the goniometer 2θ-scale, the number of fit parameters can be reduced. Thus, an alternative approach can be realised by taking the zero-shift, $\Delta\theta_0$, as an additional fitting parameter together with the strain free lattice constant a.

In this case, the lattice strain derived from the *hkl* planes, d_m^{hkl}, is calculated as follows:

$$\varepsilon_\psi^{hkl} = \frac{\dfrac{\lambda}{2\sin\left(\left(2\theta_\psi^{hkl}\right)/2 - \Delta\theta_0\right)} - \dfrac{a}{\left(\sqrt{h^2 + k^2 + l^2}\right)}}{\dfrac{a}{\left(\sqrt{h^2 + k^2 + l^2}\right)}}, \tag{4.38}$$

where $2\theta_\psi^{hkl}$ is the diffraction angle of the *hkl* reflection at tilt ψ.

In this approach, the following fit parameters occur: the strain-free lattice constant, the zero-shift of the goniometers 2θ-scale, the stress parallel to the substrate $\sigma_\parallel^S$ and the three (independent) volume fractions pertaining to the grain-interaction models involved. Thus the number of fitting parameters is six, as compared to ten in approach (i).

Following approach (ii), very good agreement between experiment and fit occurs as well. The results of the fit are:

- $\sigma_\parallel^S = 165\text{MPa (tensile)}$,

- volume fractions for the grain-interaction models, $f_{VW} = 0.6, f_R = 0.3, f_{IVW} = 0.1, f_V = 0.0$,

- strain free lattice parameter $a_0 = 3.6153\text{Å}$ (literature value: 3.615Å, Powder Diffraction File, Release 2000, International Centre for Diffraction Data),

- goniometer 2θ-scale zero shift $= 0.01°$ (this zero shift value is compatible with results from separate recordings of the position of the direct beam).

4.6.4. Discussion

Evidently, the traditional models cannot describe the measured $\sin^2\psi$-plots of the thin copper film analysed. Of course, fitting to *only one* $\sin^2\psi$-plot using only one of the traditional grain-interaction models (this is the procedure usually applied in the literature) is possible, see figure 4.10 for an example, but it is impossible to obtain a consistent fit for a single traditional grain-interaction model by fitting simultaneously to all measured $\sin^2\psi$-plots (one for each measured reflection). This emphasises the need for the procedure of diffraction-stress analysis proposed in this paper.

In particular is should be noted, that any combination of the Reuss model with the Voigt model (e.g. the traditional Neerfeld-Hill model) predicts linear $\sin^2\psi$-plots for the *hhh* and 00*l* reflections; obviously, the measured $\sin^2\psi$-plots for the 111 and 200 reflections cannot be described by straight lines. Only the direction-dependent grain-interaction models are compatible with the curved behaviour in the $\sin^2\psi$-plots observed for these two reflections.

An interpretation of the parameters representing the volume fractions of the grain-interaction models, $f_{VW} = 0.6, f_R = 0.3, f_{IVW} = 0.1, f_V = 0.0$, may be as follows. The in-plane interaction parameter, $w_\parallel$ (cf. equation (4.30)), equals 0.6 whereas the out-of plane interaction parameter, $w_\perp$ (cf. equation(4.31)), equals 0.1. In view of the discussion given in Chapter 4.2.3.2 this indicates that the in-plane crystallite coupling is comparable to a bulk material whereas the out-of plane crystallite coupling allows relatively unconstrained crystallite deformation (note that $w_\perp = 0$ would correspond to completely unconstrained crystallite deformation). These findings are compatible with the microstructure of the layer, exhibiting a more or less columnar microstructure with grain boundaries extending from the layer-substrate interface to the surface.
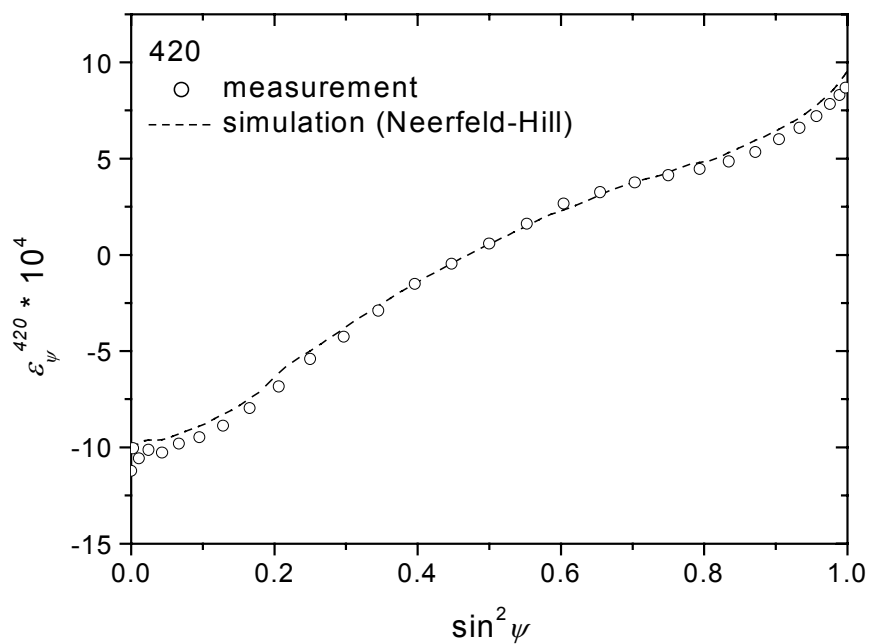
Figure 4.10: Textured copper film. Measured (open circles) and simulated (dashed line) diffraction strain data for the 420 reflection as function of $\sin^2\psi$ ($\sin^2\psi$ - plot). Clearly, the Neerfeld-Hill model is able to provide a good simulation of the $\sin^2\psi$ - plot for *only one* reflection. However, the Neerfeld-Hill model fails if multiple reflections are considered.

4.7. Conclusion

- The traditional grain-interaction models due to Voigt, Reuss, Neerfeld-Hill and Eshelby-Kröner can be inappropriate for the stress analysis in thin films by X-ray diffraction due to the assumption of isotropic grain interaction, which is not compatible with the columnar microstructures frequently observed in thin films.

- The Vook-Witt approach to grain interaction, i.e. equal in-plane strain (parallel to the substrate) and zero stress perpendicular to the film surface for all crystallites, is the first direction-dependent grain interaction taking the microstructure of a (columnar) thin film into account. The model predicts only transversely isotropic macroscopic (mechanical) properties reflecting the microstructure and thus the model can explain occurrence of curved $\sin^2\psi$-plots in the absence of texture. In analogy with the pendants formulated by Voigt and Reuss for grain interaction, for the case of transverse isotropy in this paper the inverse Vook-Witt grain-interaction model has been proposed, where all crystallites in a (thin layer) specimen can deform freely with respect to the in-plane direction, whereas they are tightly connected together with respect to the perpendicular direction.

- The traditional models of Voigt and Reuss, the recently proposed Vook-Witt model and the inverse Vook-Witt model proposed in this paper imply extreme grain-interaction assumptions. However, extreme grain-interaction assumptions are incompatible with physical reality. In this paper, an average, 'effective' grain-interaction model is proposed that consists of a linear combination of basic, extreme models with volume fractions as weighing factors. Four basic grain-interaction models have to be taken into account for surface-adjacent polycrystals as a (columnar) thin film, recognizing the occurrence of two principal directions (in-plane and perpendicular to the (film) surface) and two extremes of grain interaction (fully unconstrained (Reuss) and fully constrained (Voigt)).

- The type of grain interaction, i.e. the parameters f_i, representing the fractional contributions of the extreme grain-interaction models to the overall grain interaction, can be determined in the diffraction-stress analysis in addition to the unknown stress tensor components. It is demonstrated in this work that diffraction-stress analysis (of thin films) can best be performed by the simultaneous use of multiple reflections in a fit procedure. Fitting to only one $\sin^2\psi$-plot can lead to fortuitous, seemingly good fits that are incompatible with physical reality.

- The proposed effective grain-interaction model has been applied to experimental lattice-strain measurements of a fibre textured copper layer. The measured lattice strains, represented as $\sin^2\psi$-plots, exhibit curvature (in particular for the 111 and the 200 reflections), which is incompatible with the traditional models of grain interaction. On the basis of the effective grain-interaction model, a consistent, simultaneous analysis of several $\sin^2\psi$-plots is possible. The grain-interaction parameters used for fitting the measured $\sin^2\psi$-plots indicate that for the copper film investigated contributions of three types of grain interaction are significant: a dominating Vook-Witt ($f_{VW} = 0.6$), a distinct Reuss ($f_R = 0.3$) and a small inverse Vook-Witt ($f_{IVW} = 0.1$) type of grain interaction have been determined. These results imply that the grain interaction parallel to the surface is constrained and of mixed nature ($w_\parallel = 0.6$), whereas the grain interaction perpendicular to the surface is almost unconstrained ($w_\perp = 0.1$). This is the first time that anisotropic grain interaction has been analysed quantitatively.

5. Use of Polycapillary X-Ray Lenses in the X-Ray Diffraction Measurement of Texture

U. Welzel & M. Leoni

Abstract

Corrections for instrumental aberrations of X-ray diffraction texture measurements (pole figure measurements) conducted in quasi-parallel beam geometry using an X-ray lens have been investigated on the basis of measurements on (texture-free) reference samples.

It has been shown that a defocusing correction, which is a major correction for pole figures recorded with divergent beam geometries, is not necessary when a beam paralleled by an X-ray lens is used. In this case, the major instrumental sources of error stem from the illumination of areas outside the sample surface, i.e. the finite sample size, and the finite area of the detector, both giving rise to a reduction of the recorded signal. Two correction procedures for this reduction, an experimental one and a numerical one, have been described and tested.

5.1.Introduction

X-ray diffraction texture analysis is based on the measurement of pole figures for one or more (dependent on the texture symmetry) reflections of the sample under investigation. Diffractometers equipped with an Eulerian cradle and crossed slits for defining the size and divergence of the incident beam are the standard equipment for recording pole figures with the reflection technique (Schulz, 1949). Due to the Bragg Brentano geometry often employed in these instruments (see for example Bunge, 1982b, 1999), pole figures are severely affected by instrumental aberrations and have to be corrected before quantitative use.

A major instrumental aberration is the defocusing of the diffracted beam in a texture measurement: a broadening of the diffracted beam upon tilting the sample arises as parts of the sample move away from the focusing circle. This causes a reduction of the recorded intensity upon specimen tilting, when a fraction of the broadened diffraction profile does not pass the receiving slit. Various publications have paid attention to the correction of measured pole figures for defocusing (see, for example, Chernock & Beck, 1952, Gale & Griffiths, 1960, Holland, 1964, Tenckhoff, 1970, Holt & Winegar, 1977, Ortiz & Hermida, 1981, Lahn & Hougardy, 1999). The extent of defocusing depends on several parameters: settings of the diffractometer optics, sample contribution to the width of the diffraction line ('sample broadening'), diffraction angle, illuminated sample size and misalignments of the diffractometer. In particular, misalignments and sample size effects not taken properly into account can make the application of analytical corrections unreliable (Ortiz & Hermida, 1981, Hermida, 1982, Kurtasov *et al.*, 1983). Experimental correction methods for defocusing are based on texture-free reference samples with a line width close to that of the sample under investigation. However, the similarity of the line width of the reference and the sample under investigation can be a requirement difficult to meet.

Novel X-ray optical components, such as polycapillary collimators ('X-ray lenses') have recently been introduced (see, for instance, Kumachov & Komarov, 1990, Kogan & Bethke, 1998, Scardi *et al.*, 2000), providing higher intensity than traditional optics based on crossed slits. Further, the (quasi-) parallel beam geometry realised by means of these optics is less sensitive to sample displacements, as compared to focusing geometries and therefore instrumental aberrations are reduced. However, as the beam, when using an X-ray lens, is not perfectly parallel but exhibits a small residual divergence ('quasi-parallel beam'), aberrations are not completely eliminated (Scardi *et al.*, 2000).

An X-ray lens is composed of a large number (up to millions) of individual capillaries

(hollow fibres). When the condition for total reflection is met (i.e. the incident angle of the beam with respect to the capillary wall is below the angle for total reflection of the material composing the capillary), the capillaries guide the X-rays with a very small intensity loss by successive total reflections at the (inner) walls. Since photons with energies above a certain threshold (given by the fibre diameter and the angle for total reflection) are highly absorbed by the capillary walls as the condition for total reflection is not met, the lens acts also as an energy filter. The curvatures of the capillaries are arranged such that a fraction of the divergent beam emitted from the focus of a X-ray tube is converted to a quasi-parallel beam (see, for instance, Kumachov & Komarov, 1990, Downing *et al.*, 1996).

The application of X-ray lenses, which have now been commercially available for a few years, is not yet frequent in texture analysis. The present paper presents, on the basis of measurements performed with texture-free reference samples, an analysis of the corrections for instrumental aberrations of texture measurements (pole figures) if an X-ray lens is employed. It will be demonstrated that the defocusing (i.e. the broadening of the diffraction line, see also discussion in Chapter 5.2.) of the diffracted beam, a major problem for measurements performed in focusing geometry (e.g. Bragg-Brentano geometry), is eliminated by the quasi-parallel beam. A reduction of the measured intensity occurs in a pole-figure measurement when areas outside of the sample surface are illuminated or when only a (specimen orientation dependent) fraction of the diffracted beam is collected by the detector due to its finite size. Correction procedures for the reduction of the intensity upon specimen tilting, based on reference measurements as well as geometrical considerations, and experimental validation are presented.

5.2. Theoretical background

A pole figure $P_{2\theta_0}(\psi, \varphi)$ for a particular *hkl* reflection (identified by the Bragg angle $2\theta_0$ in the following) is a representation of the volume fraction of diffracting crystallites which have their (*hkl*) planes oriented normal to the diffraction vector as a function of angles ψ and φ, where ψ is the inclination angle of the sample surface normal with respect to the diffraction vector and φ denotes the rotation of the sample around the sample surface normal. A particular set of (*hkl*) lattice planes is selected by the choice of the diffraction angle 2θ according to Bragg's law. The integrated intensity of a *hkl* reflection is proportional to the volume fraction of crystallites (within the irradiated volume) which have their (*hkl*) planes

oriented normal to the diffraction vector. Thus, for a pole figure it is necessary to consider integrated intensities.

However, measured pole figures have to be corrected for effects, which hinder in direct interpretation of the recorded integrated intensity $P_{2\theta_0}^{meas}(\psi,\varphi)$ in terms of (orientation dependent) volume fractions (see, for instance, Bunge, 1982b, 1999):

Absorption. Because of the tilt-angle dependence of the absorption of the incident as well as of the diffracted beam along the path through the sample, an absorption factor for a (homogeneous) layer with thickness d can be given by (see, for instance, Bunge, 1982b):

$$A(d,\tau) = \tau - \tau \exp\left(-\frac{d}{\tau}\right). \tag{5.1}$$

The corresponding correction involves division of the measured intensity by A. The penetration depth τ is given by (Hauk, 1997)

$$\tau = \frac{\sin\theta\cos\psi}{2\left(\dfrac{\mu}{\rho}\right)\rho_{sample}}. \tag{5.2}$$

τ depends on the mass absorption coefficient (μ/ρ) of the material composing the sample and the (actual) density ρ_{sample} of the sample.

If the sample thickness d is much larger than the penetration depth τ, equation (5.1) becomes:

$$A(d,\tau) \xrightarrow{\quad d \gg \tau \quad} \tau. \tag{5.3}$$

Geometry of illuminated and detected areas. The illuminated area G of the sample is given by

$$G = G_0 \frac{1}{\sin\theta\cos\psi}, \tag{5.4}$$

where G_0 represents the cross-section of the incident beam. Correcting for the illuminated area involves division of the measured intensity by G.

Note that equation (5.4) holds only as long as the illuminated area remains within the sample perimeter. When a fraction of the incident beam misses the sample, equation (5.4) is no longer valid. An analogous problem arises (in the parallel beam geometry, cf. discussion below) when the irradiated sample area is larger than the area 'visible' for the detector. Then, an additional correction is necessary for the specimen orientation dependence of the diffracted

beam fraction missing the detector. The corresponding correction procedures will be discussed in detail in Chapter 5.5 Note that, in case equation (5.4) fails, G can also depend on the rotation angle φ.

Defocusing. For a parallel beam geometry, defocusing, strictly speaking, cannot occur as there is no focusing condition that could be violated. Thus, the use of parallel beam diffraction would result in a diffraction line shape independent of the actual sample tilting and rotation. However, as the beam emerging from an X-ray lens is not perfectly parallel but quasi-parallel (i.e. it exhibits a small residual divergence, see Chapter 5.4) and the diffracted beam optics accept a small divergence of the diffracted beam, the instrumental effects of tilting and rotating the sample in a texture measurement on peak shape (and position) are not obvious. These effects will be studied experimentally in Chapter 5.4.2.

Note that in parallel beam geometry, in contrast to a focusing geometry, the measurement of integrated intensities of a diffraction line is not possible if the diffraction angle, 2θ, is kept fixed (using a focusing geometry, the integrated intensity can be measured for a fixed diffraction angle 2θ by making the receiving slit large, so that the slit comprises the entire diffraction line). However, as long as the shape of the diffraction line is invariant (i.e. independent of sample tilting and rotation), the integrated intensity is proportional to the peak intensity and therefore recording the recording the intensity of a diffraction line is equivalent to the measurement of the integrated intensity.

In order to comply with the conventions used in the literature on texture analysis, a correction for an intensity loss due to a change in the width of the diffraction line (with respect to 2θ) will be referred to as defocusing correction in the following, although one could call this as well a 'geometrical correction'. If the measured intensity is reduced when areas outside of the sample surface are illuminated or when only a (specimen orientation dependent) fraction of the diffracted beam is collected by the detector due to its finite size for a measurement in (quasi-) parallel beam geometry (whereas the width of the diffraction line with respect to the 2θ scale remains unchanged), this effect will be referred to as a geometrical aberration. In the following, these two (geometrical) sources of error (i.e. fraction of the incident beam not 'hitting' the specimen and fraction of the illuminated sample area not 'seen' by the detector) will be named *instrumental intensity loss*.

Taking all corrections into account, the corrected pole figure $P_{2\theta_0}^{corr}(\psi, \varphi)$ for a given reflection can be expressed in terms of the measured pole figure $P_{2\theta_0}^{meas}(\psi, \varphi)$ by:

$$P_{2\theta_0}^{corr}(\psi,\varphi) = \frac{P_{2\theta_0}^{meas}(\psi,\varphi)}{A\left(2\theta_0,\psi,d,\left(\mu/\rho\right),\rho_{sample}\right)G(2\theta_0,\psi,\varphi)D(2\theta_0,\psi,\varphi)} \qquad (5.5)$$

where *A, G* and *D* represent the effects of absorption, geometry and defocusing, respectively. Note that $P_{2\theta_0}^{corr}(\psi,\varphi)$ is normalised to the diffracting volume.

5.3. Experimental

A set of texture-free powder samples was used. These samples were prepared by filling square or rectangular cavities cut in an aluminium disk, with tungsten powder (Merck, sample A1, area 14x14mm^2 and sample A2, area 8x22mm^2) and germanium powder (Johnson-Matthey, sample B, area 14x14mm^2). A thin layered sample (consisting, idealised, of a mono-layer of powder particles) was prepared by sedimentation of silicon powder (Ventron, sample C, area 14x14mm^2) onto a silicon wafer using ethanol as dispersing agent. The absence of texture was checked for the tungsten, the germanium and the silicon samples by a Rietveld-refinement of diffraction patterns collected with Cu Kα-radiation (for the tungsten and germanium samples) and with Co Kα-radiation (for the silicon sample) on a Philips X'Pert MPD θ-θ diffractometer in Bragg-Brentano geometry using the Rietveld-program GSAS (Larson & von Dreele, 1994). No texture effects had to be taken into account in the Rietveld-refinement, thus the refinement indicates that the samples are untextured.

Square- or rectangular-shaped samples are chosen here because correction with respect to the rotation φ of the sample around its surface normal is investigated (no such correction would be necessary for round-shaped samples). However, one of the two correction strategies presented in this paper can be applied to samples of any shape.

A Philips X'Pert MRD diffractometer equipped with an Eulerian cradle (4-circle goniometer) was used for texture measurements. Cu Kα-radiation emerging from the point focus of a sealed X-ray tube operated at 45kV and 40mA was converted into a quasi-parallel beam by a commercially available X-ray lens (Philips). The lens used in these investigations had a diameter of approximately 7mm. The size of the beam was adjustable to a square or rectangle by crossed slits placed in front of the lens (slit size was adjustable from 0mm to 10mm). Note that only if the size of both slits is smaller than the lens diameter divided by $\sqrt{2}$, the incident beam has a square- or rectangular cross section. It is recommended to use slit settings significantly smaller than the size of the lens, (e.g. 4mm x 4mm) to obtain a well-shaped beam and avoid inhomogeneous transmission properties of the lens that can occur in

the outer lens corona. The diffracted beam passed a parallel plate collimator (0.18° acceptance angle) and a flat graphite analyser (optional) before being detected by a proportional counter.

Diffraction patterns were evaluated by fitting split Pearson VII functions (for the definition of the profile function, see for instance Sonneveld *et al.* 1991). Peak positions, peak heights, half widths at half maximum (HWHM), asymmetries and shape parameters were refined. The $K\alpha_2$ component was taken into account by simultaneous fitting of two Pearson VII functions, one for each radiation component. A $K\alpha_2 : K\alpha_1$ intensity ratio of 0.5 was used (this assumption was checked by setting the ratio free as a fit parameter for some evaluations). For each diffraction peak (or group of overlapping diffraction peaks) a linear background was fitted. The span of the measurement ranges was selected as to collect a number of points sufficient for a full description of peak tails and background. The stepsize was chosen such that at least 5 data points across the full width at half maximum of the $K\alpha_1$ peak were measured. The ψ-range was 0° to 90°, the step size in ψ was 2°. Some measurements were conducted at negative ψ to ensure that the results are independent of the tilting direction.

5.4. Experimental results and discussion

5.4.1. Beam divergence and beam intensity distribution

The beam characteristics of X-ray lenses have been described from a theoretical as well as an experimental point of view in various publications (see, for instance, Kardiawarman *et al.*, 1995).

A detailed description of the intensity distribution and divergence of the beam emerging from the lens will be presented elsewhere (Leoni *et al.*, 2001); however, some main points useful for the following discussion are summarised here.
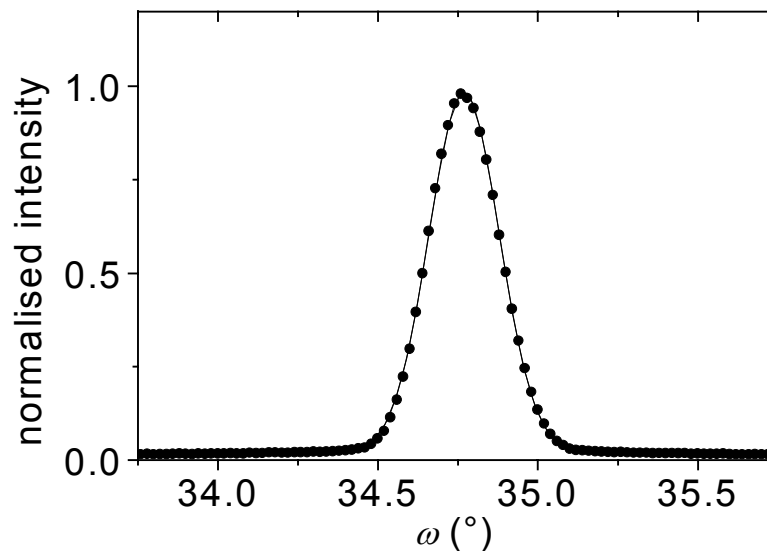
Figure 5.1: Rocking curve for the 400 reflection of a single crystalline silicon wafer (filled circles). The intensity can be described by a Gaussian distribution (line) with full width at half maximum of approximately 0.3°.

The residual divergence of the beam produced by the X-ray lens used in the present investigations was characterised by recording rocking curves from a single crystalline silicon wafer (<001> cut). A residual divergence of approximately 0.3^0 was found, as determined from the full width at half maximum of the (004)-Si-rocking curve presented in figure 5.1; note that the rocking curve was recorded without any optical components in the diffracted beam path. The homogeneity of the resulting beam was investigated by measuring the intensity of the beam as a function of the beam size (same in both vertical and horizontal direction, i.e. using a square-shaped slit aperture) by placing the detector directly in front of the crossed slits (a copper attenuator was used for reducing the intensity to a level suitable to the detector; practically identical results were obtained when a monochromator was employed or when a nickel filter for removing Cu Kβ-radiation was used): see figure 5.2. Three regions have been indicated in figure 5.2, separated by particular values of the slit aperture l_b. In region I the crossed slits aperture is positioned fully within the beam exiting the lens. The limiting case is a crossed silts aperture corresponding to the largest square that can be inscribed in the lens circumference (in this case the diagonal of the square is equal to the diameter of the lens, thus the limiting slit aperture is $l_I = \frac{1}{\sqrt{2}}D = 4.95mm$, D being the lens diameter).
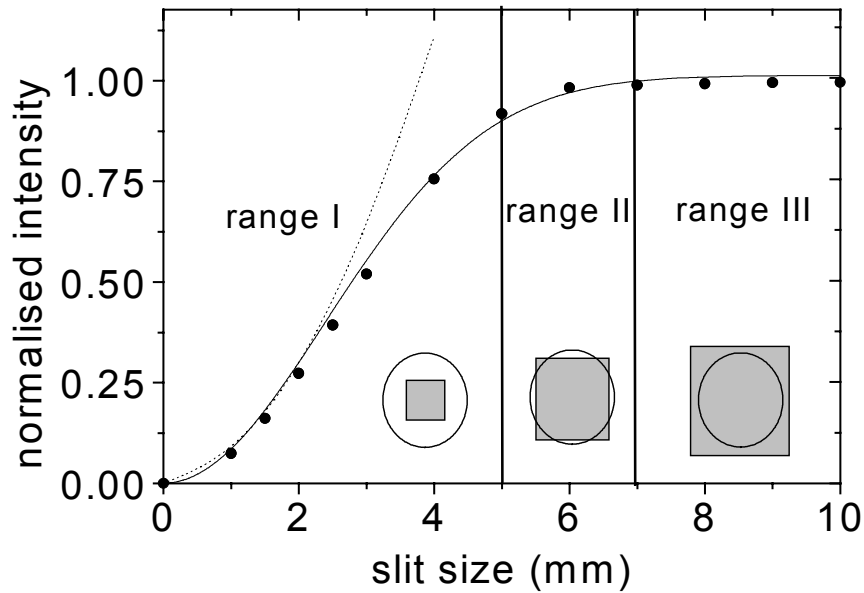
118

Figure 5.2: Beam intensity versus beam size as set by the slits (filled circles). The intensity behaviour can be described by a Gaussian distribution (solid line). A parabola can only be fitted for small lens apertures (dotted line).

In region II the beam extension is determined by both the slits and the lens whereas in region III the extension is determined only by the lens. The slit size for the transition from region II to region III is $l_{II} = D$ (provided the centres of gravity of lens and slit apertures coincide).

Plotting the intensity in region I as a function of the slit size should yield a parabola in the case of a homogeneous transmission. For small slit apertures ($l<3$mm) such a parabola fit is possible indeed, but this fit does not represent the observed intensity for slit sizes $l>3$mm (which are still within range I, see figure 5.2). It is concluded that the lens transmission is not homogeneous, the outer lens corona transmitting relatively less intensity. This can be understood, recognising that a ray passing through the centre of a lens can be transmitted without being reflected at the fibre walls whereas a ray propagating in an outer lens corona suffers an intensity loss from a number of total reflections at the walls (note that, as every material exhibits absorption, for a total reflection at an incidence angle larger than zero, a small loss of intensity occurs due to absorption).

A good (empirical) approximation, comprising regions I, II and III is possible by a Gaussian curve:

$$I = I_0 \left(1 - \exp\left(-\frac{l_b^2}{l_0^{\,2}} \right) \right) \tag{5.6}$$

where I_0 indicates the maximum intensity and l_0 is the slit size where about 63% of the maximum intensity passes the slits.

5.4.2. Instrumental effects in texture measurements

For a (hypothetical) pole-figure measurement without instrumental aberrations, the integrated intensity of a diffraction peak of a thick, texture-free powder sample should be independent of the sample orientation φ (rotation) and ψ (tilting). Thus, any orientation dependence of the peak shape or the peak intensity observed in a measurement from a texture-free specimen hints at the necessity for corrections to be performed in pole-figure measurements using an X-ray lens (cf. Chapter 5.2. '*Defocusing*').

Peak shape

For investigating the influence of instrumental effects on peak shape associated with tilting and rotating the sample, diffraction lines of (texture-free) reference powder samples (cf. Chapter 5.3) were recorded at various Bragg-, sample tilt- and rotation angles: 2θ: 28°...155°, ψ: -90°...+90°, φ: 0°...360°). Results for the tungsten sample (thick layer, sample A1) at relatively low (110-reflection, $2\theta \approx 40°$) and high Bragg angle (321-reflection, $2\theta \approx 130°$) are shown in figures 5.3 and 5.4. Figure 5.3 presents the diffraction line width (half width at half maximum, HWHM), the diffraction line shape parameter η and the diffraction line asymmetry α as a function of the sample tilt ψ (Pearson VII fits).
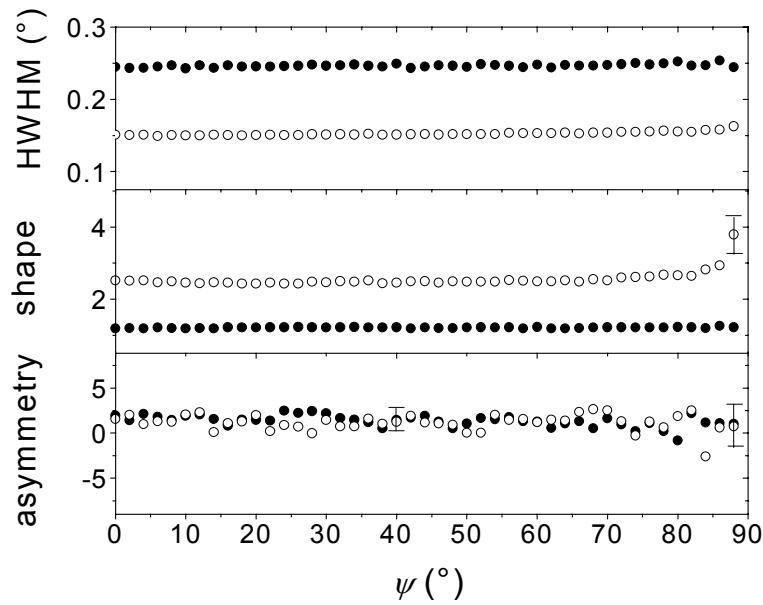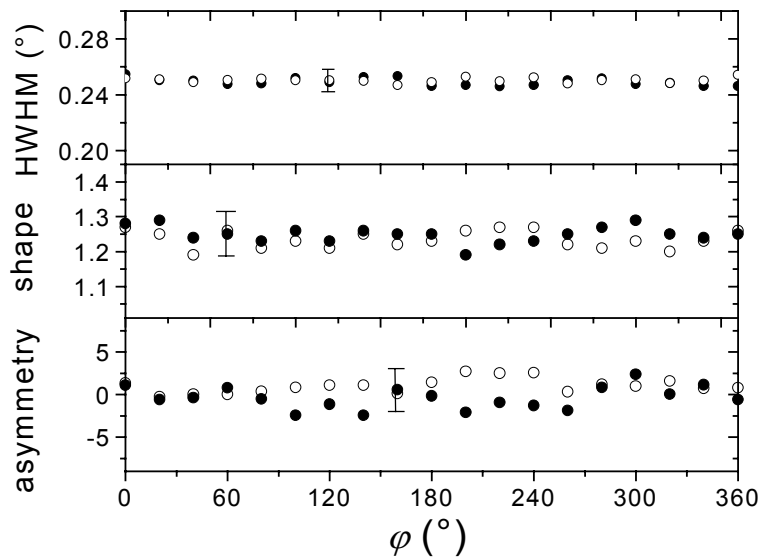
Figure 5.3: Peak parameters obtained from reflections of a thick tungsten powder layer (sample A1): half width at half maximum, shape parameter η and asymmetry α of the tungsten 110- and 321-reflections versus the sample tilt angle ψ (open and filled circles, respectively).

Figure 5.4: Peak parameters obtained from reflections of a thick tungsten powder layer (sample A1): half width at half maximum, shape parameter η and asymmetry α of the tungsten 110 reflection versus the sample rotation angle φ for two different tilt angles ψ, 0° (open circles) and 80° (filled circles).

Figure 5.4 shows results for the same parameters as recorded for the tungsten 321-reflection as a function of the rotation angle φ for two different values of ψ-tilt, 0° and 80°. Evidently, these parameters are practically independent of ψ and φ. Only a slight increase of the shape parameter η occurs for the 110-reflection of tungsten at high angles, $\psi > 84°$. However, the ratio of the integrated and the peak intensity does not change significantly, thus, recording the peak intensity is still equivalent to evaluating the integrated intensity from the whole diffraction peak. It is not necessary to account for an instrumental shift in peak position. Although a stable peak position cannot be guaranteed at high tilt angles, the observed shifts need not be considered for texture analysis as they are too small to influence the measured intensity significantly (see also Scardi *et al.*, 2000).

There is thus no need for applying a defocusing correction when an X-ray lens is used. In the following, integrated intensities extracted from the whole diffraction line profiles have been used in all figures; as a distinction between peak and integrated intensities is not necessary, the term 'intensity' will be used in the following for brevity.

Peak intensity

Experimental examples are shown in figures 5.5a and 5.5b. The intensity of the 321-reflection of a (thick) tungsten powder layer (sample A1) is presented in figure 5.5a as a function of the sample tilt angle ψ, the intensity of the 400-reflection of a thin silicon layer (sample C, this layer cannot be considered as infinitely thick) is shown in figure 5.5b.

For the thick layer (sample A1) it holds that, at low ψ (up to about 60°), the intensity increase due to increase of illuminated sample area is compensated exactly by the decrease of diffracted intensity due to absorption: the recorded intensity is independent of ψ (figure 5.5a). The intensity decrease at higher angle of tilt is due to instrumental intensity loss. For the thin layer (sample C), the intensity decrease due to absorption is overcompensated by the increase in intensity due to increase in illuminated area upon tilting and therefore the intensity increases up to about 60°. The intensity decrease upon further tilting is due to instrumental intensity loss (figure 5.5b).

The extent of instrumental intensity loss depends not only on the angle of sample tilt but also on the Bragg angle of the reflection considered. The intensity as function of tilt angle ψ for tungsten (sample A1) at low (110-reflection, $2\theta \approx 40°$) and high (321-reflection, $2\theta \approx 131°$) Bragg angle is shown in figure 5.6a. It follows that the extent of the instrumental intensity loss decreases with increasing Bragg angle.
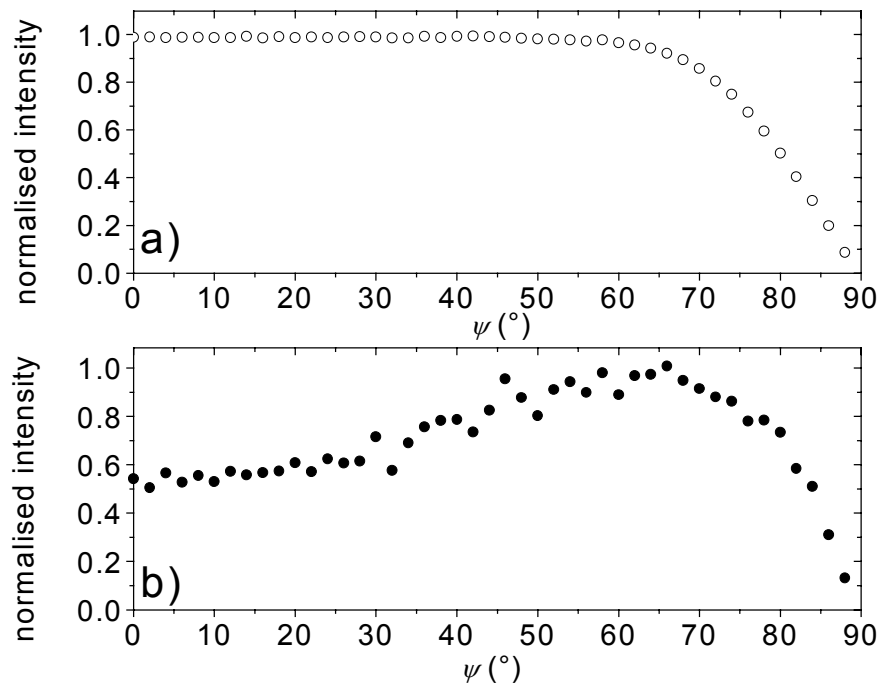
Figure 5.5: Intensity of the 321-reflection of a (thick) tungsten powder layer (a) (sample A1) and intensity of the 400-reflection of a thin silicon layer (b) (sample C) versus the sample tilt angle ψ.

The instrumental intensity loss upon tilting depends also on the ratio of the diameter of the incident beam and the surface area of the sample: see figure 5.6b. The smaller this ratio the lesser the instrumental intensity loss.

The integrated intensity does not depend on the angle of rotation, φ, for a round-shaped sample. However, for a square- or rectangular-shaped sample an effect of specimen rotation on the recorded intensity can be observed (if instrumental intensity loss occurs). As an example, the φ-dependence of the peak intensity of the W 110-reflection of two tungsten samples (sample A1 and A2) is presented for a tilt angle ψ of 60° in figure 5.7. For the square sample (A1) only a shallow modulation of the intensity is observed whereas for the rectangular sample (A2) the modulation is much more pronounced.
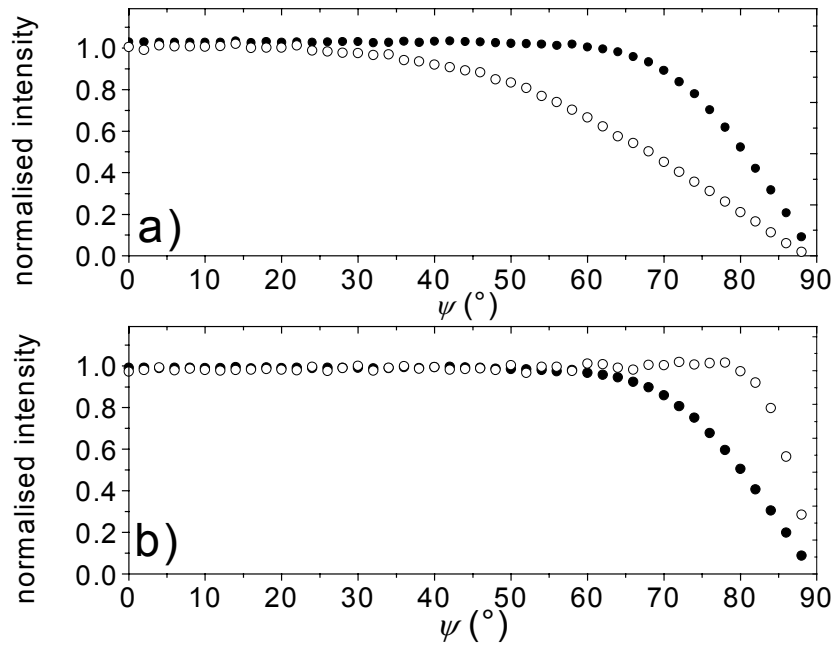
Figure 5.6: (a) Intensity of the tungsten 110- ($2\theta \approx 40°$, open circles) and 321-reflections ($2\theta \approx 130°$, filled circles) of a thick powder layer (sample A1) versus the sample tilt angle ψ. (b) Intensity of the tungsten 321-reflection ($2\theta \approx 130°$) of a thick powder layer (sample A1) versus the sample tilt angle ψ for two sizes of the incident beam, 1x1mm^2 and 4x4mm^2 (open circles and filled circles, respectively).
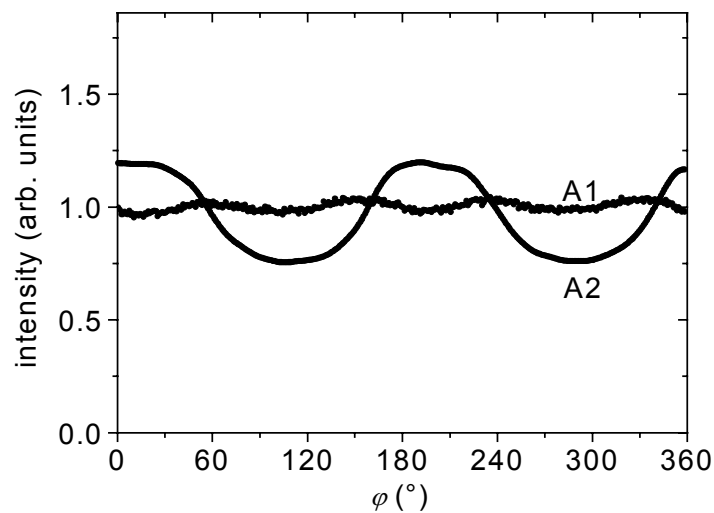
Figure 5.7: Intensities of the 110-reflections of two (thick) tungsten powder layers (samples A1, 14x14mm^2 and A2, 8x22mm^2) versus the sample rotation angle φ for ψ=60°.

In summary, from the results shown in this section it can be concluded that the only instrumental effect, for which a correction is necessary, is the geometrically conditioned instrumental intensity loss occurring upon tilting and/or rotating the sample.

Note that even though the peak intensity of a diffraction line is equivalent to the integrated intensity, weak reflections must be counted for an appropriate time to reduce the associated statistical error.

5.5. Full correction of pole figure intensities

Analytical corrections for the effect of instrumental intensity loss in the case that an X-ray lens is used are not available in the literature. In the following an experimental approach for the correction of the instrumental intensity loss is presented. The method is based on measurements on texture-free samples, valid for all sample and beam geometries. On the basis of geometrical considerations the required number of such measurements can be reduced if only tilting-dependent effects have to be corrected (e.g. in the case of fibre texture or for square shaped samples, when the modulation of the intensity in a φ-rotation is marginal): in this case a numerical calculation of the correction factor, calibrated by only one measurement on a texture-free reference sample is possible.

5.5.1. Experimental method

To establish the correction factor for instrumental intensity loss by measurement from a texture-free reference sample, it is required that the size and the shape of the reference sample and the sample under investigation are identical. Moreover, an identical positioning of the reference and the sample under investigation in the diffractometer must be guaranteed. To this end, the positioning of the reference and the sample under investigation should be performed with an accuracy of 5% for a shift within the plane of the sample. For the sample height ('displacement'), a displacement of ±100μm from the ideal position is acceptable (in this case, no significant deviations of measured intensities were observed in test measurements). This reproducibility is achievable under practical conditions. It is *not* required that the material of the reference sample is the same as that of the sample under investigation. The widths of the diffraction peaks may also be different.

The correction is first presented for the effect of tilt angle ψ only; the effect of rotation (φ) is considered afterwards. The determination of the correction factor $C(2\theta_i,\psi)$ for changes

in illuminated sample area and instrumental intensity loss runs as follows:

Determination of the Correction Factor for illuminated sample area and instrumental intensity loss

(i)   Measurement of the intensity $I_{2\theta_i}^{meas}(\psi)$ for various reflections (characterised by the Bragg angles $2\theta_i$) of a thick reference (i.e. texture-free) sample as a function of ψ.

(ii)   Correction of $I_{2\theta_i}^{meas}(\psi)$ for the tilting angle dependence of absorption (factors being constant for a particular sample and reflection are ignored, as, in the next step (iii), a normalisation is performed, cf. equation (5.2) and (5.3)):

$$I_{2\theta_i}^{corrabs}(\psi) = \frac{I_{2\theta_i}^{meas}(\psi)}{\cos\psi}.$$

(iii)   Normalisation of the intensities for every reflection such that

$$I_{2\theta_i}^{corrabs}(\psi = 0) \equiv 1.$$

(iv) $C(2\theta_i,\psi) = 1/I_{2\theta_i}^{corrabs}(\psi)$ is the correction factor for changes in illuminated sample area and instrumental intensity loss.

Then, full correction of the pole figure intensities $P_{2\theta_S}(\psi)$ of a particular reflection of the sample to be investigated (characterised by the Bragg angle $2\theta_S$), i.e. the correction for absorption, changes in illuminated sample area and instrumental intensity loss, is achieved as follows (cf. equation (5.5)):

Full correction of pole figure intensities using the correction factor $C(2\theta_i,\psi)$

(i)   Absorption correction by division of the measured intensity by A according to equation (5.1) (general case) or equation (5.3) (thick sample).

(ii)   Multiplication of the intensity as obtained by the previous step (i) by $C(2\theta_S,\psi)$.

(iii)   Division of the intensity as obtained by the previous step (ii) by $G_0 / \sin\theta_S$ (G_0 being the cross-section of the incident beam) results in a normalisation to the diffracting volume, such that the obtained intensity corresponds to $P_{2\theta_S}^{corr}(\psi)$ in equation (5.5).

For performing the correction, only the mass coverage and the mass absorption coefficient of the sample under investigation must be known: as the ratio of the sample thickness and the penetration depth (i.e. the argument of the exponential function in equation (5.1)) contains the mass coverage $d\rho_{sample}$ times the mass absorption coefficient as individual factors, thickness and density of the layer are not needed as individual quantities for the absorption correction and the knowledge of the mass coverage is sufficient.

The correction factor $C(2\theta, \psi)$ can only be determined experimentally for Bragg angles ($2\theta_i$) where peaks of the reference are available. After normalisation of the intensities of the reference specimen as a function of ψ (step (iii) in the determination of the correction factor, see above), a smooth 2θ -dependence for $C(2\theta_i, \psi)$ for a given tilting ψ is observed. Therefore a spline-interpolation *on the 2θ-scale* is a sufficiently accurate method for the determination of $C(2\theta, \psi)$ at a Bragg angle where no reference peak is available. Here a cubic spline interpolation routine (from the IMSL Fortran Math-library v1.0, © 1987 by IMSL, Inc.) was applied.

The performance of the experimental method was tested as follows:

- The correction factor $C(2\theta, \psi)$ for changes in illuminated sample area and instrumental intensity loss was determined using eight reflections (i.e. all reflections accessible with CuKα radiation) of the tungsten powder layer (sample A1) as a reference.

- Then, the full correction (absorption + illuminated area + instrumental intensity loss) was applied to the intensities of reflections recorded from a *thick* Ge powder sample (sample B) as function of tilt angle ψ. The corrected intensity for each reflection as function of ψ should then be independent of ψ. This expectation was met by the results: see figure 5.8.

- The full correction was also applied to the integrated intensities of reflections of a *thin* Si powder sample, see figure 5.9. The mass coverage (mass per unit area, here: 9.4 μg /mm^2) was calculated from the mass of the silicon powder dispersed and the covered area. Also in this case an almost ψ-independent intensity is observed after correction.

It can be deduced from the figures 5.8 and 5.9 that (especially at low Bragg angle) the correction of the experimental intensities for instrumental intensity loss is a prerequisite for quantitative texture analysis. If the correction is applied, as a rule, the tilt angle range can be extended up to about 86^0, independently of the Bragg angle for the reflection used for pole-figure measurement.
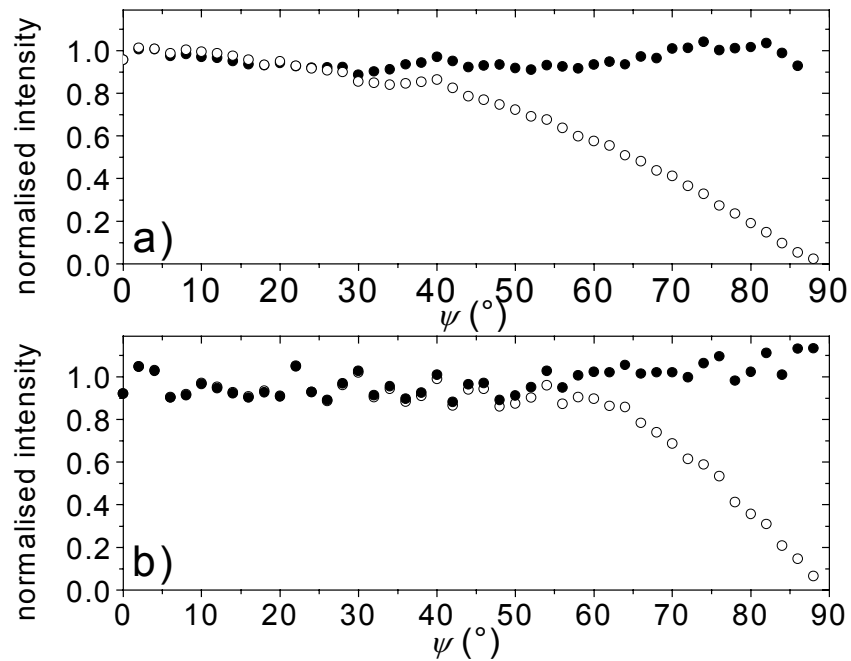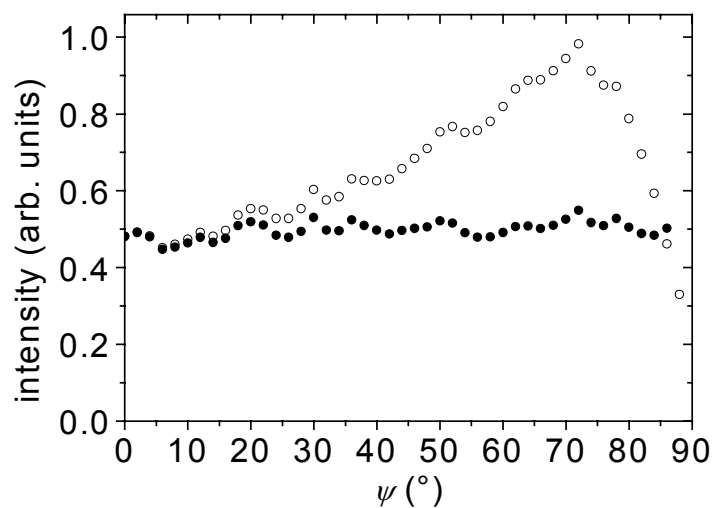
127

Figure 5.8: Full (experimental) correction of measured intensities: Measured (open circles) and corrected (filled circles) intensities versus the sample tilt ψ for two reflections, 111 and 440, of a thick germanium sample (sample B).

Figure 5.9: Full (experimental) correction of measured intensities: Measured (open circles) and corrected (filled circles) intensities versus the sample tilt ψ for the 440-reflection of a thin silicon sample (sample C).

The effect of rotation by the angle φ can be taken into account in the correction procedure as follows: The intensity of a particular reflection of the reference sample has to be measured not only as a function of the tilt angle ψ but now also as a function of the rotation angle φ. For regularly shaped samples the full range of 0° to 360° for φ has not to be considered: the measurement time can be reduced by symmetry considerations. Consider, for example, a square shaped samples: the intensity for a φ-rotation at a given ψ tilt exhibits four-fold symmetry and thus only one quarter of the complete φ–rotation angle range has to be covered. The intensity $I_{2\theta_0}^{meas}(\psi,\varphi)$ of the reference specimen for a particular reflection which has to be determined thus pertains to one quadrant of a pole figure.

A further reduction in measurement time for the standard can be gained by considering that the φ-dependence of the intensity of the standard (see figure 5.7) is smooth for regular sample shapes, thus a spline-interpolation for the φ-dependence of the correction factor also reduces the number of φ-values for which measurements are necessary. The same analysis as outlined above can be applied to the integrated intensity measured as a function of ψ and φ for a particular reflection of the sample under investigation.
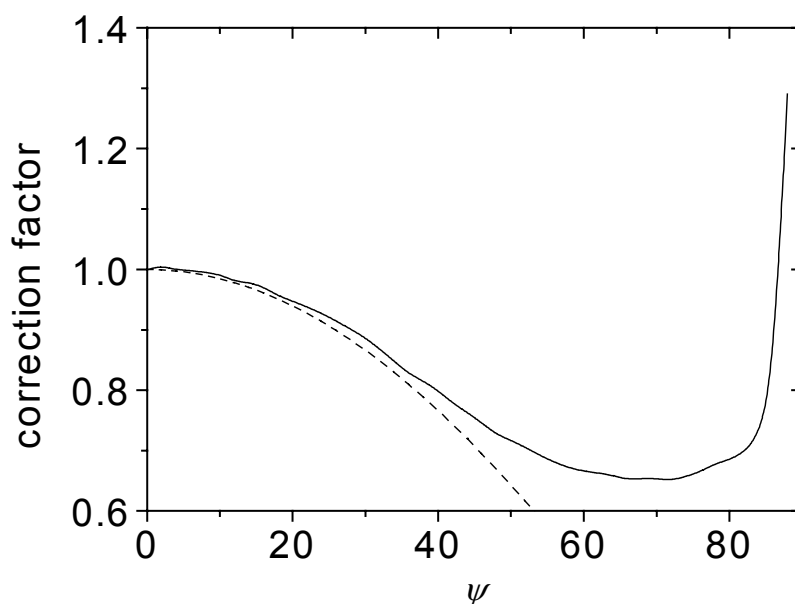

Figure 5.10: Correction factor for illuminated sample area and instrumental intensity loss for a diffraction angle $2\theta=60°$ (continuous line). The calculation of the correction factor is based on standard measurements for 8 reflections of the tungsten standard sample A1. In addition, $\cos(\psi)$ is shown by the broken line.

As a concluding remark it is noted that, at high tilt (ψ>80°), the correction factor $C(2\theta,\psi)$ increases quite steeply with ψ; see figure 5.10 for an example. For proper correction, special care has to be taken to ensure that the standard specimen and the specimen under investigation is well aligned, i.e. the mounting is identical with respect to the tilt angle ψ.

5.5.2. Geometrical considerations and numerical method

A numerical calculation of the instrumental intensity loss can, in principle, be carried out straightforwardly. To this end, the specimen orientation dependence of the fraction of the incident beam missing the sample and the specimen orientation dependence of the illuminated area not visible for the detector have to be calculated. However, due to beam imperfections, e.g. inhomogeneous lens transmission and residual divergence, and a rather complex transmission of the diffracted beam optics (e.g. mosaic spread of the monochromator) a calculation of the instrumental intensity loss (taking all beam imperfections and instrumental details into account) is complex (but possible, see Leoni *et al.* 2001). In the following, the simplest geometrical approach will be presented, based on the following assumptions:

- The cross section of the incident beam has a square shape.

- The sample has a square shape.

- The instrumental intensity loss is solely due to a fraction of the incident beam missing the sample surface, i.e., no correction for the (specimen orientation dependence of the) diffracted beam fraction missing the detector is applied. This constraint can be met in practice by a proper selection of the sample size, i.e. smaller than the acceptance of the optical modules in the diffracted beam path. The monochromator used is the limiting optical module for the equatorial size of the diffracted beam: the acceptance is approximately 9mm in the equatorial plane with a monochromator and 14mm without the monochromator. For this reason, the monochromator was removed from the diffracted beam path for measurements used for testing the numerical method with square shaped samples of the size 14x14mm^2. [3]

The calculation of the correction factor is performed as follows (for mathematical details see

---

[3] Note that even without the monochromator mounted in the diffracted beam path, a small specimen orientation dependent intensity loss can occur in the diffracted beam path for a sample size of 14x14mm^2. However, the loss of intensity is small and is not considered in the following for this reason. Equivalent results are obtained with smaller samples.

Appendix 5):

(i) A laboratory reference frame with the origin at the centre of the goniometer is defined such that the x-axis points towards the source of the incident X-ray beam (lens centre), the y-axis is aligned parallel to the inverse surface normal of the sample for $\theta=\psi=0$ and the z-axis is parallel to the $\theta/2\theta-$ rotation axis. With respect to this reference frame, the corners of the square sample can be indicated by four vectors. When the sample is in the position $\theta=0$, $\varphi=0$, $\psi=0$, the components of the vectors can be readily determined as the y-components are zero.

(ii) Any (rotational) positioning of the sample is defined by values for the three rotation angles φ, ψ and θ. The vectors for the corners of the sample in a rotated position (φ, ψ, θ) can be found by multiplying the initial vectors corresponding to the sample position ($\theta=0$, $\varphi=0$, $\psi=0$) by suitable rotation matrices (see appendix for the definition of the rotation matrices).

(iii) The projection of the corners of the sample onto the y-z-plane (i.e. the plane perpendicular to the propagation direction of the incident beam) is obtained by setting the x-component of the vectors for the corners equal to zero. When the y- and z-components are considered as vectors in a (two-dimensional) y-z-reference frame, they define the sample surface as it is seen along the direction of the incident beam, i.e. the area of the projection of the sample surface.

(iv) The area of the projection of the sample surface covered by the incident beam can then be determined by numerical integration as a function of ψ tilt and φ–rotation. This calculated area (as a function of ψ and φ) can be used instead of the measured intensity of a thick reference sample and the correction can be performed analogous to the procedure outlined in Chapter 5.5.1.

In the above calculation procedure a perfectly parallel and homogeneous incident beam has been assumed. The use of a beam with these characteristics is not possible in practice by employing an X-ray lens: residual divergence as well as inhomogeneous lens transmission occur (cf. Chapter 5.4.1). An approximate procedure for considering beam divergence (neglecting any changes of the cross section of the beam due to divergence) is possible as follows: Due to divergence the beam size at the sample position l_b^s, i.e. the edge length of the square-shaped beam, is larger than the size l_b as defined by the slit settings (i.e. the aperture size at the lens exit).
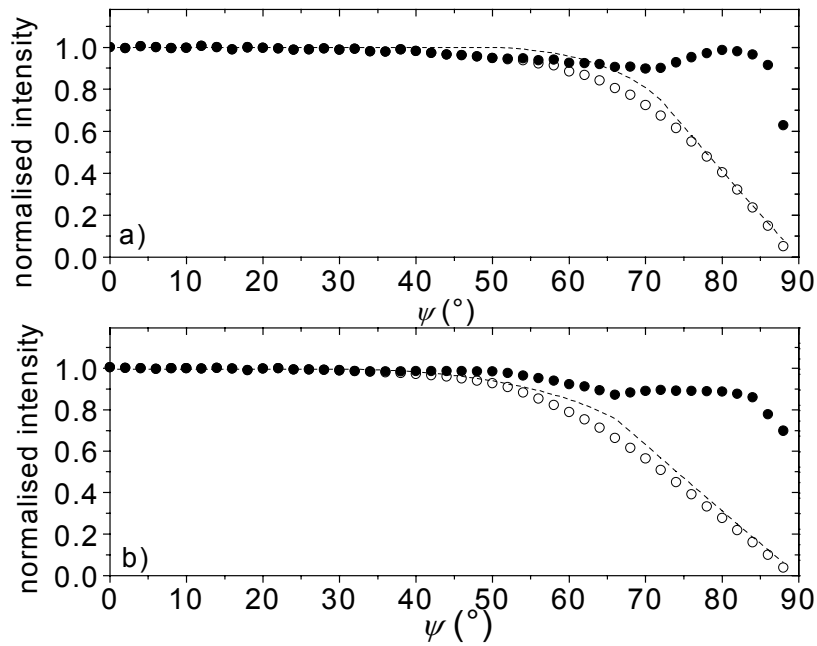
Figure 5.11: Full (numerical) correction of measured intensities: Measured (open circles) and corrected (filled circles) intensity of the tungsten 211-reflection of a thick powder layer (sample A1) versus the sample tilt ψ, measured without a monochromator (a) and with a monochromator (b). Calculated intensity following the correction scheme presented in section 5.2 is shown as dashed lines.
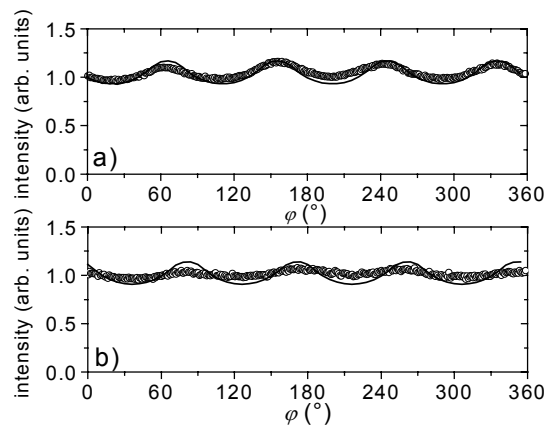

Figure 5.12: Measured (circles) and calculated (lines) intensity of the tungsten 110-reflection (a) and the tungsten 211-reflection (b) of a thick powder layer (sample A1) versus the sample rotation angle φ at a tilt angle ψ=80°.

The increase in beam size can be described by a factor κ as $l_b^s = \kappa \cdot l_b$. The correction procedure can be followed as outlined above (steps 1 to 4) by replacing the beam size as set by the slits at the lens exit l_b by the increased beam size l_b^s.

For the practical application of the correction, the factor κ can be determined as follows: For a measurement of the tilting angle dependence of the intensity of a (texture-free) reference sample for one particular reflection, κ has to be fitted such that the calculated tilting dependence of the intensity equals the measured dependence for this reference measurement. This fitting is necessary, as the divergence angle of the incident beam, as measured by the FWHM of a rocking curve, cannot be used straightforwardly for the calculation of κ (note that the divergence has a distribution, the divergence angle being the width of this distribution (cf. Chapter 5.4.1)). In addition, other instrumental effects not taken into consideration so far, as for example the beam inhomogeneity, can be satisfactorily corrected for by determining a proper value κ, i.e. other beam imperfections can also be covered (empirically) by this simple treatment.

Results for the tilt-(ψ)-dependence of the intensity for the 211 reflection of tungsten (sample A1) are presented in figure 5.11a where the measured intensity is shown together with the intensity calculated as outlined above and the corrected intensity. The beam area set by the slits was 4x4mm^2 and the sample area was 14x14mm^2. Divergence was taken into account by using a corrected beam area of 4.4x4.4mm^2 (i.e. κ=1.1) as determined by the fit of the calculated normalised intensity to the measured one. Also an instrumental intensity loss in the diffracted beam path can be modelled (empirically) by the correction: see figure 5.11b, where the experimental results for the tilt-(ψ)-dependence of the intensity for the 211 reflection of tungsten (sample A1) measured with a monochromator[4] in the diffracted beam path can be compared with the calculated and the corrected intensity evaluated using a beam area of 5.6x5.6mm^2 instead of 4x4mm^2 (i.e. κ=1.4). κ was determined by the fit of the calculated normalised intensity to the measured intensity for the 222 reflection (not shown). Note that κ determined in this way provides a reasonable correction not only for the

---

[4] Insertion of the monochromator causes significant intensity loss in the diffracted beam path, as can be seen by comparing the experimental results in figure 11a and 11b: for the data shown in figure 11b, the intensity decrease due to instrumental intensity loss occurs at lower tilt angle and is more pronounced as compared to the data presented in figure 11a.

particular reflection employed for the determination of κ but also for other reflections, thus the measurement of the tilt angle dependence for one reflection is sufficient to establish the correction. It can be concluded that the simple geometrical procedure proposed provides a reasonable estimation of the tilting angle-dependent instrumental intensity loss and thus of a correction factor. However, due to the simplifying assumptions employed, some unphysical oscillations can occur in the corrected intensity (see figure 5.11a,b).

The quantitative evaluation of the rotation-(φ)-dependence of the intensity shows qualitative agreement with the experimental results, however, the calculation slightly overestimates the amplitude of the intensity modulation: see figure 5.12, showing calculated and experimental data for the 110 and the 211 reflection of tungsten (sample A1, measurement without monochromator). One reason for the observed discrepancy is that beam divergence causes a rounding of the ideally square-shaped profile of the incident beam; the amplitude of the intensity modulation is therefore lower than expected from the calculation where a truly square-shaped beam is assumed. In addition, the outer portions of the irradiated sample area contribute less to the diffracted signal than the centre, as the lens transmission is inhomogeneous (i.e. reduced within the outer lens corona). It should be noted that a correction for the φ-dependence of instrumental intensity loss is not required for many practical applications as their effect can be of minor importance as compared to the ψ-dependence of instrumental intensity loss.

From the performance of the numerical method as shown above (see figure 5.11, correction of the tilting dependence of the intensity, and figure 5.12, slight overestimation of the intensity modulation amplitude), the limitations of a simple geometrical approach approximating details of the beam imperfections become obvious. The (fully) experimental correction discussed in Chapter 5.5.1 is certainly more rigorous but also more tedious. An alternative correction procedure not relying on measurement from texture free standard samples, taking all beam imperfections and instrumental details fully into account, is a ray-tracing of the diffractometer optics. Details on this approach will be presented elsewhere (Leoni *et al.*, 2001).

5.6. Conclusions

1. If an X-ray lens is used in X-ray diffraction texture analysis no defocusing correction is necessary as a result of the parallel beam geometry. Thus, measuring the (peak) intensity of a diffraction line is equivalent to the measurement of the integrated intensity in a pole figure measurement.

2. The effects of absorption and the geometry of illuminated and detected areas on the intensity as function of specimen tilt and rotation, as presented in measured pole figures, have to be corrected. The geometry effects include the obvious intensity increase due to the increase of illuminated sample area upon tilting, and intensity loss due to a part of the incident beam not "hitting" the specimen and a part of the diffracted beam not recorded by the detector.

3. An experimental correction procedure for the geometric effects has been proposed. The method is based on measurements for various reflections from texture-free reference powder specimens. The reference powder can be different from the material of the sample under investigation. The reference measurements have to be performed only once for a given sample shape and beam size. The procedure can be applied to correct intensities recorded as a function both of the sample tilt and the specimen rotation.

4. A numerical correction for the geometric effects has been proposed as well. This method is suitable for applications where the instrumental intensity is φ-independent (e.g. round-shaped samples) or where the φ-dependence is marginal. This procedure can incorporate the effects of beam divergence and beam inhomogeneity by fitting to one reference measurement.

Appendix 5. Rotation matrices used in the numerical method

For the particular choice of the laboratory reference frame (see main text), the rotations are best applied in the order φ-rotation, ψ-rotation and θ- rotation. Then the rotation axes remain stationary, i.e. their relation to the reference axes is the same for each calculation step, because for each calculation step, i.e. for each tilt or rotation angle, the sample is rotated *starting from* the position $\theta = 0$, $\varphi = 0$, $\psi = 0$). The rotation axis for the φ-rotation is the y-axis, the corresponding rotation matrix D_φ is:

$$D_\varphi = \begin{pmatrix} \cos\varphi & 0 & \sin\varphi \\ 0 & 1 & 0 \\ -\sin\varphi & 0 & \cos\varphi \end{pmatrix}.$$

(5A1)

The second rotation, ψ, has to be performed around the x-axis, the corresponding rotation matrix D_ψ is:

$$D_\psi = \begin{pmatrix} 1 & 0 & 0 \\ 0 & \cos\psi & \sin\psi \\ 0 & -\sin\psi & \cos\psi \end{pmatrix}.$$

(5A2)

The last rotation, rotating around the $\theta/2\theta$–axis, is described by the rotation matrix D_θ:

$$D_\theta = \begin{pmatrix} \cos\theta & -\sin\theta & 0 \\ \sin\theta & \cos\theta & 0 \\ 0 & 0 & 1 \end{pmatrix}.$$

(5A3)

The matrices have to be applied to the vectors $\overline{c}_i$ of the four sample corners, which can be readily given when the sample is in the position $\theta = 0$, $\varphi = 0$, $\psi = 0$:

$$\overline{c}_1 = \frac{l}{2}\begin{pmatrix} 1 \\ 0 \\ 1 \end{pmatrix}, \; \overline{c}_2 = \frac{l}{2}\begin{pmatrix} 1 \\ 0 \\ -1 \end{pmatrix}, \overline{c}_3 = \frac{l}{2}\begin{pmatrix} -1 \\ 0 \\ -1 \end{pmatrix} \text{ and } \overline{c}_4 = \frac{l}{2}\begin{pmatrix} -1 \\ 0 \\ 1 \end{pmatrix},$$

(5A4)

where l is the length of one edge of the sample (assuming a square shape).

6. Kurzfassung der Dissertation in deutscher Sprache

6. 1. Einleitung und Überblick

Dünne Schichten, hergestellt durch Abscheidung auf einem Substrat oder durch einen Prozeß (wie z.B. Plasmanitrieren) an einer Oberfläche, sind von großer technologischer Bedeutung, z.B. als Schutzschichten oder in der Mikroelektronik. Zahlreiche Faktoren, wie z.B. die Adhäsion einer abgeschiedenen Schicht auf ihrem Substrat, beeinflussen die Eigenschaften und insbesondere die Zuverlässigkeit von Schichten und Schichtsystemen. Einen der wohl wichtigsten Faktoren stellt der Eigenspannungszustand dar (siehe z.B. Machlin, 1995).

Um ein grundlegendes Verständnis für die Korrelation von Mikrostruktur, Eigenspannungszustand und weiteren (z.B. elektrischen oder magnetischen) Eigenschaften des Schichtsystems zu entwickeln, bedarf es insbesondere auch der Meßverfahren zur quantitativen Analyse von Eigenspannungszuständen.

Röntgenbeugungsmessungen stellen für kristalline Proben eine Möglichkeit zur Analyse von Eigen- (und Last-) Spannungszuständen dar (siehe z.B. Noyan und Cohen, 1987, Hauk, 1997). Es ist ein Vorteil dieser Methode, daß neben der Messung von Gitterdehnungen zur Spannungsanalyse auch gleichzeitig weitere Informationen über die untersuchte Probe erhalten werden können. So können Aussagen über die kristallografische Textur aus der (integralen) Intensität der Röntgenbeugungslinien und die Defektstruktur (z.B. Größe von Kristalliten, Verseztungsdichten) aus der Verbreiterung der Röntgenbeugungslinien erhalten werden. Überdies ist die Methode zerstörungsfrei.

Die vorliegende Arbeit ist der Analyse von Eigenspannungszuständen polykristalliner Proben mit Hilfe von Röntgenbeugungsmessungen gewidmet. Der Schwerpunkt liegt dabei auf der Modellierung der elastischen Kornwechselwirkung in dünnen, oberflächennahen Schichten.

Die Grundlage jeder röntgenografischen Spannungsanalyse ist die Messung von Gitterdehnungen unter der Verwendung einer oder mehrerer Röntgenbeugungslinien in Abhängigkeit von zwei Winkeln ψ und φ, wobei ψ den Verkippungswinkel des Beugungsvektors bezüglich der Oberflächennormalen der Probe und φ den Drehwinkel um die Oberflächennormale der Probe bezeichnet. Aus den gemessenen Gitterdehnungen können die Komponenten des mechanischen Spannungstensors in einem bezüglich der Probe fixierten

Koordinatensystem unter Verwendung von geeigneten, sogenannten röntgenelastischen Konstanten ermittelt werden (siehe z.B. Noyan & Cohen, 1987, Hauk, 1997).

Die Bestimmung dieser elastischen Konstanten (ebenso wie der mechanischen elastischen Konstanten) aus den einkristallelastischen Konstanten des Probenmaterials ist nicht ohne zusätzliche Annahmen möglich, falls die einzelnen Kristallite, aus denen der Vielkristall zusammengesetzt ist, elastisch anisotrop sind. In diesem Fall sind die Dehnungs- und Spannungszustände für die unterschiedlich orientierten Kristallite im Vielkristall voneinander und von dem Dehnungs- und Spannungszustand des Vielkristalls verschieden. In sogenannten Kornwechselwirkungsmodellen werden Annahmen über die Verteilung von Dehnungen und Spannungen für die verschieden orientierten Kristallite getroffen und somit wird auch die Berechnung von röntgenelastischen und mechanischen elastischen Konstanten ermöglicht. In der Regel werden die Kornwechselwirkungsmodelle nach Voigt (1910), Reuss (1929), Neerfeld-Hill (Neerfeld, 1942 und Hill, 1952) und Eshelby-Kröner (Eshelby, 1957, Kröner, 1958, siehe auch Kneer, 1965) verwendet. Diese Modelle werden, obwohl nicht ursprünglich dafür konzipiert, auch auf dünne Schichten angewendet.

Aufgrund ihres quasi-zweidimensionalen Aufbaus und ihrer Mikrostruktur kann das elastische Verhalten dünner Schichten nicht ohne weiteres mit dem elastischen Verhalten eines dreidimensionalen (Bulk-)Vielkristalls, der aus Kristalliten des gleichen Materials wie die dünne Schicht aufgebaut ist, gleichgesetzt werden. Es ist vielmehr zu erwarten, daß sich der quasi-zweidimensionale Aufbau einer Schicht sowie ihre Mikrostruktur in der Symmetrie der elastischen Eigenschaften widerspiegelt, also keine elastische Isotropie, sondern höchstens Rotationssymmetrie der elastischen Eigenschaften bezüglich der Oberflächennormalen vorliegt (Stickforth, 1966, van Leeuwen *et al.*, 1999; im folgenden als transversale elastische Isotropie bezeichnet). Da die herkömmlichen Kornwechselwirkungsmodelle (siehe oben) jedoch (in der Abwesenheit von kristallografischer Textur) für einen Vielkristall elastische Isotropie implizieren, sind diese für die Anwendung auf dünne Schichten nur eingeschränkt geeignet.

Erst kürzlich wurde das Vorliegen von mechanischer elastischer Anisotropie (hier: transversaler elastischer Isotropie) in einer dünnen, untexturierten Nickelschicht von van Leeuwen *et al.* (1999) experimentell mittels einer röntgenografischen Spannungsmessung nachgewiesen; bei einer Auftragung der gemessenen Gitterdehnung für verschiedene Beugungslinien gegen $\sin^2\psi$ (,$\sin^2\psi$-Auftragung') wurden jeweils nicht-lineare Verläufe gefunden, die sich für die betrachteten Proben nur beim Vorliegen von mechanischer elastischer Anisotropie ergeben können (siehe auch Kapitel 2 dieser Arbeit und Stickforth,

1966). Eine Auswertung der experimentellen Ergebnisse wurde nur durch die Entwicklung eines Kornwechselwirkungsmodells, welches auf von Vook und Witt (1965) vorgeschlagenen Kornwechselwirkungsannahmen basiert, möglich. In diesem Modell ist die elastische Wechselwirkung von Kristalliten abhängig von der Richtung in der betrachteten Probe, weswegen es im folgenden als ‚richtungsabhängiges Kornwechselwirkungsmodell' bezeichnet wird.

In *Kapitel 2* dieser Arbeit wird gezeigt, daß bei der Anwendung richtungsabhängiger Kornwechselwirkungsmodelle (weitere richtungsabhängige Kornwechselwirkungsmodelle werden in Kapitel 4 vorgestellt) die sogenannten röntgenografischen Spannungsfaktoren (Dölle & Hauk, 1978, Dölle & Hauk, 1979) zur Auswertung von röntgenografischen Spannungsmessungen benutzt werden können. Weiterhin wird gezeigt, daß die röntgenografischen Spannungsfaktoren die allgemeinste Formulierung des Zusammenhangs der Gitterdehnung mit den mechanischen Spannungen im Probensystem darstellen. Für makroskopisch elastisch isotrope Proben ist die Verwendung der röntgenografischen elastischen Konstanten jedoch eine mathematisch sehr viel einfachere Alternative (siehe auch Stickforth, 1966).

Im *Kapitel 3* dieser Arbeit wird das Vook-Witt Kornwechselwirkungsmodell erweitert, so daß eine Anwendung für Proben mit kristallografischer Textur ermöglicht wird. Basierend auf der Simulation von Gitterdehnungen für fasertexturierte Proben ließ sich zeigen, daß fehlerhafte Ergebnisse für die Eigenspannungen (bis zu 50% Abweichungen) erhalten werden können, wenn die Kornwechselwirkung in der Probe dem Vook-Witt Modell folgt, aber bei der Auswertung eines der herkömmlichen Kornwechselwirkungsmodelle zur Berechnung der röntgenografischen elastischen Konstanten (bzw. Spannugsfaktoren) angewendet wird.

Im *Kapitel 4* dieser Arbeit wird ein verallgemeinertes richtungsabhängiges Kornwechselwirkungsmodell vorgestellt. Obwohl das Vook-Witt Modell für die Anwendung auf dünne Schichten besser geeignet als die herkömmlichen Kornwechselwirkungsmodelle, da nur das Vook-Witt Modell mit transversaler elastischer Isotropie kompatibel ist, während die herkömmlichen Kornwechselwirkungsmodelle mechanische elastische Isotropie implizieren, werden dennoch extreme Kornwechselwirkungsannahmen verwendet. Es wird davon ausgegangen daß parallel zur Oberfläche alle Kristallite die gleiche Dehnung aufweisen (d.h. eine Voigt-artige Kornwechselwirkung vorliegt) und senkrecht zur Oberfläche alle Kristallite die gleiche Spannung aufweisen (d.h. eine Reuss-artige Kornwechselwirkung vorliegt). Es ist aus der Literatur bekannt (siehe z.B. Hill, 1952, Neerfeld, 1942) daß extremale Kornwechselwirkungsannahmen nicht mit dem Verhalten von realen Vielkristallen

kompatibel sind. In dieser Arbeit wurde ein sogenanntes effektives Kornwechselwirkungsmodell entwickelt, welches auf einer linearen Kombination von mehreren (extremalen) Kornwechselwirkungsmodellen beruht. Dieses Modell ist das erste richtungsabhängige Kornwechselwirkungsmodell welches nicht auf extremalen Annahmen für die Kornwechselwirkung basiert, sondern mit dessen Hilfe richtungsabhängige Kornwechselwirkung quantitativ durch die Einführung von Kornwechselwirkungsparametern beschrieben werden kann.

In *Kapitel 5* werden die Korrekturen von instrumentellen Aberrationen für röntgenografische Texturuntersuchungen (Polfigurmessungen), die mit einer Röntgenpolykappilarlinse durchgeführt wurden, diskutiert.

Kristallografische Textur wird häufig in dünnen Schichten angetroffen und hat einen signifikanten Einfluß auf die mechanischen elastischen und röntgenelastischen Eigenschaften. Es ist daher notwendig, die Textur bei der Auswertung röntgenografischer Messungen quantitativ zu berücksichtigen. In dieser Arbeit wurde für die Spannungs- und Texturuntersuchungen eine sogenannte Röntgenpolykapillarlinse verwendet (siehe z.B. Kumachov & Komarov, 1990, Kogan & Bethke, 1998, Scardi *et al.*, 2000), welche seit einigen Jahren erhältlich ist. Die Anwendung dieser röntgenoptischen Komponente ist noch nicht weit verbreitet und aus diesem Grund existieren in der Literatur noch keine Korrekturverfahren für instrumentelle Aberrationen. In dieser Arbeit wurden die Korrekturen, welche für quantitative röntgenografische Texturmessungen notwendig sind, experimentell untersucht und es wurden geeignete Korrekturmethoden entwickelt.

6.2. Röntgenografische Spannungsanalyse markoskopisch elastisch anisotroper Vielkristalle; das Konzept der röntgenografischen elatischen Konstanten und der röntgenografischen Spannnungsfaktoren – Kapitel 2

Bei der Auswertung der röntgenografischen Spannungsmessung wird in der Regel zwischen untexturierten (makroskopisch elastisch isotropen) und texturierten Proben unterschieden (sieh z.B. Hauk, 1997). Für untexturierte Proben werden zur Auswertung die sogenannten röntgenografischen elastischen Konstanten S_1^{hkl} und $\frac{1}{2}S_2^{hkl}$ benutzt. Der Zusammenhang der Gitterdehnung für eine Röntgenbeugungslinie *hkl* (in die durch die Winkel ψ und φ charakterisierte Richtung des Beugungsvektors) mit den Komponenten des mechanischen

Spannungstensors, ausgedrückt im Probensystem S, $\left\langle \sigma_{ij}^{S} \right\rangle$, wird durch das $\sin^2\psi$-Gesetz beschrieben (siehe, z.B. Hauk, 1997, siehe auch Stickforth, 1966):

$$
\begin{aligned}
\varepsilon_{\varphi,\psi}^{hkl} = {} & \tfrac{1}{2} S_2^{hkl} \sin^2\psi \left(\left\langle \sigma_{11}^{S} \right\rangle \cos^2\varphi + \left\langle \sigma_{12}^{S} \right\rangle \sin(2\varphi) + \left\langle \sigma_{22}^{S} \right\rangle \sin^2\varphi \right) + \\
& + \tfrac{1}{2} S_2^{hkl} \left(\left\langle \sigma_{13}^{S} \right\rangle \cos\varphi \sin(2\psi) + \left\langle \sigma_{23}^{S} \right\rangle \sin\varphi \sin(2\psi) + \left\langle \sigma_{33}^{S} \right\rangle \cos^2\psi \right) \quad (6.1) \\
& + S_1^{hkl} \left(\left\langle \sigma_{11}^{S} \right\rangle + \left\langle \sigma_{22}^{S} \right\rangle + \left\langle \sigma_{33}^{S} \right\rangle \right)
\end{aligned}
$$

Für texturierte Proben werden die sogenannten röntgenografischen Spannungsfaktoren $F_{kl}(\psi,\varphi,hkl)$ benutzt (siehe Dölle & Hauk, 1978, Dölle & Hauk, 1979, Hauk, 1997) und der Zusammenhang der Gitterdehnung mit den Komponenten des mechanischen Spannugstensors, $\left\langle \sigma_{ij}^{S} \right\rangle$, kann geschrieben werden als (die Einsteinsche Summenkonvention, d.h. Summation über wenigstens doppelt vorkommende Indizes, wird benutzt):

$$
\varepsilon_{\varphi,\psi}^{hkl} = F_{kl}(\psi,\varphi,hkl) \left\langle \sigma_{kl}^{S} \right\rangle . \tag{6.2}
$$

Von van Leeuwen *et al.* (1999) wurde gezeigt, daß makroskopische elastische Anisotropie auch für untexturierte Proben auftreten kann, falls richtungsabhängige Kornwechselwirkung vorliegt. Insbesondere wurden für eine Probe mit ebenem, rotationssymmetrischem Spannungszustand experimentell nicht-lineare $\sin^2\psi$-Verläufe beobachtet, welche mit Gleichung (6.1) nicht kompatibel sind. Daraus folgt, daß selbst für untexturierte Proben welche einer richtungsabhängigen Kornwechselwirkung unterliegen, das herkömmlich $\sin^2\psi$-Gesetz (Gleichung (6.1)) nicht angewendet werden kann.

In dieser Arbeit wird gezeigt, daß die röntgenografischen Spannungsfaktoren (d.h. Gleichung (6.2)) generell für makroskopisch elastisch anisotrope Proben verwendet werden können. Insbesondere gilt Gleichung (6.2) auch für Proben mit richtungsabhängiger Kornwechselwirkung, unabhängig von kristallografischer Textur.

Die Gültigkeit von Gleichung (6.1) wurde mehr als 40 Jahre nach der ersten röntgenografischen Messung von elastischen Dehnungen (Joffe & Kirpitcheva, 1922) von Stickforth (1966) gezeigt. In diesem Zusammenhang wurde von Stickforth (1966) postuliert, daß das röntgenelastische Verhalten von oberflächennahen Kristalliten von dem Verhalten von Kristalliten im Inneren eines Bulk-Vielkristalls abweicht. In dieser Arbeit wird diskutiert, inwiefern die postulierte Oberflächenanisotropie als Sonderfall von richtungsabhängiger Kornwechselwirkung verstanden werden kann.

6.3. Spannungs- und Dehnungsfelder in transversal elastisch isotropen dünnen Schichten – Kapitel 3

6.3.1. Theoretische Grundlagen

Während in einem dreidimensional ausgedehnten Vielkristall alle Kristallite in allen Richtungen von benachbarten Kristalliten umgeben sind, ist dies für dünne Schichten oder Oberflächen im allgemeinen nicht der Fall. Kornwechselwirkungsannahmen, welche an eine kolumnare, oberflächennahe Mikrostruktur angepaßt sind, wurden von Vook und Witt (1965) vorgeschlagen und erstmals von van Leeuwen *et al.* (1999) als Kornwechselwirkungsmodell auf die röntgenografische Spannungsmessung angewendet.

Im folgenden wird davon ausgegangen daß die Schicht wenigstens transverale elastische Isotropie (d.h. Rotationssymmetrie der elastischen Eigenschaften bezüglich der Oberflächennormalen) aufweist. Die Kornwechselwirkungsannahmen im Vook-Witt Modell sind wie folgt:

1. Die Schicht ist einem Dehnungszustand unterworfen, der Rotationssymmetrie bezüglich der Oberflächennormalen der Probe aufweist.

2. Alle Kristallite haben den gleichen Dehnungszustand in der Ebene der Schicht.

3. Die Spannungen senkrecht zur Oberfläche sind Null für alle Kristallite.

Diese Annahmen legen in einem bezüglich der Probe fixierten Koordinatensystem, dem sogenannten Proben-System, dessen *z*-Achse mit der Oberflächennormalen der Probe zusammenfällt, sechs Komponenten des Spannungs- und Dehnungstensors fest. Im folgenden gibt ein hochgestelltes *S* an, daß ein Tensor im Probensystem zu betrachten ist.

$$
\left.
\begin{aligned}
\varepsilon_{11}^{S} &= \varepsilon_{22}^{S} \overset{def}{=} \varepsilon_{\parallel}^{S} \\
\varepsilon_{12}^{S} &= \varepsilon_{21}^{S} \overset{def}{=} 0 \\
\sigma_{i3}^{S} &= \sigma_{3i}^{S} \overset{def}{=} 0
\end{aligned}
\right\}
\tag{6.3}
$$

Die sechs Komponenten ε_{ij}^{S} des Dehnungstensors und σ_{ij}^{S} des Spannungstensors (beide Tensoren sind symmetrische Tensoren, d.h. $\varepsilon_{ij}^{S} = \varepsilon_{ji}^{S}$ und $\sigma_{ij}^{S} = \sigma_{ji}^{S}$) welche nicht (direkt) durch die Gleichungen (6.3) definiert werden, können unter Verwendung des Hookeschen Gesetzes berechnet werden:

$$
\varepsilon_{ij}^{S} = s_{ijkl}^{S} \sigma_{kl}^{S},
\tag{6.4}
$$

welches mit dem Nachgiebigkeitstensor s_{ijkl}^{S} eines Einkristalls ein lineares Gleichungssystem in 12 Unbekannten darstellt (es muß beachtet werden, daß Spannungs- und Dehnungstensoren symmetrisch sind, d.h. beide Tensoren weisen jeweils nur sechs unabhängige Einträge auf).

Der Nachgiebigkeitstensor im Probensystem kann für jeden Kristallit mittels geeigneter (orthogonaler) Transformationsmatrizen aus dem Nachgiebigkeitstensor im Kristallsystem berechnet werden, welcher für viele Materialien tabelliert vorliegt. Somit sind für alle Kristallite im Vielkristall Dehnungs- und Spannungszustand bekannt und es kann auch das elastische Verhalten des Vielkristalls berechnet werden. Zur Berechnung des mechanischen elastischen Verhaltens sind Mittelwerte über alle Kristallite in der Probe zu berechnen während für die Berechnung des röntgenografischen elastischen Verhaltens sich die Mittelung nur über die in einem Beugungsexperiment erfaßten Kristallite erstreckt (also über Kristallite, für die der Beugungsvektor senkrecht zu den dem betrachteten Reflex entsprechenden Ebenen orientiert ist).

Im folgenden wird ein ebener, rotationssymmetrischer (mechanischer) Spannungszustand betrachtet (mechanische Spannungs- und Dehnungstensoren werden in eckige Klammern gesetzt um diese gegen Spannungen und Dehnungen einzelner Kristallite abzugrenzen):

$$\left\langle \sigma^{S} \right\rangle = \begin{pmatrix} \sigma_{\parallel}^{\,S} & 0 & 0 \\ 0 & \sigma_{\parallel}^{\,S} & 0 \\ 0 & 0 & 0 \end{pmatrix}. \tag{6.5}$$

Es genügt die Kenntnis der zwei mechanischen elastischen Konstanten A und B zur Beschreibung des mechanischen elastischen Verhaltens:

$$\varepsilon_{\parallel}^{S} = A\sigma_{\parallel}^{S}, \tag{6.6}$$

$$\varepsilon_{\perp}^{S} = B\sigma_{\parallel}^{S}. \tag{6.7}$$

Dabei bezeichnet $\varepsilon_{\parallel}^{S}$ die Dehnung (aller Kristallite) parallel zum Substrat und $\varepsilon_{\perp}^{S}$ die mechanische, d.h. über alle Kristallite gemittelte Dehnung, senkrecht zur Oberfläche der Schicht so daß für den mechanischen Dehnungstensor

$$\left\langle \varepsilon^{S} \right\rangle = \begin{pmatrix} \varepsilon_{\parallel}^{S} & 0 & 0 \\ 0 & \varepsilon_{\parallel}^{S} & 0 \\ 0 & 0 & \varepsilon_{\perp}^{S} \end{pmatrix} \tag{6.8}$$

geschrieben werden kann.

Das röntgenelastische Verhalten wird im folgenden durch eine sogenannte $\sin^2\psi$-Auftragung veranschaulicht, wobei die Gitterdehnung ε_ψ^{hkl}, welche für eine bestimmte Röntgenlinie erhalten wird, gegen $\sin^2\psi$ aufgetragen wird.

In der vorliegenden Arbeit wurde nun die kristallografische Textur in die Betrachtungen einbezogen. Dazu muß bei der Berechnung des mechanischen und des röntgenografischen elastischen Verhaltens die sogenannte Orientierungsverteilungsfunktion (ODF) als Wichtungsfaktor berücksichtigt werden (siehe z.B. Bunge, 1982a, 1999), welche angibt mit welcher Häufigkeit die verschiedenen Kristallitorientierungen in der betrachteten Probe vorkommen.

Im folgenden werden sowohl das mechanische elastische Verhalten (charakterisiert durch die mechanischen elastischen Konstanten A und B) sowie das röntgenelastische Verhalten (charakterisiert durch eine Auftragung der Gitterdehnung für verschiedene Reflexe gegen $\sin^2\psi$) für verschieden Kornwechselwirkungsmodelle veranschaulicht und diskutiert. Dabei wird das auf den Annahmen von Vook und Witt basierende Kornwechselwirkungsmodell mit den Modellen nach Reuss und Voigt (für die mechanischen elastischen Konstanten A und B auch nach Neerfeld-Hill) verglichen. Für eine detaillierte Beschreibung dieser Modelle sei auf Kapitel 3 dieser Arbeit verwiesen.

6.3.2 Mechanisches und röntgenelastisches Verhalten fasertexturierter Polykristalle nach den Kornwechselwirkungsmodellen von Reuss, Voigt und Vook - Witt

Zur Veranschaulichung des Einflusses einer kristallografischen Textur wurden für verschiedene (kubische) Materialien, welche sich in ihrer elastischen Anisotropie unterscheiden, Berechnungen durchgeführt. Im folgenden sei als Beispiel nur Niob herausgegriffen, welches sich durch eine hohe elastische Anisotropie auszeichnet. Für weitere Beispiele sei an dieser Stelle auf Kapitel 3 dieser Arbeit verwiesen.

Exemplarisch ist in Abbildung 6.1 die Abhängigkeit der mechanischen elastischen Konstanten A und B von der Breite der Verteilung einer {111} Fasertextur dargestellt.
Für eine ‚perfekte‘ {111} Fasertextur (Breite 0°) werden die elastischen Konstanten unabhängig von der vorliegenden Kornwechselwirkung, d.h. die verschiedenen Modellrechnungen liefern identische Werte für A und B (Kamminga *et al.*, 2000; Vook & Witt, 1965). Die ist nicht der Fall für eine ‚perfekte‘ {110} Fasertextur.

Der Einfluß der Textur auf das röntgenelastische Verhalten wird in Abbildung 6.2 veranschaulicht.
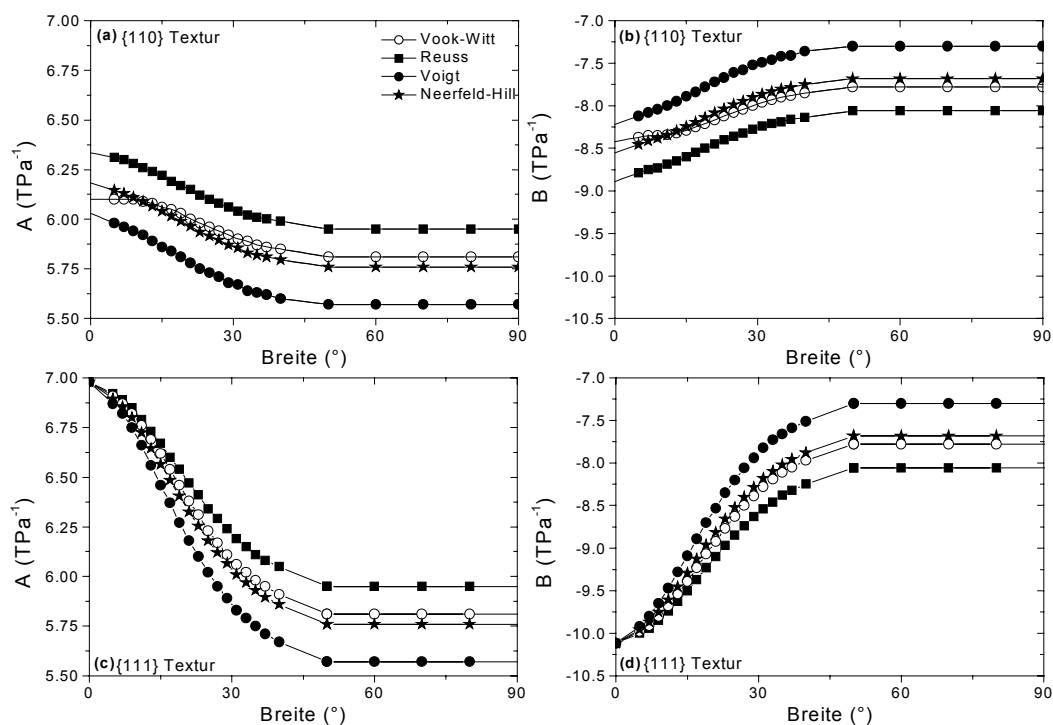
Abbildung 6.1: Texturierte, transversal elastisch isotrope Niob Schicht; Verlauf der mechanischen elastischen Konstanten A und B berechnet für verschiedene Kornwechselwirkungsmodelle als Funktion der Breite der Textur (Gaußsche Fasertextur, Breite entspricht der halben Breite bei halber Höhe der Orientierungsverteilungsfunktion).

Nur geringe Unterschiede ergeben sich für die verschiedenen Modelle in Abwesenheit von Textur. Wenn eine Textur berücksichtigt wird, so ergeben sich signifikant nicht-lineare Verläufe für die Modelle von Reuss und Vook-Witt: der Einfluß der intrinsischen elastischen Anisotropie von Niob auf das röntgenelastische Verhalten wird durch die Textur verstärkt. Insbesondere für die 222 und 400 (allgemeiner: 00*l* und *hhh*) Reflektion treten die Unterschiede zwischen dem Vook-Witt Kornwechselwirkungsmodelle und den Modellen nach Reuss und Voigt besonders hervor, da diese Modelle (wie alle herkömmlichen Kornwechselwirkungsmodelle) hier lineare Verläufe liefern (Brakman, 1983), für das Vook-Witt Modell aber ausgeprägte Nichtlinearitäten auftreten.

Es soll an dieser Stelle nur kurz erwähnt werden daß die Anwendung der traditionellen $\sin^2 \psi$-Auswertung auf der Basis der sogenannten röntgenografischen elastischen Konstanten für den Fall, daß der Vielkristall der Vook-Witt Kornwechselwirkung unterliegt, zu erheblich verfälschten Spannungswerten führt.
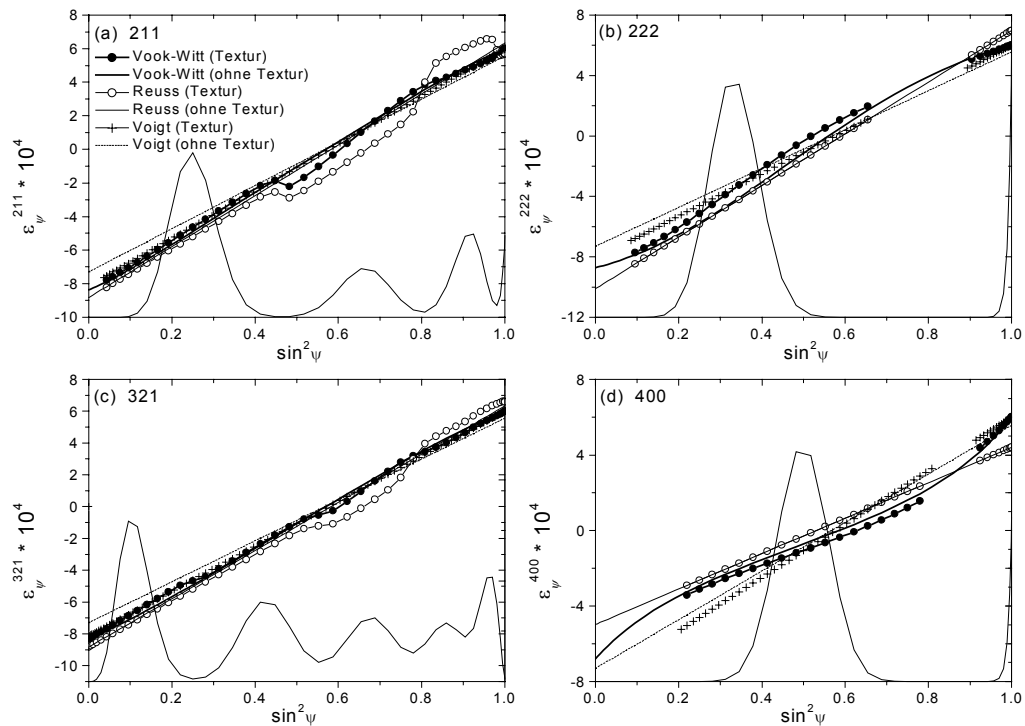
Abbildung 6.2: Texturierte, transversal elastisch isotrope Niob-Schicht (Gaußsche {110} Fasertextur mit 5° Breite); berechnete Gitterdehnung ε_ψ^{hkl} für verschiedene Reflektionen ((a) 211, (b) 222, (c) 321 und (d) 400) aufgetragen gegen $\sin^2\psi$ für eine Spannung $\sigma_\parallel^S$ von 100 MPa. Die integrale Intensität, welche dem Volumenanteil von diffraktierenden Kristalliten proportional ist, wird durch die (dünne) durchgezogene Linie dargestellt.

Die auftretenden Fehler können in der Größenordnung von 50% liegen. Für eine genauere Diskussion auf der Basis von berechneten Beispielen sei der Leser auf Kapitel 3. dieser Arbeit verwiesen.

6.3.3. Zusammenfassung

Der Einfluß der Kornwechselwirkung im Vielkristall auf die mechanischen elastischen Konstanten ist, unabhängig von der betrachteten Textur, eher gering. Sehr viel stärker ausgeprägt ist der Einfluß der Kornwechselwirkung auf das röntgenelastische Verhalten, wie es durch die Auftragung der Gitterdehnung für einen bestimmten Reflex gegen $\sin^2\psi$ beschrieben wird. Selbst für untexturierte Proben können signifikant nicht-lineare Verläufe auftreten. Die Auswertung von röntgenografischen Dehnungsmessungen an dünnen Filmen, welche der Vook-Witt Kornwechselwirkung unterliegen, mittels herkömmlicher Methoden (d.h. unter Verwendung der röntgenografischen elastischen Konstanten) kann zu stark verfälschten Spannungswerten führen (Fehler bis zu 50%).

6.4. Die Bestimmung von Spannungen in dünnen Schichten; Modellierung der elastischen Kornwechselwirkung – Kapitel 4

6.4.1. Theoretische Grundlagen - Die Modellierung von richtungsabhängiger elastischer Kornwechselwirkung

Neerfeld (1942) und Hill (1952) folgerten auf der Basis experimenteller Ergebnisse, daß das elastische Verhalten von Vielkristallen im allgemeinen nicht durch die Modelle von Reuss und Voigt beschrieben werden kann. Neerfeld (1942) schlug basierend auf experimentellen Daten vor, die röntgenografischen und mechanischen elastischen Konstanten durch die Mittelwerte der entsprechenden nach den Voigt und Reuss Modellen berechneten Konstanten zu ersetzen. Die gleiche Vorgehensweise wurde ebenso von Hill (1952) empirisch für die mechanischen elastischen Konstanten vorgeschlagen. Hill (1952) zeigte außerdem, daß die Modelle von Reuss und Voigt extremale Annahmen für die Kornwechselwirkung darstellen: diese beiden Modelle liefern Unter- und Obergrenze für die mechanischen elastischen Konstanten.

Die Verwendung der (arithmetischen) Mittelwerte der elastischen Konstanten gemäß der Modelle von Reuss und Voigt wird deshalb in der Literatur als Neerfeld-Hill Modell bezeichnet. Im folgenden wird ein Modell, bei dem Mittelwerte von elastischen Konstanten, welche mittels extremaler Modelle berechnet wurden, benutzt werden als effektives Kornwechselwirkungsmodell bezeichnet.

Das Vook-Witt Modell stellt hinsichtlich der Kornwechselwirkungsannahmen einen ‚Kompromiß' der Modelle nach Reuss und Voigt dar (siehe auch 6.3 und Kapitel 3). Dennoch werden für die beiden Hauptrichtungen in einer dünnen Schicht, in der Schichtebene und senkrecht zur Oberfläche, extremale Kornwechselwirkungsannahmen gemacht. Für alle Richtungen parallel zur Oberfläche wird davon ausgegangen, daß alle Kristallite die gleiche Dehnung aufweisen (d.h. eine Voigt-artige Kornwechselwirkung vorliegt), während für die Richtung senkrecht zur Oberfläche davon ausgegangen wird, daß alle Kristallite die gleiche Spannung aufweisen (d.h. eine Reuss-artige Kornwechselwirkung vorliegt). Aus diesem Grund muß das Vook-Witt Kornwechselwirkungsmodell als ein extremales Kornwechselwirkungsmodell betrachtet werden und folglich kann auch nicht allgemein davon ausgegangen werden daß das Vook-Witt Modell in der Lage ist, das (reale) Verhalten von Vielkristallen zu beschreiben.

Im folgenden wird ein verallgemeinertes Kornwechselwirkungsmodell vorgeschlagen, welches analog zum Neerfeld-Hill Modell als effektives Kornwechselwirkungsmodell auf einer linearen Kombination von extremalen Modellen basiert. Es wird gezeigt, daß für eine gegebene Probe eine geeignete Auswahl von Kornwechselwirkungsmodellen zur Auswertung von röntgenografischen Spannungsmessungen bestimmt werden kann.

In Bulk-Vielkristallen können alle Richtungen bezüglich der Kornwechselwirkung äquivalent sein und deswegen existieren für (solche) Bulk-Vielkristalle zwei verschiedene extremale Annahmen für die Kornwechselwirkung ('Reuss-artig' und 'Voigt-artig'). Im Gegensatz dazu besitzen dünne, oberflächennahe Schichten zwei Hauptrichtungen, parallel und senkrecht zur Oberfläche, für die jeweils zwei mögliche extremale Kornwechselwirkungen ('Reuss-artig' und 'Voigt-artig') vorliegen können. Aus diesem Grund können vier extremale Kornwechselwirkungsmodelle für eine dünne Schicht formuliert werden. Diese vier Modelle werden im folgenden zusammengestellt:

1. Das Voigt Modell

   Alle Kristallite weisen bezüglich beider Hauptrichtungen identische Dehnungen auf, können sich also nicht (dehnungs-)unabhängig von benachbarten Kristalliten deformieren.

2. Das Reuss Modell

   Alle Kristallite weisen identische Spannungen auf und können sich unter dem Einfluß dieser Spannungen (dehnungs-)unabhängig von benachbarten Kristalliten deformieren.

3. Das Vook-Witt Modell

   Alle Kristallite weisen parallel zur Oberfläche identische Dehnungen auf ('Voigt-artige Kornwechselwirkung'), während sie sich senkrecht zur Oberfläche (dehnungs-)unabhängig von benachbarten Kristalliten deformieren können und gleiche Spannungen aufweisen ('Reuss-artige Kornwechselwirkung').

Das vierte Kornwechselwirkungsmodell wird in dieser Arbeit eingeführt:

4. Das inverse Vook-Witt Modell

   Alle Kristallite können sich in der Schichtebene (dehnungs-)unabhängig von benachbarten Kristalliten verformen ('Reuss-artige Kornwechselwirkung') und weisen die gleichen Spannungen auf, während sie senkrecht zur Oberfläche die gleichen Dehnungen aufweisen ('Voigt-artige Kornwechselwirkung').

Das inverse Vook-Witt Modell ist ein neues Kornwechselwirkungsmodell, welches für die Konstruktion eines effektiven Kornwechselwirkungsmodells benötigt wird. Im folgenden

wird vorausgesetzt, daß der Vielkristall wenigstens transversale elstische Isotropie aufweist (siehe auch 6.1) und einem ebenen, rotationssymmetrischen Spannungszustand unterworfen ist. Die Kornwechselwirkungsannahmen für das inverse Vook-Witt Modell sind:

(i) die Spannung parallel zur Oberfläche ist rotationssymmetrisch und (ii) parallel zur Oberfläche gleich für alle Kristallite und (iii) die Dehnung senkrecht zur Oberfläche ist gleich für alle Kristallite.

Wie schon beim Vook-Witt Modell (vergl. 6.3 und Kapitel 3) fixieren diese Kornwechselwirkungsannahmen sechs Komponenten des Spannungs- und Dehnungstensors:

$$
\left.
\begin{aligned}
\sigma_{11}^S &= \sigma_{22}^S \overset{def}{=} \sigma_{\parallel}^S \\
\sigma_{12}^S &= \sigma_{21}^S \overset{def}{=} 0 \\
\varepsilon_{i3}^S &= \varepsilon_{3i}^S \overset{def}{=} 0, \quad i = 1,2 \\
\varepsilon_{33}^S &= \varepsilon_{\perp}^S
\end{aligned}
\right\}
\tag{6.9}
$$

Die noch fehlenden sechs Komponenten können unter Benutzung der Gleichung (6.4) (siehe auch Text unter Gleichung (6.4)) berechnet werden, so daß eine Bestimmung der röntgenografischen und mechanischen elastischen Konstanten möglich ist.

Basierend auf den vier beschriebenen Modellen kann ein effektives Kornwechselwirkungsmodell konstruiert werden. Das folgende Beispiel soll der Illustration dienen: Die Modelle nach Reuss und Vook-Witt können kombiniert werden, wenn für die Berechnung der röntgenografischen Spannungsfaktoren (und der mechanischen elastischen Konstanten) davon ausgegangen wird, daß ein Volumenanteil f_R von Kristalliten dem Reuss-Kornwechselwirkungsmodell unterliegt, während ein Volumenanteil $f_{VW} = 1 - f_R$ dem Vook-Witt Kornwechselwirkungsmodell unterliegt. Ein solches durch Mittelung erhaltenes Kornwechselwirkungsmodell kann so verstanden werden, daß effektiv für die Richtungen in der Schichtebene eine Kornwechselwirkung vorliegt, die zwischen den extremalen ‚Reuss-artigen' und ‚Voigt-artigen' Annahmen liegt; während die Kristallite gemäß dem Vook-Witt Modell starr miteinander verbunden sind und alle die gleiche Dehnung aufweisen, führt die Kombination mit dem Reuss-Modell dazu, daß diese unrealistische Kornwechselwirkungsannahme aufgehoben wird.

Eine Quantifizierung der effektiven Kornwechselwirkung kann durch die Einführung von Wechselwirkungsparametern für die zwei Hauptrichtungen erzielt werden:

- Wechselwirkungsparameter parallel zur Oberfläche $w_{\parallel}$: $w_{\parallel} = 1$ falls alle Kristallite identische Dehnungen aufweisen (‚Voigt-artige Kornwechselwirkung', Kristallite sind starr verbunden) und $w_{\parallel} = 0$ falls alle Kristallite gleiche Spannungen aufweisen (‚Reuss-

artige Kornwechselwirkung', Kristallite können sich unabhängig von benachbarten Kristalliten deformieren).

- Wechselwirkungsparameter senkrecht zur Oberfläche $w_\perp$: Definition analog zu $w_\parallel$.

Die Kombination mehrerer Kornwechselwirkungsmodelle resultiert in gemittelten Wechselwirkungsparametern $\langle w_\parallel \rangle$ und $\langle w_\perp \rangle$:

$$\langle w_\parallel \rangle = \sum_i f_i w_{\parallel,i} \tag{6.10}$$

$$\langle w_\perp \rangle = \sum_i f_i w_{\perp,i} . \tag{6.11}$$

In den Gleichungen (6.10) und (6.11) repräsentieren die Parameter f_i Volumenfraktionen von Kristalliten welche dem Kornwechselwirkungsmodell i unterliegen.

$$\sum_i f_i = 1 . \tag{6.12}$$

6.4.2. Experimentelle Ergebnisse und Diskussion

Das in dieser Arbeit entwickelte Kornwechselwirkungsmodell wurde auf die Spannungsmessung einer gesputterten, 500nm dicken Kupferschicht angewendet. Die Probenherstellung ist detailliert in Kapitel 4 dieser Arbeit beschrieben. Eine Charakterisierung der Textur durch Berechnung der Orientierungsverteilungsfunktion wurde durch Analyse der integralen Intensitäten der Röntgenbeugungslinien aus der Spannungsmessung durchgeführt. Die integralen Intensitäten wurden mittels des in Kapitel 5 (siehe auch Kapitel 6.5) beschriebenen Verfahrens auf instrumentelle Effekte korrigiert. Zusätzlich zu den röntgenografischen Messungen wurden Untersuchungen der Mikrostruktur mittels Ionenstrahlmikroskopie durchgeführt.

Es ergab sich, daß eine Auswertung der Spannungsmessung mit dem in dieser Arbeit vorgestellten effektiven Kornwechselwirkungsmodell, nicht aber mit den herkömmlichen Kornwechselwirkungsmodellen möglich ist. Insbesondere wurden nichtlineare $\sin^2\psi$-Verläufe für die 111 und 200 Reflektionen beobachtet, welche durch die Modelle aus der Literatur nicht erklärt werden können. In Abbildung 6.3 sind die gemessenen $\sin^2\psi$-Auftragungen für sechs Reflexe zusammen mit den berechneten Verläufen dargestellt. Der Spannungswert ergibt sich aus einer Anpassung von berechneten $\sin^2\psi$-Verläufen an die gemessenen Verläufe und wurde zu 165 MPa (Zugspannung) bestimmt. Die Parameter f_i, welche den Anteil des Kornwechselwirkungsmodells i an der effektiven Kornwechselwirkung in der

Probe beschreiben, wurden ebenfalls als freie Parameter in der Anpassung benutzt. Die daraus abgeleiteten Kornwechselwirkungsparemeter ergaben sich zu $w_\parallel = 0.6$ und $w_\perp = 0.1$. Für weitere Details der Auswertung sei der Leser an dieser Stelle auf Kapitel 4 der Arbeit verwiesen.

Die Kornwechselwirkungsparameter zeigen, daß parallel zur Oberfläche eine Kornwechselwirkung zwischen den extremalen Kornwechselwirkungen nach Voigt und Reuss auftritt, also eine Kornwechselwirkung ähnlich wie in einem Bulk-Vielkristall vorliegt, währenddessen sich die Kristallite senkrecht zur Oberfläche praktisch unabhängig von benachbarten Kristalliten verformen können, d.h. eine ‚Reuss-artige' Kornwechselwirkung vorliegt. Dieses Ergebnis ist mit der kolumnaren Mikrostruktur der Schicht kompatibel, welche in den mikroskopischen Untersuchungen gefunden wurde.
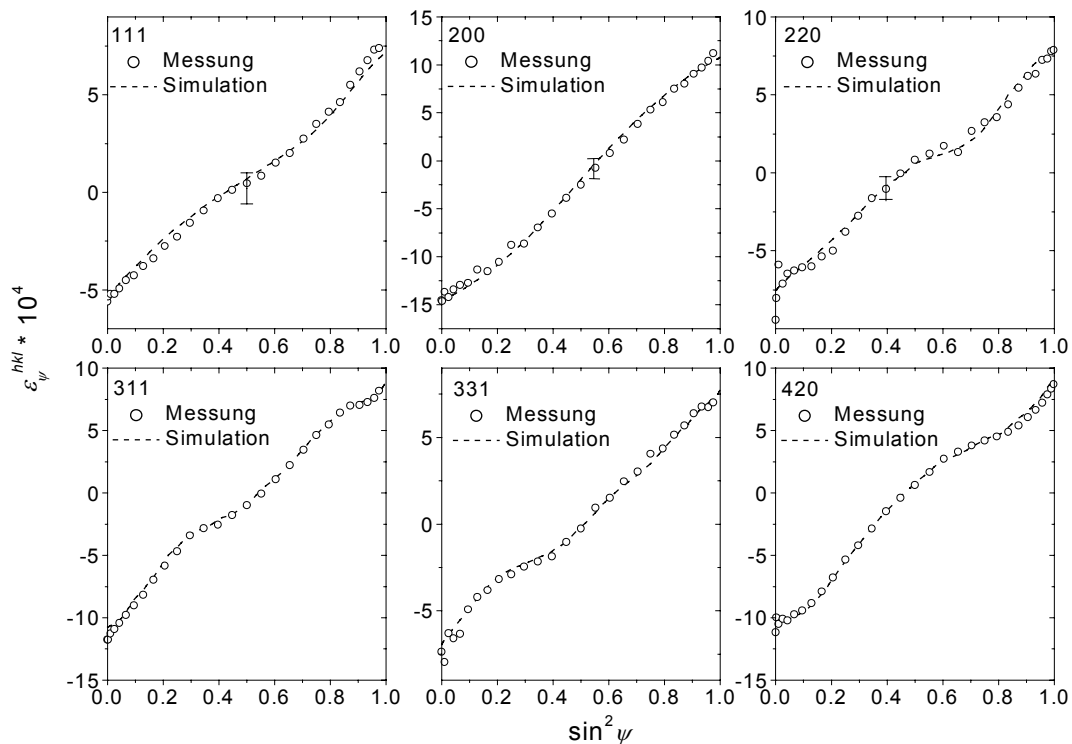
Abbildung 6.3: Spannungsanalyse einer texturierten Kupferschicht. Auftragung der gemessenen (offene Kreise) und berechneten (gestrichelte Linie) Verläufe der Gitterdehnung für verschiedene Röntgenbeugungslinien gegen $\sin^2\psi$.

6.4.3. Zusammenfassung

Die herkömmlichen Kornwechselwirkungsmodelle (z.B. die Modelle nach Reuss und nach Voigt) können für die Anwendung auf dünne Schichten ungeeignet sein. Diese Modelle implizieren, daß ein Vielkristall (in der Abwesenheit von Textur) elastisch isotrop ist, während dünne Schichten (auch in der Abwesenheit von Textur) elastisch anisotrop sein können.

Das Vook-Witt Kornwechselwirkungsmodell ist das erste Modell, welches auf richtungsabhängigen Kornwechselwirkungsannahmen beruht. Dabei wird angenommen, daß alle Kristallite die gleiche Dehnung parallel zur Oberfläche und die gleiche Spannung senkrecht dazu aufweisen. Dieses Modell impliziert, daß ein Vielkristall (auch wenn keine kristallographische Textur vorliegt) elastisch anisotrop ist.

In Analogie zu den Modellen nach Reuss und Voigt wird in dieser Arbeit das sogenannte ‚inverse Vook-Witt' Modell vorgeschlagen. Dieses Modell ist komplementär zum Vook-Witt Modell und es wird davon ausgegangen, daß alle Kristallite die gleiche Spannung parallel zur Oberfläche und die gleiche Dehnung senkrecht zur Oberfläche aufweisen.

Die Modelle nach Reuss, Voigt, Vook-Witt und das in dieser Arbeit vorgestellte Modell basieren auf extremen Kornwechselwirkungsannahmen, welche i.a. nicht mit realen Vielkristallen kompatibel sind. In dieser Arbeit wird ein effektives Kornwechselwirkungsmodell vorgeschlagen, welches auf einer (linearen) Kombination von vier Modellen - Reuss, Voigt, Vook-Witt und inverses Vook-Witt - beruht und mit dessen Hilfe die Richtungsabhängigkeit der Kornwechselwirkung durch Kornwechselwirkungsparameter quantitativ beschrieben werden kann.

Das vorgeschlagene Modell wurde auf die Spannungsanalyse einer dünnen (500 nm) Kupferschicht angewendet. Während eine Auswertung auf der Basis der herkömmlichen Modelle nicht möglich war, konnte mittels des in dieser Arbeit vorgeschlagenen Modells eine simultane Auswertung von $\sin^2\psi$-Auftragungen für sechs verschiedene Beugungslinien durchgeführt werden. Die aus dem Modell resultierenden Kornwechselwirkungsparameter, welche die Richtungsabängigkeit der Kornwechselwirkung beschreiben, sind in Übereinstimmung mit der kolumnaren Mikrostruktur der Schicht, welche in mikroskopischen Untersuchungen nachgewiesen wurde.
In dieser Arbeit gelang es erstmals, richtungsabhängige Kornwechselwirkung quantitativ zu beschreiben.

6.5. Die Benutzung von Polykapillarröntgenlinsen für Texturuntersuchungen – Kapitel 5

6.5.1. Grundlagen

Für röntgenografische Untersuchungen steht heutzutage ein Vielzahl von neuen optischen Komponenten für den Anwender zur Verfügung. Im Bereich der Textur- und Spannungsanalyse finden insbesondere sogenannte Polykapillarröntgenlinsen Verwendung (siehe z.B. Kumachov & Komarov, 1990, Kogan & Bethke, 1998, Scardi *et al.*, 2000).

Diese ‚Linsen' nutzen den Effekt der Totalreflektion aus, welcher für Röntgenstrahlen auftritt, wenn diese unter einem sehr flachen Winkel (typisch einige Zehntelgrad) auf ein optisch dünneres Medium treffen. Da der Brechungsindex in Festkörpern für Röntgenstrahlen kleiner als eins ist, kann Totalreflektion z.B. beim Auftreffen des Röntgenstrahls auf eine Glasoberfläche auftreten (der Brechungsindex von Luft ist nahezu exakt eins). Dieser Effekt wird in Polykapillarlinsen ausgenutzt, um aus dem vom Röhrenfokus abgestrahlten, divergenten Strahlbündel ein nahezu paralleles Strahlbündel zu erhalten. Zu diesem Zweck werden die Röntgenstrahlen in sehr dünnen Glaskapillaren z.B. entlang von Segmenten von Parabelbahnen geführt, so daß ein divergentes Strahlenbündel zum einem Parallelstrahl konvertiert wird. Allerdings weist der Strahl immer noch eine Restdivergenz auf, welche durch die Eigenschaften der verwendeten Linse und die Wellenlänge der benutzten Strahlung bestimmt wird. Mittels des erhaltenen Parallelstrahls lassen sich dann Röntgenbeugungsuntersuchungen in (Pseudo-)Parallelstrahlgeometrie durchführen, welche verglichen mit Fokusierungsgeometrien (z.B. Bragg-Brentano Geometrie) außerordentlich geringe instrumentelle Aberrationen aufweist. Überdies stehen, bezogen auf herkömmliche Messgeometrien, vergleichsweise hohe Intensitäten für Beugungsuntersuchungen zur Verfügung.

Röntgenografische Texturuntersuchungen basieren auf der Messung von sogenannten Polfiguren (siehe z.B. Bunge, 1982b, 1999). In einer Polfigurmessung wird die (integrale) Intensität einer bestimmten Beugungslinie, welche dem Volumen der diffraktierenden Kristallite proportional ist (abgesehen von Korrekturen, siehe unten), als Funktion der Winkel ψ und φ gemessen. Allerdings muß die gemessene Intensität korrigiert werden, da verschiedene Effekte die gemessene Intensität verfälschen. Bei der Verwendung von fokusierenden Geometrien (z.B. der Bragg-Brentano Geometrie) müssen Korrekturen für Defokusierung, Änderung der beleuchteten Probenfläche und Überstrahlung, sowie

Absorption durchgeführt werden (siehe z.B. Chernock & Beck, 1952, Gale & Griffiths, 1960, Holland, 1964, Tenckhoff, 1970, Holt & Winegar, 1977, Ortiz & Hermida, 1981, Lahn & Hougardy, 1999). In dieser Arbeit wurden die notwendigen Korrekturen, welche bei der Verwendung einer Polykapillarlinse berücksichtigt werden müssen, an Hand von Messungen an untexturierten Standardproben untersucht und geeignete Korrekturverfahren entwickelt.

6.5.2. Korrekturen bei Verwendung einer Polykapillarlinse

Die Defokusierungskorrektur stellt eine zentrale Korrektur bei der röntgenografischen Texturmessung bei der Verwendung von fokusierenden Messgeometrien (z.B. Bragg-Brentano Geometrie) dar. Unter Defokusierung wird die Verbreiterung einer Beugungslinie verstanden, die entsteht, wenn die Probe bei der Texturmessung verkippt wird, und dadurch Teilbereiche der Probe die Fokusierungsbedingung verletzen. Eine Reduzierung der gemessenen Intensität ergibt sich, wenn ein Teil des verbreiterten diffraktierten Strahls nicht in den Empfangsspalt fällt.

In dieser Arbeit konnte experimentell gezeigt werden, daß auf Grund des (Pseudo-) Parallelstrahlengangs bei Verwendung einer Röntgenlinse keine Defokusierungskorrektur benötigt wird. Da bei Parallelstrahlengang keine Fokusierungsbedingung vorliegt, ergibt sich durch die Verkippung der Probe auch keine Verbreiterung des diffraktierten Strahls (bezüglich des Beugungswinkels). Dies ist für ein Beispiel in Abbildung 6.4 veranschaulicht, in der die Peakparameter von Röntgenbeugungslinien einer Wolfram-Pulverprobe gegen den Verkippungswinkel ψ aufgetragen wurden.

Damit müssen lediglich Absorption und geometrische Effekte, d.h. die Veränderung der bestrahlten Probenoberfläche sowie die Überstrahlung der Probe (und, für große Proben, die Überstrahlung der Optiken im diffraktierten Strahl) korrigiert werden. Die Absorptionskorrektur kann mittels bekannter Formeln leicht durchgeführt werden (siehe z.B. Bunge, 1982b, 1999), so daß nur die geometrischen Effekte besondere Aufmerksamkeit erfordern. In dieser Arbeit wurden zwei Verfahren für die Korrektur von geometrischen Effekten entwickelt. Eines dieser Verfahren beruht auf der Messung von Polfiguren für mehrere Reflektionen einer untexturierten Pulverprobe, welche als Standard für die Ermittlung einer Korrekturfunktion benutzt wird. Ein zweites Verfahren basiert auf einer numerischen Berechnung der geometrischen Korrekturfunktion. Es wird jedoch noch eine Polfigurmessung für eine Reflektion einer untexturierten Standardprobe zur Kalibrierung der Korrektur benötigt (für Details, siehe Kapitel 5). Ein Beispiel ist in Abbildung 6.5. gegeben.
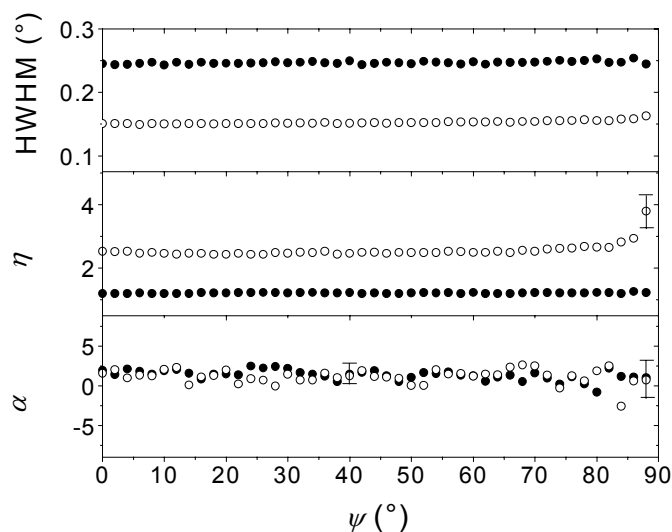
Abbildung 6.4: Parameter der 110 (offene Kreise) und der 321 (gefüllte Kreise) Beugungslinien einer Wolfram Pulverprobe als Funktion des Probenverkippungswinkels ψ: Halbe Breite bei halber Höhe (HWHM), Formfaktor η und Asymmetrie α. Die Parameter wurden durch das Anpassen einer Pearson VII Funktion an die gemessenen Beugungslinien bestimmt.
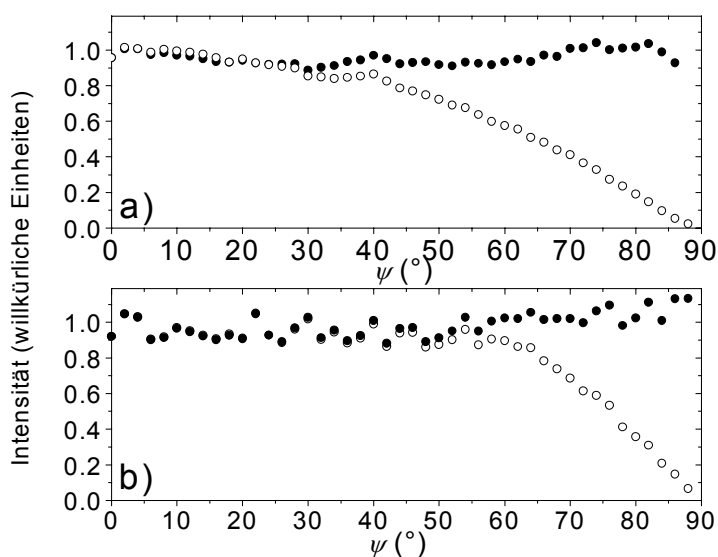

Abbildung 6.5: Experimentelle Korrektur gemessener Intensitäten (Schnitt durch eine Polfigur für φ = konstant; offene Kreise, 111 Beugunslinie (a) und 440 Beugungslinie (b)) einer dicken Germaniumprobe. Die korrigierten Intensitäten sind als gefüllte Kreise dargestellt. Zur Ermittlung der Korrekturfunktion wurden acht Beugungslininen einer Wolframstandardprobe benutzt.

Die gemessene Intensität als Funktion des Kippwinkels für zwei Reflektionen einer Germaniumpulverprobe wurde mittels Standardmessungen an einer Wolframpulverprobe korrigiert. Da die Probe untexturiert ist, sollte sich nach der Korrektur eine von ψ unabhängige Intensität ergeben, was im Beispiel auch gut erfüllt ist.

6.5.3. Zusammenfassung

Wenn eine Polykapillarlinse zur röntgenografischen Texturmessung benutzt wird, kann die Defokusierungskorrektur auf Grund des quasi-parallelen Strahlengangs entfallen.
Es müssen Korrekturen für Absorption und geometrische Effekte, d.h. die Veränderung der bestrahlten Probenoberfläche sowie die Überstrahlung der Probe (und, für große Proben, die Überstrahlung des Detektors) durchgeführt werden.

Für die Korrektur der geometrischen Effekte wurden zwei Methoden vorgeschlagen, wobei eine der beiden auf Standardmessungen an untexturierten Proben zur Bestimmung einer Korrekturfunktion basiert, während die andere Methode eine geometrischen Berechnung der Korrekturfunktion benutzt. In diesem Fall wird jedoch noch eine Standardmessung zur Kalibrierung benötigt.

Die Anwendbarkeit der vorgeschlagenen Korrekturverfahren wurde an Hand von experimentellen Beispielen demonstriert.

References

Baron, H.U. & Hauk, V. (1988), *Z. Metallkde.*, **79**, 127-131.

Brakman, C.M. (1983), *J. Appl. Cryst.*, **16**, 325-340.

Brakman, C. M. (1987), *Phil. Mag. A*, **55** [1], 39-58.

Brakman, C. M. (1988), *Phil. Mag. A* **58** [4], 635-650.

Bunge, H.-J. (1982a), *Texture analysis in materials science*, Butterworths (London).

Bunge, H. J. (1982b), *Experimental techniques*, in '*Quantitative texture analysis'*, edited by Bunge, H. J., Esling, C., p. 85. Oberursel: Deutsche Gesellschaft für Metallkunde.

Bunge, H. J. (1999), *Texture and structure of polycrystals*, in '*Defect and Microstructure Analysis by Diffraction*', edited by Snyder R. L., Fiala J., Bunge H. J., pp.405., Oxford University Press (New York).

Burbach, J. (1974) in '*Mechanische Anisotropie*', edited by Stüwe, H. P., Springer (Wien).

Chernock, W. P. & Beck, P. A. (1952), *J. Appl. Phys.* **23**, 341-345

Diz, J. & Humbert, M. (1992), *J. Appl. Cryst.*, **25**, 756-760.

Dölle, H. & Hauk, V. (1978), *Z. Metallkde.* **69**, 410-417.

Dölle, H. & Hauk, V. (1979), *Z. Metallkde.* **70**, 682-685.

Downing, R. G., Gibson, W. M. & MacDonald, C. A. (1996), *Proceedings of the SPIE – The International Society for Optical Engineering* **2859**, 150-161.

Eshelby, J. D. (1957), *Proc. Roy. Soc.* **A 241**, 376-396.

Evenschor, P. D. & Hauk, V. (1975), *Z. Metallkde.* 66, 167-168.

Gale, B. & Griffiths, D. (1960), *Brit. J. Appl. Phys.* **11**, 96-102.

Genzel, Ch. (1994), *Phys. stat. sol. (a)*, **146**, 629-637.

Genzel, Ch. (1997), *Phys. stat. sol. (a)*, **159**, 283-296.

Genzel, Ch. (1998), *Phys. stat. sol. (a)*, **165**, 347-360.

Giacovazzo, C., Monaco, H. L., Voterbo, D., Scordari, F., Gilli, G., Zanotti, G. & Catti, M. (1998), *Fundamentals of Crystallography*, Oxford Science (Oxford)

Glocker, R. (1938), *ZS. f. techn. Phys.* **10**, 289-293.

Hartmann, U. R.(1973), PhD thesis, Universität Karlsruhe (TH).

Hauk, V., Nikolin, H.-J. & Weisshaupt, H. (1985), *Z. Metallkde.* 76, 226-231.

Hauk, V. (ed.) (1997), *Structural and residual stress analysis by nondestructive methods*, Elsevier (Amsterdam).

Hendrix, B. C. & Yu, L. G. (1998), *Acta Mater.*, **46** [1], 127-135.

Hermida, J. D. (1982). *Mater. Sci. Eng.* **56**, 135-141.

Hill, R. (1952), *Proc. Phys. Soc. London*, **65**, 349-354.

Holland, J. R. (1964), *Advanc. X-ray Anal.* **7**, 86-93

Holt, R. A. & Winegar, J. E. (1977), *J. App. Phys.* **48**, 3557-3559

International Tables For X-ray Crystallography Vol. IV (1974), edited by J.A. Ibers and W.C. Hamilton (Kynoch, Birmingham).

Kamminga, J.-D., De Keijser, Th. H., Delhez, R. & Mittemeijer, E. J., (1999), *J. Appl. Cryst.*, **33**, 1059-1066.

Kardiawarman, York, B. R., Qian, X. W., Xiao, Q. F., MacDonald, C. A. & Gibson, W. M. (1995), *Proceedings of the SPIE - The International Society for Optical Engineering* **2519**, 197-206.

Kneer, G. (1965), *Phys. Stat. Sol.*, **9**, 825-838.

Kogan, V. A. & Bethke, J. (1998), *Mat. Sci. Forum* **278-281**, 227-235.

Krigbaum, W. R. & Roe, R.-J. (1964), *J. Chem. Phys.*, **41** [3], 737-748.

Kröner, E. (1958), *Z. Physik* **151**, 504-518.

Kröner, E. (1971), *Statistical Continuum Mechanics*, Springer (New York).

Kumachov, M. A. & Komarov, F. A. (1990), *Physics Reports* **5**, 289-298.

Kurtasov, S. F., Borodkina, M. M.& Shestakov, K. A. (1983), *Zavodskaya Laboratoriya* **49** [9], 52-53.

Lahn, L. & Hougardy, H. P. (1999), *Mat.-wiss. u. Werkstofftech.* **30**, 77-86.

Larson, A. C. & von Dreele, R. B. (1994), *GSAS-General Structure Analysis System - Manual*, Los Alamos.

Ledbetter, H.M. & Naimon E.R. (1974), *J. Appl. Phys.*, **45** [1], 66-69.

Leigh S.-H. & Berndt, C. C. (1999), *Acta Mater.*, **47** [5], 1575-1586.

Leoni, M., (1998), PhD Thesis. Universitá di Roma "Tor Vergata", Italy.

Leoni, M., Dong, Y.H. & Scardi, P. (1999), *Mat. Sci. Forum*, **321-324**, 439-444.

Leoni, M., Welzel, U. & Scardi, P. (2001), *Proceedings of the conference "Accuracy in Powder Diffraction III"*, April 22-25, 2001, National Institute of Standards and Technology, Gaithersburg, MD, USA.

Leroux, J. & Thinh, T. P. (1977), *Revised Tables of X-Ray Mass Attenuation Coefficients*, Corporation Scientifique Claisse Inc. (Quebec).

Love, A. E. H. (1927), *A treatise on the mathematical theory of elasticity*, Cambridge (New York).

Machlin, E.S. (1995), *Materials science in microelectronics. Vol. 2*, Giro Press (New York).

Matthies, S. & Humbert, M. (1995), *J. Appl. Cryst.*, **28**, 254-266.

Matthies, S., Vinel, G. & Helming K. (1987), *Standard distributions in texture analysis,* Akademie Verlag (Berlin).

Matthies, S., Wenk, H.-R. & Vinel, G. W. (1988), *J. Appl. Cryst.*, **21**, 285-304.

Meyers, M. A. & Chawla, K. K. (1984), *Mechanical Metallurgy, Principles and applications;* Prentice-Hall (Englewood Cliffs), pp. 57-58.

Möller, H. & Barbers, J. (1935), *Mitt. K.-Wilh.-Inst. Eisenforsch., Düsseldorf*, **17**, 157-166.

Möller, H. & Martin, G. (1939), *Mitt. K.-Wilh.-Inst. Eisenforsch., Düsseldorf*, **21**, 261-269.

Murakami, M. & Yogi, T. (1985), *J. Appl. Phys.*, **57** [2], 211-215.

Neerfeld, H. (1942), *Mitt. K.-Wilh.-Inst. Eisenforschg.*, **24**, 61-70.

Nikolin, H.J. (1983), Diploma thesis, Institut für Werkstoffkunde, RWTH Aachen.

Noyan, I.C. & Cohen, J. B. (1987), *Residual stress. Measurement by diffraction and interpretation*, Springer Verlag (New York).

Nye, J.F. (1957), *Physical properties of crystals*, Oxford University Press (Oxford).

Ortiz, M. & Hermida, J. D. (1981). *Texture* **4**, 159-169.

Rafaja, D., Valvoda, V., Kuzel, R., Perry, A. J. & Treglio, J.R. (1996), *Surface & Coatings Technology*, **87**, 302-308.

Reuss, A. (1929), *Zeitschrift für angewandte Mathematik und Mechanik*, **9**, 49-58.

Roe, R.-J. & Krigbaum, W. R. (1964), *J. Chem. Phys.* **40** [9], 2608-2615.

Roe, R.-J. (1965), *J. Appl. Phys.*, **36** [6], 2024-2031.

Sasaki, T., Yoshioka, Y. & Kuramoto, M. (1993), in *Current Japanese Materials Research*, Vol. 10, eds. K. Tanaka, S. Kodama, T. Goto, Elsevier (Amsterdam), 73-94.

Scardi, P., Leoni, M. & Dong, Y.H. (1999), *Adv. X-ray Anal.*, **42**.

Scardi, P., Setti, S. & Leoni, M. (2000). *Mat. Sci. Forum* **321-324**, 162-167.

Schulz, L. G. (1949). *J. Appl. Phys.* **20**, 1030-1033.

Serruys, W., Van Houtte, P. & Aernoudt, E. (1987), in *Residual Stresses in Science and Technology* (Macherauch, E. & Hauk, V., ed.). Deutsche Gesellschaft für Metallkunde (Oberursel)

Serruys, W., Langouche, F., van Houtte, P. & Aernoudt, E., Proc. (1989), in Proc. of ICRS2 (Beck, G., Denis, S. & Simon, A., ed.). Elsevier Applied Science (London, New York).

Sonneveld, E. J., Delhez, R., de Keijser, Th. H. & Mittemeijer, E. J. (1991). *Mat. Sci. Forum* **79-82**, 85-90.

Stickforth, J. (1966), *Tech. Mitt. Krupp – Forsch.-Ber.* **24** [3] 89-102.

Tenckhoff, E. (1970). *J. Appl. Phys.* **41** (10), 3944-3948.

vande Walle (ed.) (1981), *Residual stress for designers and metallurgists*, Materials/Metalworking series, American Society for Metals (Metals Park, Ohio)

van Leeuwen, M., Kamminga, J.-D. & Mittemeijer, E. J. (1999), *J. Appl. Phys.* **86** [4], 1904-1914.

Voigt, W. (1910), *Lehrbuch der Kristallphysik*, Teubner (Leipzig-Berlin).

Vook, R.W. & Witt, F. (1965), *J. Appl. Phys.* **36** [7], 2169-2171.

Welzel, U., Lamparter, P., Ligot, J., Vermeulen, A. & Mittemeijer, E. J. (2002), in preparation

Wieder, T. (1995a), *Thin Solid Films*, **256,** 39-43.

Wieder, T. (1995b), *J. Appl. Phys.*, **78 [2],** 838-841.

Wieder, T. (1995c), *Computer Physics Communications*, **85** [3], 398-414.

Wieder, T. (1996), *Computer Physics Communications*, **96** [1], 53-60.

Witt F. & Vook, R. W. (1968), *J. Appl. Phys.*, **39** [6], 2773-2776.

Curriculum Vitae

Name	Udo Siegfried Welzel
Date of birth	February 19, 1972
Place of birth	Selb (Bayern)
School	1978-1982 Grundschule Erkersreuth – Selb-Plößberg 1982-1991 Gymnasium Selb
Community Service	1991-1992 Home of the Aged ‚Paul-Gerhardt-Haus' in Selb
Higher Education	1992-1998 Physics at University of Bayreuth, Bayreuth since 1998 PhD student at Max Planck Institute for Metals Research and Institut für Metallkunde of Stuttgart University, Stuttgart

Danksagung